Modeling, fabrication and experimental characterization of weakly coupled MEMS arrays for mass detection

Toky Harrison Rabenimanana

UBFC
UNIVERSITÉ
BOURGOGNE FRANCHE-COMTÉ

UNIVERSITÉ DE FRANCHE-COMTÉ

Thèse de doctorat de l'établissement Université Bourgogne Franche-Comté

Préparée à l'Université de Franche-comté

Ecole doctorale n°37

Ecole Doctorale Sciences Pour l'Ingénieur et Microtechniques

Doctorat de Sciences pour l'Ingénieur

Par

Toky Harrison RABENIMANANA

Modélisation, fabrication et caractérisation expérimentale de réseaux MEMS faiblement couplés pour la détection de masse

Modeling, fabrication and experimental characterization of weakly coupled MEMS arrays for mass detection

Thèse présentée et soutenue à Besançon, le 16 décembre 2020

Composition du Jury :

Skandar BASROUR	Professeur des Universités, TIMA, Grenoble	Président
Sébastien HENTZ	Directeur de recherche, LETI, Grenoble	Rapporteur
Claude-Henri LAMARQUE	Professeur, ENTPE, LTDS, Lyon	Rapporteur
Jérôme JUILLARD	Professeur, CentraleSupélec, GEEPS, Gif sur Yvette	Examinateur
Joseph LARDIES	Professeur des Universités, FEMTO-ST, Besançon	Directeur de thèse
Najib KACEM	Maître de Conférences, FEMTO-ST, Besançon	Codirecteur de thèse
Vincent WALTER	Maître de Conférences, FEMTO-ST, Besançon	Codirecteur de thèse

Remerciements

Mes travaux de thèse ont été effectués au département mécanique appliquée de l'Institut Femto-st (Université de Franche-Comté). J'ai rejoint l'équipe MEMS durant les trois années passées au sein de ce laboratoire, et je tiens à remercier les personnes avec qui j'ai travaillé.

Tout d'abord, je remercie mon directeur de thèse, Joseph Lardiès, pour ses conseils concernant l'orientation de mes travaux de thèse. Merci à mon codirecteur de thèse, Vincent Walter, pour son engagement dans l'encadrement de ma thèse, son aide sur le travail expérimental, et pour m'avoir permis de participer à des congrès à l'étranger. Merci à mon autre codirecteur de thèse, Najib Kacem, pour avoir partagé ses connaissances sur la dynamique non-linéaire. Merci également aux autres membres de l'équipe MEMS avec qui j'ai travaillé, particulièrement Patrice Le Moal pour sa participation à ce travail et ses précieux conseils tant en matière de modélisation que d'expérimentation, et Gilles Bourbon pour sa contribution à la conception et à la fabrication des micro-capteurs que j'ai testés, et pour son aide sur les expériences réalisées dans ce travail. Je remercie aussi toutes ces personnes pour la relecture de mon manuscrit de thèse et leurs suggestions enrichissantes.

Je remercie tous les membres de mon jury d'avoir pris le temps de lire mon travail et d'assister à la soutenance de ma thèse. Merci à Skandar Basrour d'avoir accepté de présider le jury, merci à Sébastien Hentz et à Claude-Henri Lamarque d'avoir accepté la fonction de rapporteur de cette thèse, et je remercie aussi Jérôme Juillard d'avoir accepté de se joindre au jury en tant qu'examinateur.

Je remercie également toutes les personnes qui ont participé directement ou indirectement à ce travail, notamment Benoît Verdin qui m'a aidé sur l'utilisation du picoscope, et Roland Salut qui a réalisé le dépôt de masse sur les capteurs à l'aide de la sonde ionique focalisée.

Je tiens aussi à remercier l'ensemble des membres du département mécanique appliquée, mes amis au département MN2S, Claude, Fernando, Jean-Loup, Aymen, Jean et Emmanuel, avec lesquels j'ai passé des bons moments, et mes collègues de bureau, Faleh et Fangnao.

Et enfin, j'adresse mes remerciements à ma famille. Merci à mes parents pour m'avoir soutenu, et à Jean-Rémi et Cyrano qui m'ont permis de poursuivre mes études à Clermont-Ferrand.

Contents

General introduction

Context

Since the development of microfabrication technologies, miniature systems become more and more present in our daily life. It starts with the invention of integrated circuits involving large numbers of extremely small transistors on a small chip. This is then followed by the development of Micro Electro-Mechanical Systems (MEMS), which are devices covering a large domain of applications. These devices are widely used in everyday products, especially in wearable devices and automotive. The small size of MEMS allows them to be manufactured in parallel with low production costs.

MEMS applications include different kinds of sensors which measure physical quantities like acceleration, pressure, temperature and mass. Mass sensing consists in detecting or measuring a small amount of analyte with a micro sensor. Also known as microbalances, MEMS mass sensors have not only a low energy consumption, but also a very high sensitivity, making them suitable for biological, chemical and gas detection.

Depending on their operating principle, mass sensors can detect the analyte in different ways. Among them, there is mass sensing based on the frequency shift. This principle exploits the fact that the addition of a mass perturbation on a single resonator leads to a decrease in its resonance frequency. Given that this mass sensing method has proven its effectiveness, it is used by almost all current mass sensors. However, the interest of having even more sensitive devices has prompted us to investigate other detection principles. One of them is the mode localization that is the subject of several recent studies. Initially studied by Anderson [1] in the field of matter physics, the mode localization has then been proposed for mass sensing application. Instead of measuring a frequency shift, mode localized sensors use the change in the vibration mode of weakly coupled identical resonators when a small perturbation is introduced. The main interest of mode localization is the fact that sensors using this principle have a higher normalized sensitivity compared to those using a frequency shift [2]. Thus, researches on mode localized sensors have been conducted over the last fifteen years [3]. These studies do not only concern mass detection, but have been extended to other types of sensors.

Problem statement and motivation

Since mode localized sensors have been studied, their use has remained at the experimental level, but their performance has continued to increase. However, the following problems have often been identified:

- The manufacturing constraints:
  The coupled resonators of mode localized sensors must be perfectly identical, which is limited by the manufacturing process. The current microfabrication technology is certainly very advanced but the micromachining relative tolerance remains poor at the micrometer scale. Due to the fact that the resonators of the fabricated device are not exactly identical, the system exhibits localized vibration reflecting the presence of perturbation while no mass has been added. As this initial imbalance limits the sensor operation, it is then necessary to find a way to counterbalance its effects.

- The design constraints:
  Mode localized sensors are composed of resonators which are connected to each other by a coupling. Most of sensors considered by authors include a mechanical coupling, but the geometry of this part of the device is not modeled and therefore does not allow to be predictive on the value of the coupling obtained. As the sensitivity of the sensor depends directly on the coupling intensity, an accurate model needs to be developed in order to design it properly.

- The sensitivity limitation:
  The sensitivity of mode localized sensors is defined by the coupling intensity. Indeed, the sensitivity is inversely proportional to the ratio between the effective stiffness of the coupling element and that of the resonators. Reducing this coupling ratio will then increase the device sensitivity. However, the more the coupling decreases, the closer the frequencies of each vibration mode of the system are to each other. As the measurement of the sensor output metrics is made on these vibration modes, we must be able to distinguish them. Consequently, the maximum sensitivity is fixed by the minimum coupling ratio that ensures the separation between the resonance peak of each mode, preventing the well-known mode aliasing phenomenon. In order to further improve the device performance, it would then be interesting to increase its sensitivity without changing the coupling ratio.

- The resolution limitation:
  To identify the mass perturbation, mode localized sensors measure the change in the vibration mode of a system having coupled resonators. But other output metrics can also be used for this. However, all of them are based on vibration amplitude measurement. Thus, the minimum detectable mass depends directly on the minimal detectable amplitude variation. In order to improve the mass resolution of the sensor, it is then necessary to have a device with a high dynamic range.

Manuscript organization

As solutions to the problems mentioned above, we propose some concepts that will be demonstrated through two proposed MEMS devices respectively involving attractive and repulsive resultant electrostatic forces. For that, the manuscript is divided into four chapters:

- In Chapter 1, we provide a literature review on MEMS and their fabrication while focusing on mass sensors and mode localization. We also review in detail the difficulties encountered on existing mode localized sensors.

- In Chapter 2, we present a device with an attractive electrostatic force, allowing to answer the problem of manufacturing defects generating asymmetry of the coupled resonators used in mode localized sensors. The model uses two Euler-Bernoulli beams coupled by a torsion spring. The dynamic behavior of the system is determined by discretizing the equations of motion by the Galerkin method, and the resolution of these equations is performed by the method of multiple scales.

- Chapter 3 is dedicated to the experimental validation of the theoretical model established in the previous chapter. Afterwards, we present a solution allowing to overcome the sensitivity limitation of mode localized sensors.

- Chapter 4 investigates a device using repulsive electrostatic forces from both theoretical and experimental points of view. It will be shown in this chapter that this device makes it possible both to increase the dynamic range of this type of sensor and to work with higher amplitude levels, thus increasing the resolution.

Chapter 1

State of the art

Contents

1.1 Introduction

In this chapter, we present a brief review on MEMS and microfabrication technologies. Then, we talk about mass microsensors and their working principles, in particular the mode localization which is the main subject of this thesis. Following the literature review, we highlight the advantages of mode localization and identify the problems of existing mode localized mass sensors.

1.2 MEMS

1.2.1 Generality

MEMS or Micro Electro-Mechanical Systems are micro-scale devices integrating mechanical and electrical elements performing a specific function. The history of the development of MEMS begins around 1970s when the microfabrication technologies rapidly matured. Since 1990, MEMS have entered a period of growth and their applications now cover a very wide field [4]. The main advantage of MEMS is its lowcost production. The batch processing allows many components to be manufactured in parallel, and in a reduced surface area. MEMS also have a low power consumption with improved sensitivity and accuracy. In addition, their small size allows them to be integrated into other systems. The global MEMS market has been growing steadily for several years and is expected to grow in the coming years.

1.2.2 Categories and applications

Depending on their applications, MEMS can be separated into four categories, which are Sensors and actuators, MOEMS, RF-MEMS and BioMEMS, as illustrated in Figure 1.1.

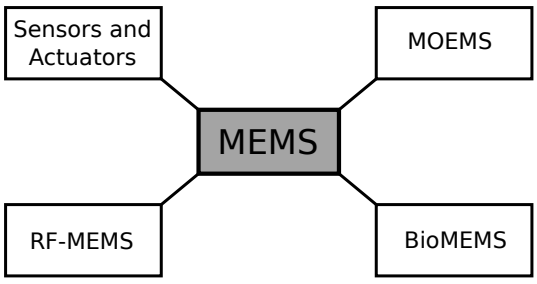

Figure 1.1: Categories of MEMS

Sensors and actuators belong to the category of transducers. They serve the function of transforming a signal in one form of energy to another. Sensors are devices capable of measuring a physical quantity and transforming it, usually into electrical signals. The physical quantity to be measured can be mechanical (force, pressure, speed, acceleration), thermal (temperature, heat flux), chemical (pH, chemical concentration) or magnetic (magnetic field, magnetic force). For example, we can see in Figure 1.2a a gyroscope using a polysilicon vibrating ring [5]. Unlike sensors, actuators are devices that convert an energy (electrical, thermal, pneumatic) to a mechanical output. The output is gen-

erally a force, a moment or a displacement, and they are generated by an electrostatic, magnetic or piezoelectric actuation.

MOEMS or Micro-Opto-Electro-Mechanical systems are a class of MEMS devices that sense or manipulate optical signals on a very small size scale. They include devices like optical switches, DMD (Digital Micromirror Devices) and microbolometers. Actually, MOEMS are almost ubiquitous in many devices like video projectors. Figure 1.2b shows an example of these devices, it is a MOEMS with a two directional electrostatic comb-drive X–Y micro-stage [6].

RF-MEMS or Radio-Frequency Micro Electro-Mechanical Systems are MEMS with electronic components that are used to provide radio-frequency functionality. Their application concerns wireless communication systems for transmitting or receiving signals. We can see in Figure 1.2c an example of such a device, it is a MEMS switch used for telecommunication applications [7].

BioMEMS or Biomedical Micro Electro-Mechanical Systems concern microfabrication technologies made for biomedical applications. These devices allow to interact with cells, proteins or tissue. In Figure 1.2d, we can see an example of BioMEMS, which is a microneedle used for microfluidic transdermal interfacing [8]. BioMEMS are also associated with LOC or Lab On a Chip.

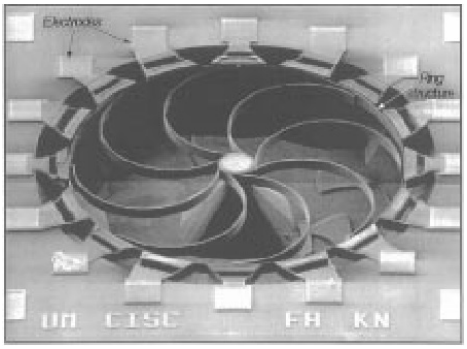

(a) Gyroscope [5]

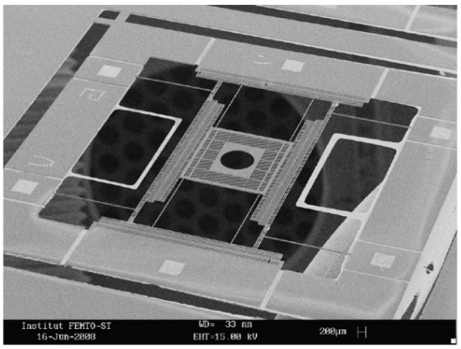

(b) MOEMS with a micro-stage [6]

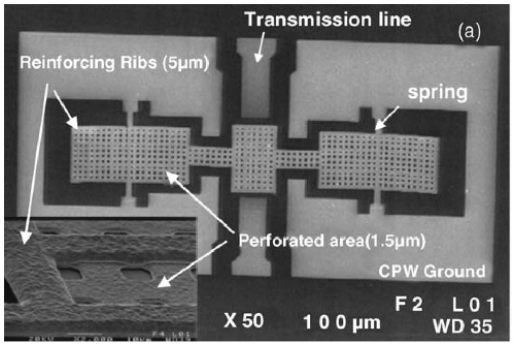

(c) RF-MEMS switch [7]

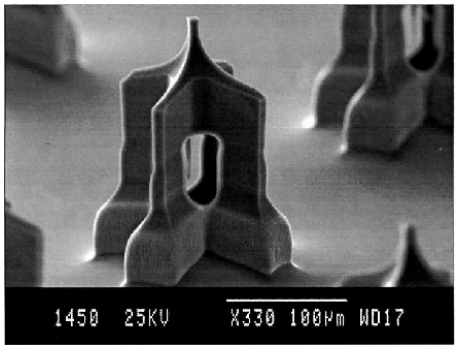

(d) Microneedles [8]

Figure 1.2: Examples of MEMS

1.2.3 Fabrication

MEMS fabrication processes

MEMS fabrication uses the technology of microfabrication that was first used for integrated circuits. They are generally made on single crystal silicon wafers. The manufacturing of MEMS takes place in a clean room where the wafer goes through many steps of fabrication process. According to [9], these steps can be separated into three categories: the lithography, the pattern transfer with subtractive techniques and the pattern transfer with additive techniques.

The lithography is a technique that is used to transfer copies of a master pattern onto the surface of a solid material such as a silicon wafer. The most widely used lithography is photolithography. It consists in first using a surrogate layer (photoresist) that is patterned with UV. The pattern of this layer is then transferred to the material of interest. But there are also other form of lithographies, such as ultraviolet lithography, x-ray lithography, and charged particle beam lithography.

The pattern transfer with subtractive techniques includes dry etching, wet chemical etching, wet bulk micromachining, thermal energy-based removing, and mechanical energy-based removing.

- Dry etching: it is a process in which the solid substrate is etched by gaseous species.
- Wet chemical etching: in this process, material are chemically removed through etching process of preferentially exposed surfaces.
- Wet bulk micromachining: it is also a chemical etching used to sculpt isotropic and anisotropic 3D microfeatures in single crystal semiconductor substrates.
- Thermal energy-based removing: it consists in using thermal energy provided by a heat source to melt or vaporize the volume of the material to be removed.
- Mechanical energy-based removing: in this process, the physical removal of unwanted material is achieved by mechanical energy at the work piece.

The pattern transfer with additive techniques concerns processes where materials are added to the device under construction. It includes physical and chemical vapor deposition, chemical, photochemical and electrochemical-based forming, thermal energy-based forming, and micromolding techniques.

- Physical and chemical vapor deposition: the physical vapor deposition consists of a direct material deposition by using evaporation, sputtering or laser beam, while the chemical vapor deposition uses chemical reaction that take place on the surface of the substrate.
- Chemical-based forming: it is a process where chemical reactions create features by forming new compounds.
- Photochemical-based forming: in this process, photoenergy solidifies a material into a three-dimensional shape.

- Electrochemical-based forming: it concerns electroless and electrodeposition. In this process, the energy at the work piece is electrochemical.
- Thermal energy-based forming: it is a method where thermal energy provided by a heat source transforms a material's structure or shape.
- Micromolding techniques: it is a replication-based process involving feature-transferring mechanisms like compression or injection.

The MUMPS®

To fabricate MEMS devices, there are several foundries which are companies offering manufacturing services with surface micromachining or bulk micromachining [10]. Among them is the MEMSCAP that proposes the MUMPS® [11]. The MUMPS® or Multi-User MEMS Processes is a commercial program of surface micromachining fabrication intended for the industrial and academic communities.

The MUMPS® allows users to fabricate MEMS devices based on seven layers of materials shown in Figure 1.3. It is composed of one layer of nitride, one layer of metal, two layers of oxide (1st Oxide and 2nd Oxide) and three layers of polysilicon (Poly0, Poly1 and Poly2). The silicon nitride is used as electrical isolation between the polysilicon and the substrate, the polysilicon layers are used as structural layer, and the oxide layers are used as sacrificial layer. Their thicknesses are given in Table 1.1. Depending on the desired structure, these layers are deposited and etched during the fabrication process.

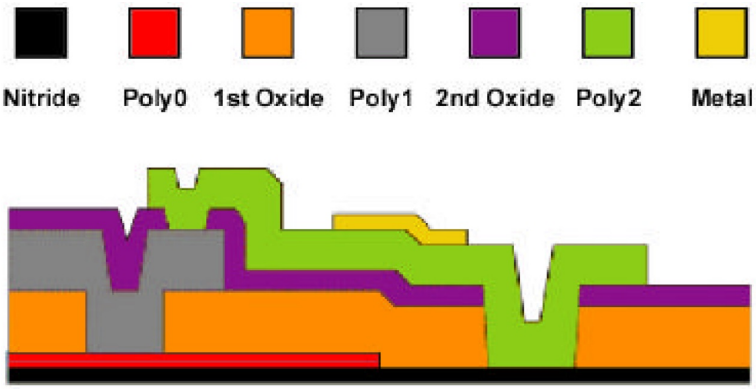

Figure 1.3: Cross sectional showing the layers of the MUMPS® process [11]

Table 1.1: Thicknesses of each layer

Layer	Nitride	Poly0	1st Oxide	Poly1	2nd Oxide	Poly2	Metal
Thickness (μm)	0.6	0.5	2.0	2.0	0.75	1.5	0.5

The process of the MUMPS® starts with a 100 mm silicon wafer, which is doped with phosphorus. Next, the silicon nitride layer is deposited with LPCD (Low Pressure Chemical Vapor Deposition). It is followed by successive depositions of layers of polysilicon and oxide, which is also known as PSG

(PhosphoSilicate Glass). All layers of polysilicon are deposited with LPCVD. These layers are then patterned by photolithography. After patterning the photoresist, the layers of polysilicon are etched with a RIE system (Reactive Ion Etch). For the PSG, they are also deposited between each layers of polysilicon with LPCVD, and lithographically patterned. For the patterning of the 1st oxide, it is possible to create dimples by removing a part of its thickness during the etching. If the entire thickness is removed, we get an anchor that will be filled by the Poly1. After each deposition of the Poly1 and the Poly2, a thin film of PSG is deposited above them and the wafer is annealed at $1050° C$ for 1 hour. It dopes the polysilicon with phosphorus from the PSG layers above and below it. Once the Poly2 is patterned, the last layer of metal is deposited and patterned using lift-off. Finally, all sacrificial layers are released by immersing the wafer in a bath of 49 % HF. All of these steps are illustrated in Appendix A.1.

1.2.4 Characterization

Once the MEMS microfabrication is finished, the next step is the characterization. This step consists in evaluating the results of the fabrication by measuring the etching, the thickness, the in-plane dimension, the depth or the surface roughness. It is also used to detect all defaults after the fabrication. To do this, we can use instruments like an optical microscope, an optical profilometer, a stylus profilometer or a SEM (Scanning Electron Microscope).

The optical microscope allows visual inspection of the fabricated device and verifying the in-plane dimension. But as it uses visible light to generate images, its resolution is limited by the wavelength of the illumination source. The microscope can not reproduce any object smaller than $0.2\,\mu m$, so it is not suitable for the characterization of nanoscale devices.

The optical profilometer is an instrument that is used to measure height variations. It allows to extract topographical data from a surface. Thus, we can determine the depth of a hole or the thickness of a layer. The technique consists in using wave properties of light (interference) to compare the optical path difference between a test surface and a reference surface.

The stylus profilometer is also an instrument used to measure heights on a surface. But instead of using light, it uses a physical moving probe that is directly in contact with the sample in order to acquire the surface height. This tool have a good resolution that can be below $1\,nm$. But as this technique requires physically touching the sample, it can damage some surfaces.

The SEM is a microscope that uses a focused electron beam for observing sample. The electrons that interact with atoms in the sample produce signals that contain information about the observed surface. As we don't use the light anymore for observation, the resolution may reach 1 nm, which is well above the resolution of an optical microscope. It can be used to measure both in-plane dimensions and thicknesses.

1.2.5 Precision in microfabrication

As seen previously, characterization is carried out once the fabrication is finished in order to control the size of the fabricated device. However, the microfabrication technology has limited accuracy so defects can occur even if all the processes of the fabrication have been executed correctly. Microfabrication have an excellent absolute tolerance because it allows us to fabricate microscale devices. But as this absolute tolerance is fixed, the relative tolerance becomes less and less excellent as the size of the device decreases. The Figure 1.4 reproduced from [9] shows the relative machining tolerance as a function of linear dimension.

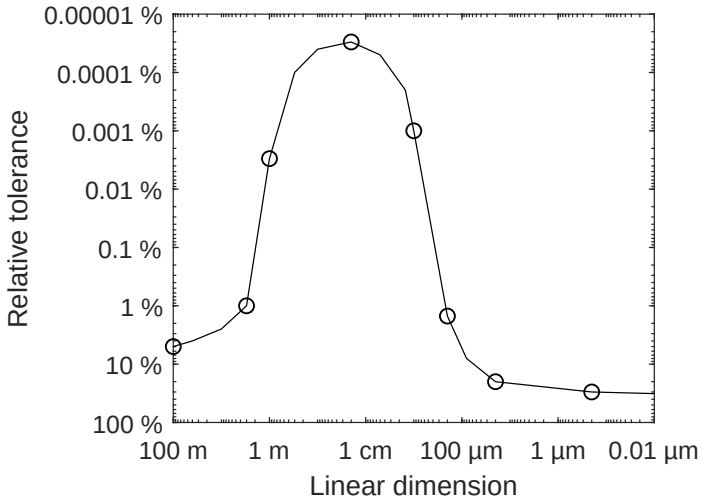

Figure 1.4: Machining tolerance as a function of linear dimension [9]

For dimensions between $1\,cm$ and $100\,\mu m$, we still have an acceptable accuracy. But for dimensions less than $100\,\mu m$, the relative tolerance increases and it can be over $10\,\%$. As a consequence, we cannot fabricate with a very high precision devices with dimensions under this value, and it mainly concerns nanoscale devices like NEMS (Nano Electro-Mechanical Systems).

1.3 Mass sensors

1.3.1 Generality

MEMS mass sensors are devices which are used to detect and measure a mass. Depending on the application, the analyte can be a bacteria, virus, toxin, protein or other molecule. Mass detection can be done in air or in a liquid, for example to detect the presence of a compound or to measure its concentration in the medium. To do this, the surface of the MEMS device is coated with a functionalized layer containing receptors chosen for their chemical affinity with the analyte. But MEMS sensors can also be used in vacuum for other applications like mass spectrometry.

1.3.2 Resonators used for mass sensing

Microbeams

Almost all mass sensors include resonant mechanical systems, such as microbeams. In general, these resonators are composed of beams vibrating in flexural or torsional mode [12]. The microbeams as a resonator are usually used either in cantilever or clamped-clamped configuration, as shown in Figure 1.5. Micro and nanocantilevers have been used by many authors in many studies in order to detect various kinds of mass like explosive [13], pesticides [14], viruses [15], alkanes, alcohols and water vapor [16]. Other authors used mass sensor with doubly clamped beams [17, 18].

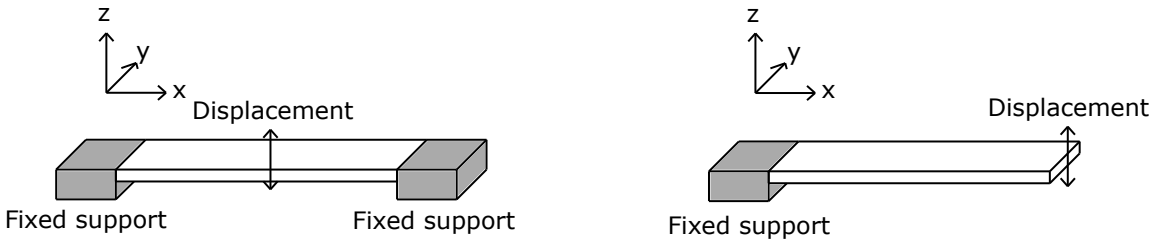

(a) Doubly clamped beam

(b) Cantilever

Figure 1.5: Illustration of the two types of microbeam

Other resonators used

There are also other resonators that can be used for mass sensing. One may distinguish three other types: Bulk Acoustic Wave resonators or BAW, Surface Acoustic Wave resonators or SAW and tuning forks.

The BAW are resonators composed of two electrodes on either side of piezoelectric material substrate. Among BAW resonators, we have Quartz Crystal Microbalances or QCM, which used quartz for the substrate. It is the most used and commercially available mass sensor. Its main advantage is its high quality factor allowing the use of the device in air. Zu et al. [19] presented a high temperature BAW mass sensor used for thermogravimetric analysis.

The SAW are devices that use transducer on the surface of a substrate to generate acoustic waves propagating along the surface. These waves have two components normal and parallel to the propagation direction. This kind of sensor has been considered by Hao et al. [20] in order to investigate its mass sensitivity.

Tuning forks are fork-shaped resonators that are commonly used as gyroscope, but they can also be found in mass sensing application. Kunicki et al. [21] used a quartz tuning fork mass change sensor to determine the density of focused ion beam induced deposition.

1.3.3 Actuation for mass sensors

Electrostatic actuation

As resonators are used in mass sensors, we need to generate vibrations with an actuation. Electrostatic actuation consists in using the force between conducting electrodes when a voltage is applied. The actuation voltage is applied on the driver electrode and it is often composed of a DC voltage combined with an AC voltage. Depending on the electrodes configuration, the resulting force can be attractive or repulsive.

Electrostatic actuation using attractive force is mainly used for microbeams. The attraction takes place between the microbeam (mobile or movable electrode usually to ground) and the drive electrode under it (fixed electrode usually to the applied voltage). As illustrated in Figure 1.6, the electrode and the microbeam can be assimilated to a parallel plate capacitor with variable capacitance, and the resulting force F_E is given by

$$F_E = \frac{1}{2}\frac{\varepsilon A V^2}{g^2} \tag{1.1}$$

where ε is the dielectric constant of the medium between the two plates of the capacitor, A is the area of the plates, V is the applied voltage and g is the distance between the plates or gap.

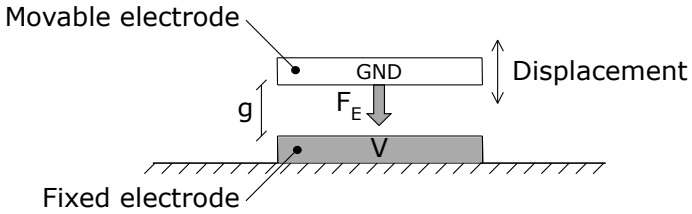

Figure 1.6: Electrostatic actuation using attractive force

When the distance g is not negligible with respect to the dimensions of the plates, the intensity of the electrostatic force is higher due to the effects of fringing field. To take them into account, this expression is multiplied by a coefficient [22].

When the applied voltage is too high, the mechanical restoring force of the structure becomes insufficient and the structure can stick to the fixed electrode, which can leads to the failure of the device. To avoid this, the applied DC voltage must be below a limit value called pull-in voltage. Analytical models allowing to evaluate this pull-in voltage exist in the literature. It concerns several electrostatically actuated resonators like square and circular plates [23], doubly clamped microbeams [24], and cantilevers [25]. For cantilevers, the maximum static deflection with this pull-in voltage is around 45 % of the initial gap.

For forced vibrations where the actuation is composed of a combined AC-DC voltage, the attractive electrostatic force does not only depend on the applied voltage, we have in addition to the harmonic load, other forces that depend on the displacement of the structure. These forces create softening effect that decreases the stiffness of the structure, and also its resonance frequency. This softening effect increases with the applied DC voltage. These forces that depend on the displacement also create

electrostatic nonlinearities with a softening behavior. Electrostatic nonlinearities bend the frequency response of the device to the left. This creates multivalued region, where the vibration amplitude can have three different values for a given excitation frequency, as illustrated in Figure 1.7.

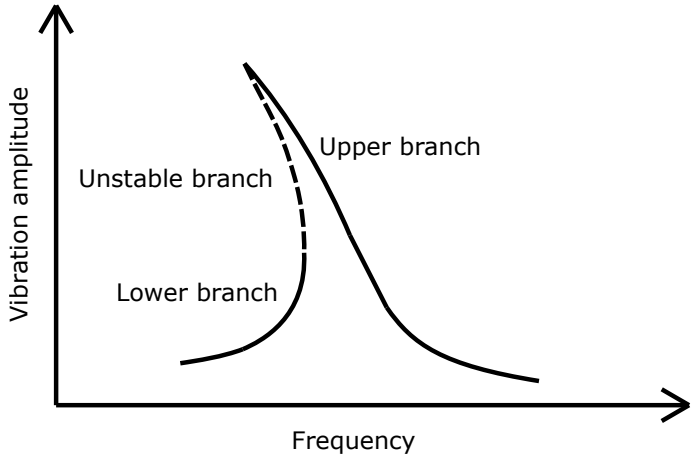

Figure 1.7: Frequecy response with softening behavior

Electrostatic nonlinearities appear when the vibration amplitude increases, and it limits the dynamic linear range of the device. But they can be canceled out by tuning some design parameters. Kacem et al. proposed in [26] a model for nonlinearity cancellation of electrostatically actuated cantilevers, which allows to drive the device beyond the critical amplitude.

Unlike electrostatic actuation using attractive force, the one with repulsive force uses the repulsion between a fixed electrode and a movable one. This actuation requires three different electrodes: a fixed electrode and a movable electrode which are grounded, and the actuation electrode on which we apply the voltage. The repulsive force can be explained by the imbalance in the distribution of the electrostatic field between these three electrodes. As reported in [27], we can have four configurations for this kind of actuation, which are the levitation of comb drive actuator [28], the in-plane repulsive actuator [29], the out-of-plane repulsive actuator [30] and the three layered repulsive actuator [31]. These actuations can all be used for micromachined devices and they are illustrated in Figure 1.8. Unlike electrostatic actuation with attractive force, which has the problem of the pull-in phenomenon, the movable electrode never sticks to the fixed one. But the intensity of the resulting repulsive force is less important for the same applied voltage.

Other actuation used

There are also other types of actuation used in mass sensor, such as electrothermal actuation, piezoelectric actuation, electromagnetic actuation and electrostatic actuation.

Electrothermal actuation consists in applying a voltage signal to a heating resistor. It is then converted into a thermal contraction and expansion which force the structure to vibrate. Wasisto et al. [32] proposed a MEMS cantilever with electrothermal actuation, which is used for airborne ultrafine particle sensing.

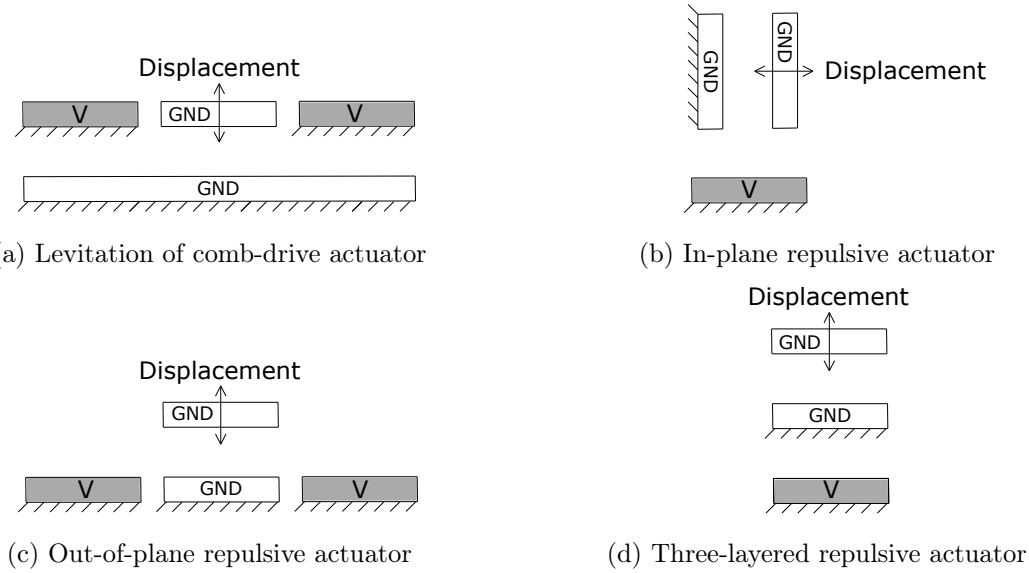

(a) Levitation of comb-drive actuator

(b) In-plane repulsive actuator

(c) Out-of-plane repulsive actuator

(d) Three-layered repulsive actuator

Figure 1.8: Electrostatic actuation using repulsive force

Piezoelectric actuation concern all devices using piezoelectric resonators like QCM, but it can also be used to actuate other resonators like microbeams by adding a thin film of piezoelectric material on the structure. To generate the vibrations, the piezoelectric material produces mechanical stress when a voltage is applied. As a mechanical stress applied to the material induces a voltage, it can also be used for vibrations sensing. Joshi et al. [33] proposed a mass sensor based on cantilevers actuated with piezoelectric ZnO thin films. The device shows high quality factor around 234 at room temperature and atmospheric pressure.

Electromagnetic actuation concern structures that vibrate in presence of variable magnetic field. It may involve the use of Lorentz force or magnetostriction with ferromagnetic materials. Ergeneman et al. [34] presented a mass sensor using magnetic actuation. Their device also uses a magnetic readout for vibration detection.

1.3.4 Vibration sensing in mass sensors

In order to measure the response of the sensor, we also need to detect its vibrations, and several methods can be used for this. These include the piezoresistive sensing, the optical sensing and the capacitive sensing.

Piezoresistive sensing uses piezoresistors on the structure to detect its vibrations. As the change in the resistance of the piezoresistor is proportional to its deformation, we can detect the vibrations by measuring this resistance. A Wheatstone bridge is used for this, so we have directly a voltage signal for the output. This method is often combined with electrothermal actuation when the device is composed of microbeams [32].

Optical sensing is a method mainly used for micro cantilever. A laser beam hits the cantilever and is reflected to be detected by an optical sensor. When the cantilever moves, the reflected beam deflects

and the displacement can be measured. This method often concerns the measurement of the static deflection due to its resolution that can reach the sub-nanometer range, but it can also measure the dynamic deflection. Another principle consists in measuring the variations of intensity of the diffracted beam to detect the vibrations [35].

The capacitive sensing only concerns electrostatic actuation. The variable capacitance due to the displacement of the moving electrode creates a variable current, and measuring it allows us to sense the vibrations. This motional current is proportional to the applied DC voltage and the surface area of the electrode. But this signal is always combined with feedthrough signal, due to the direct coupling between the drive and sense ports. The feedthrough signal is caused by a parasitic feedthrough capacitor which is in parallel to the resonator. As it causes an antiresonance around the resonance frequency of the device, a feedthrough cancellation is required [36, 37].

1.4 MEMS mass sensing methods

To measure the added mass, sensors have different working principles and we will see these different sensing methods in this section. Almost all of them are based on vibrating resonators, but there are other sensors operating in static mode.

1.4.1 Sensing using frequency shift

Principle

The mass sensing based on frequency shift is a principle used by almost all sensors with a single resonator. The resonator of such a sensor can be modeled by a mass-spring system as illustrated in Figure 1.9.

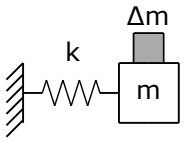

Figure 1.9: Mass-spring system

The resonance frequency of this system is given by

$$f_0 = \frac{1}{2\pi}\sqrt{\frac{k}{m}} \tag{1.2}$$

where k is the stiffness and m is the mass. When a mass perturbation Δm is added on the system, it creates a shift in its resonance frequency. To measure the added mass, the relation between the relative changes in the mass and the resonance frequency is given from [38] by

$$\frac{\Delta f_0}{f_0} = \frac{1}{2}\frac{\Delta m}{m} \tag{1.3}$$

The sensitivity of this kind of mass sensor is given by the frequency variation per unit of mass. But we should consider the minimum detectable frequency variation, which depends on the quality factor of the resonator. This also defines the mass resolution of the sensor.

For the readout, phase looked-loop circuits are used to track automatically the varying resonance frequency of the sensor. Thus, this control system allows the sensors to do a real-time sensing. The NEMS sensor proposed by Ekinci et al. [17] used a self oscillation loop system to detect a sequential gold atom adsorption upon a silicon doubly clamped beam resonator. As shown in Figure 1.10, the beam length is around $14.2\,\mu m$ and the frequency shift is detected almost at the same time as the addition of the masses.

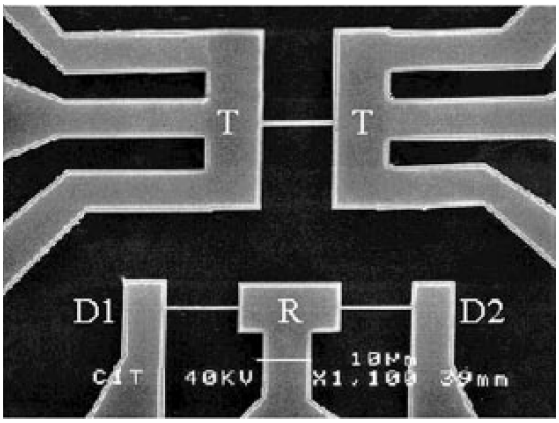

(a) SEM image of the device

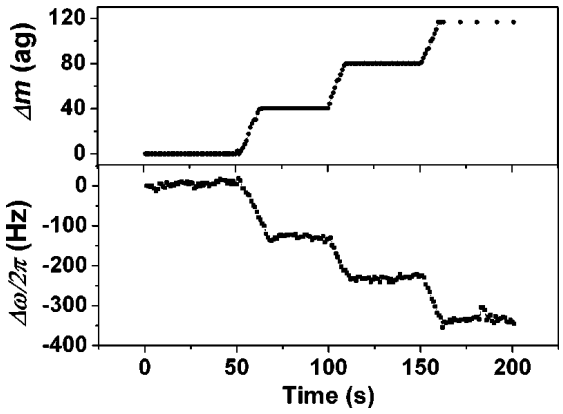

(b) Frequency shifts induced by a sequential gold atom adsorption

Figure 1.10: NEMS mass sensor based on frequency shift of doubly clamped beam [17]

Some resonators like microbeams have several resonance frequencies, and each of them corresponds to a mode of vibration with its mode shape. They are often driven at the first resonance frequency but the other higher frequencies can also be considered. Lochon et al. [39] proposed to use high-order modes instead of reducing dimensions to improve the sensitivity of resonant microcantilever chemical sensors.

Order of magnitude of the detected mass

Depending on the type and dimensions of the resonator used, the order of magnitude of the mass that can be detected is variable, it can go from nanograms ($10^{-9}\,g$) to yoctograms ($10^{-24}\,g$).

Nanogram-scale mass sensing is easily achievable with QCM devices. Richardson et al. [40] used a thickness-shear mode quartz resonator to measure nanogram droplets of a polymer solution.

Picogram-scale mass sensing ($10^{-12}\,g$) can be achieved with MEMS cantilever. Sone et al. [41] used an atomic force microscope cantilever to detect a mass change due to humidity variation, and they obtained a sensitivity around 2.5 pg/Hz. Johnson et al. [42] used a piezoelectric cantilever with an asymmetric electrode configuration, and the device shows a resolution of 1 pg.

Femtogram-scale mass sensing ($10^{-15}\,g$) is achievable with MEMS, but it requires more sensitive

devices. Sone et al. [43] used a piezoresistive microcantilever to measure a mass change due to antigen and antibody adsorption, and a mass resolution about 500 fg were obtained. Jin et al. [44] also used a piezoresistive cantilever with an optimized electromagnetic actuation to achieve a mass sensor with a resolution in air about 29 fg, this optimization is due to the use of high vibration mode.

For attogram-scale mass sensing ($10^{-18}\,g$), smaller devices are used and NEMS are suitable for that. Lee et al. [45] used suspended nanochannel resonators and demonstrated the measurement of mass in solution with a resolution of 27 ag. Baek et al. [18] used doubly clamped beam resonators with a minimum detectable mass around 70 ag.

Zeptogram-scale mass sensing ($10^{-21}\,g$) is still achievable as shown in some studies in the literature. Yang et al. [46] used a very high frequency NEMS for a mass sensor with a mass resolution of 7 zg. Muruganathan et al. [47] presented a zeptogram level mass sensing with a doubly clamped graphene resonator, and they measured a mass of 886 zg.

So far, the lowest scale of mass sensing is the yoctogram level. Chaste et al. [48] presented a mass sensor using carbon nanotube. It has 150 nm length and vibrates at a frequency of almost 2 GHz, and they reported mass sensing experiments with a resolution of 1.7 yg.

1.4.2 Sensing using mode localization

Principle

Unlike the previous method using a single resonator, mass sensing utilizing the mode localization is composed of coupled resonators. Mode localization is a phenomenon which was first presented by Anderson [1], and it was then studied by other authors [49, 50]. This phenomenon shows that the presence of irregularities in a periodic system can inhibit the propagation of vibrations within this system. Spletzer et al. [2] then proposed to use this phenomenon in a mass sensing capacity by presenting sensors with weakly coupled resonators. In the case of sensors with two identical coupled resonators, the device can be modeled as a two degrees of freedom mass-spring system as illustrated in Figure 1.11.

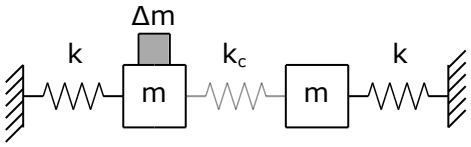

Figure 1.11: 2 degrees of freedom mass-spring system

m and k are respectively the mass and the stiffness of each resonator, and k_c is the coupling stiffness. Without perturbation, the two vibration modes of this system are the symmetric mode where the two masses vibrate in-phase, and the antisymmetric mode where the two masses vibrate out-of-phase. The

eigenfrequencies and the eigenvectors corresponding to these two modes are

$$\begin{aligned} f_1 &= \frac{1}{2\pi}\sqrt{\frac{k}{m}}, \quad u_1^0 = \frac{1}{\sqrt{2}}\begin{bmatrix} 1 \\ 1 \end{bmatrix} \\ f_2 &= \frac{1}{2\pi}\sqrt{\frac{k+2k_c}{m}}, \quad u_2^0 = \frac{1}{\sqrt{2}}\begin{bmatrix} 1 \\ -1 \end{bmatrix} \end{aligned} \tag{1.4}$$

When a small mass perturbation Δm is introduced, the vibration modes of the system change and the vibrations become localized in one of the two resonators. From [2], the relation between the relative changes in the mass and the vibration mode is given by

$$\frac{\left|u_i - u_i^0\right|}{\left|u_i^0\right|} = \left(\frac{1}{4} + \frac{1}{4\frac{k_c}{k}}\right)\frac{\Delta m}{m}, \quad i = 1, 2 \tag{1.5}$$

where u_i^0 and u_i are respectively the eigenvector of mode i before and after adding the mass perturbation. It follows from this equation that the normalized sensitivity of the device increases when the coupling ratio k_c/k decreases, which justifies the weakly coupled terminology.

Another phenomenon observed on mode localized devices is the eigenvalue loci curve veering. It was defined by some authors [51–53] as being a consequence of mode localization in weakly coupled resonators. In the case of two degrees of freedom system exhibiting two modes of vibration, it is observed when we plot the eigenvalues as a function of the parameter representing the perturbation. This perturbation can be a variation of mass or stiffness. As observed in Figure 1.12 [53], the loci of the two eigenvalues approach each other but never intersect, then they diverge abruptly.

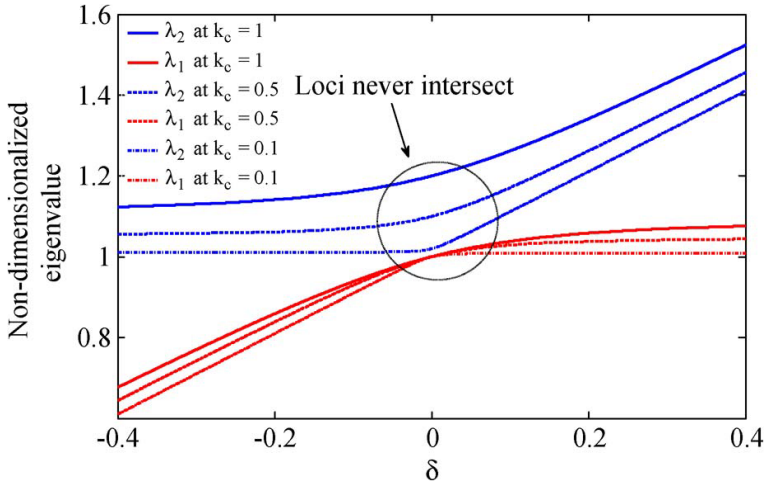

Figure 1.12: Illustration of loci veering for 2 weakly coupled resonators. δ is the normalized perturbation, λ_i is the normalized eigenvalue of the ith mode and k_c is the coupling strength [53].

Coupling

To ensure a weak coupling between the resonators of mode localized mass sensors, different kinds of coupling can be used.

Mechanical coupling consist in using a mechanical component connecting directly the resonators to each other. For coupled microbeams were the vibrations are often out of plane, the mechanical coupling can be an overhang or a coupling beam, as illustrated in Figure 1.13.

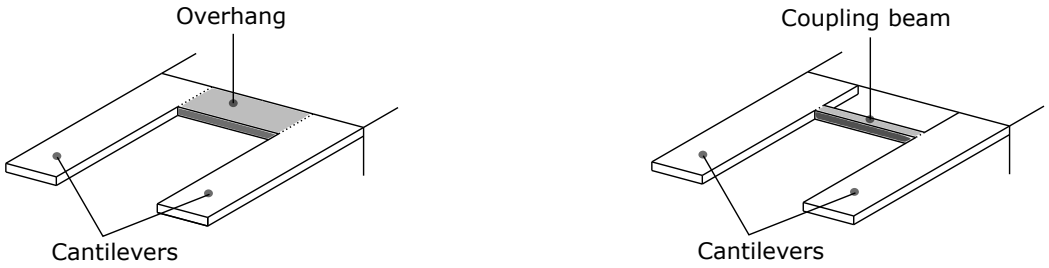

(a) Overhang (b) Coupling beam

Figure 1.13: Mechanical coupling for cantilevers

The sensor used by Spletzer et al. [2] is composed of two gold-foil cantilevers coupled by an overhang. The device is shown in Figure 1.14 and borosilicate microspheres of around 154 pg were placed on the device in order to highlight the phenomenon of mode localization. Chopard et al. [54] proposed two microcantilevers chemically etched and coupled by an overhang. Endo et al. [55] presented a self-excited coupled microcantilevers mass sensor which also uses overhang to couple two cantilevers. For devices using coupling beams, Ryan [56] proposed a sensor composed of an array of coupled cantilevers, and polystyrene microspheres were placed on the microbeams to create a mass perturbation.

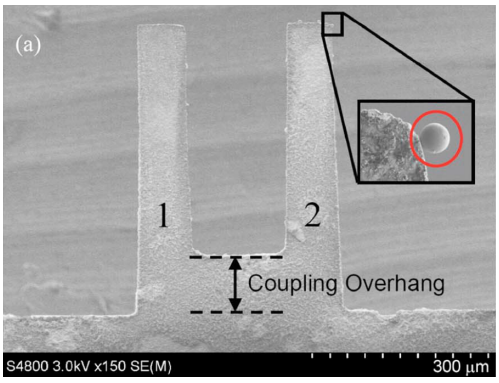

Figure 1.14: SEM image of two coupled gold-foil cantilevers [2]

Electrostatic coupling consist in using the displacement dependent electrostatic attractive force which occurs between two moving electrodes with different polarization voltages. This coupling depends on the difference in the DC polarization voltages of the two electrodes, the surface of these electrodes and the distance between them. Thiruvenkatanathan et al. [57] proposed this kind of coupling for two different sensors using a pair of electrically coupled nearly identical double-ended tuning forks and a pair of electrically coupled double-free–free-beam resonators. The DC polarization was first used to

create a stiffness perturbation, and localized vibrations were later observed. Then, they used this kind of coupling for a mass sensor composed of two ring resonators [58]. Opposite polarization voltages of $15\,V$ and $-15\,V$ were applied on both resonators, and platinium patches around $13\,pg$ were deposited to create the mass perturbation. Wood et al. [59] also proposed a mass sensor utilizing electrostatically coupled MEMS, but instead of adding a mass perturbation on the device, they used focused ion beam milling of one of the resonators to create a mass variation.

In addition to these two types of coupling, there is another one which can be qualified as a virtual coupling. This consists in coupling two resonators of different physical nature. This coupling is advantageous for resonators for which the implementation of mechanical or electrical coupling is difficult. Tao et al. [60] proposed a device which uses a MEMS resonator coupled to electrical resonators. Humbert et al. [61,62] used a mass sensor composed of a piezoelectric resonator (QCM) coupled to a digital resonator simulated with a Field Programmable Gate Array. Kasai et al. [63] proposed a device using cantilever virtually coupled to a virtual resonator that is simulated in real time by a digital computer.

Number of degrees of freedom (DoF)

The number of degrees of freedom or the number of coupled resonators is another characteristic of mode localized sensors. Almost all sensors mentioned above uses two coupled resonators, but other sensors with more degrees of freedom have been proposed by other authors.

A 3-DoF sensor was proposed by Wang et al. in [64]. The device (Figure 1.15a) is composed of three mechanically coupled cantilevers, and it is actuated with a piezoelectric ceramic plate. Polystyrene microspheres of about $10\,pg$ were deposited on one side cantilever, and they reported a significant enhancement in the amplitude change of the two unloaded cantilevers. Wang et al. [65,66] also proposed a sensor with three electrostatically coupled resonators. Under atmospheric pressure, the minimum detectable mass with the sensor was around $1.7\,ng$.

For sensors with more than three DoF, Wang et al. [67] proposed a mass sensor with a mechanically coupled beam-shaped five resonator array. For the actuation, the device (Figure 1.15b) was mounted on a piezoelectric ceramic plate. The device used by Ryan [56] used eight cantilevers connected with a coupling beam (Figure 1.15c), and a piezoelectric stack actuator was used for the actuation of all microbeams. Spletzer et al. [68] proposed a large array of mechanically coupled microbeams by using fifteen cantilevers (Figure 1.15d). They showed that the eigenmode changes were specific to the cantilever on which the mass was added, thus making it possible to identify where the mass had been added.

Extension to other sensing applications

As shown in [3], mode localization also concerns other sensing applications. It can be used in other sensors like stiffness sensors, force sensors, gyroscopes and accelerometers.

Mode localized stiffness sensors measure the change in the stiffness of a resonator. As for mass

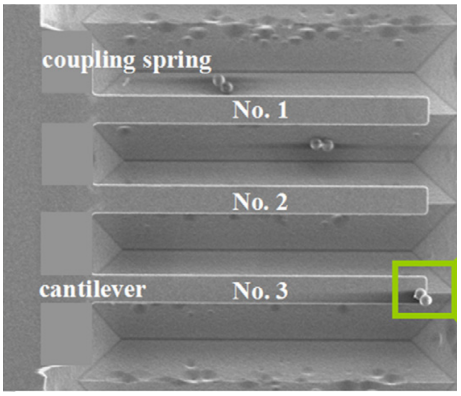

(a) 3-DoF mass sensor [64]

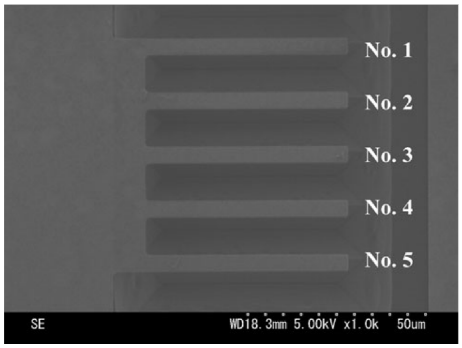

(b) 5-DoF mass sensor [67]

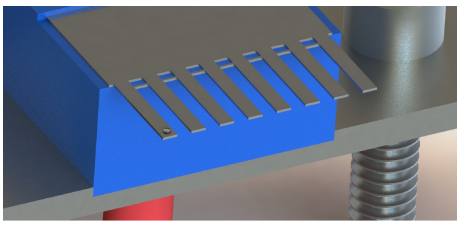

(c) Shematic of a 8-DoF mass sensor [56]

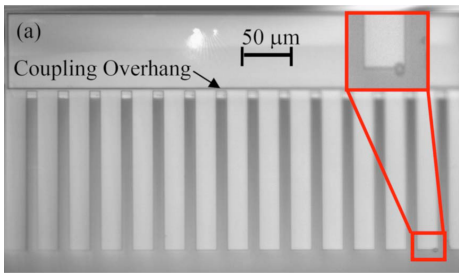

(d) 15-DoF mass sensor [68]

Figure 1.15: Mode localized mass sensors using more than two coupled resonators

perturbation, a perturbation in the stiffness of weakly coupled identical resonators also leads to a localization of vibrations. Some authors proposed this kind of sensor in order to study mode localization. Zhao et al. [69,70] proposed a 3-DoF stiffness sensor with electrostatic coupling and electrostatic actuation. For the vibration sensing, the device uses capacitive readout with comb fingers attached to the resonators. The motional current was measured with a transimpedance amplifier. The stiffness perturbation is introduced by changing the DC applied voltage of one resonator. Zhang et al. [71,72] proposed a stiffness sensor using two mechanically coupled resonator. The device also uses capacitive readout requiring feedthrough cancellation.

Force sensors based on mode localization were proposed by some authors. Thiruvenkatanathan et al. [73] presented an electrometer that can be adapted for force monitoring. The device uses a pair of weakly coupled double-ended tuning fork resonators. By introducing charge across an input capacitor on one resonator, a differential axial strain which perturbs the stiffness of the resonator is induced. From this input charge, the applied electrostatic force can be calculated. Zhao et al. [74] presented a force sensor with three coupled resonators. The force perturbation is introduced by applying DC voltage to one resonator.

In the literature, we have sensors for acceleration sensing and based on mode localization. Pai et al. [75] demonstrated the use of two resonators magnetically coupled to sense rotations. The device is composed of electroplated copper cantilevers coupled with magnetic field of rare earth magnets, and they demonstrated that the device can be used to detect an in-plane rotation. For linear acceleration sensing, Zhang et al. [76] proposed a method using two weakly coupled resonators. The principle con-

sists in using the displacement due to the acceleration of a proof mass to create differential electrostatic stiffness perturbations on the coupled resonators. Pandit et al. [77] also proposed 2-DoF accelerometer with a bias stability of $7\,\mu g$ (where g is the gravitational acceleration). Other authors proposed accelerometers with a higher DoF by using three [78] or four [79] resonators.

Actuation scheme

As we have multiple resonators in mode localized sensors, the device can be actuated in different ways.

For 2-DoF sensors, we can have devices with only one resonator driven (Figure 1.16a), two resonators driven by in-phase forces (Figure 1.16b) and two resonators driven by out-of-phase forces (Figure 1.16c). As shown by simulation results in Figure 1.16d, the actuation with single driven resonator allows us to have the symmetric and the antisymmetric modes in the frequency responses when there is no perturbation. With the in-drive scheme, we only have the symmetric mode and the vibrations of the two resonators are always in-phase (Figure 1.16e). With the out-drive scheme, we only have the antisymmetric mode and the vibrations of the two resonators are always out-of-phase (Figure 1.16f). Zhang et al. [72] investigated these three schemes of actuation in a sensor for stiffness change.

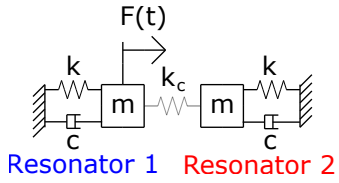

(a) Single resonator driven

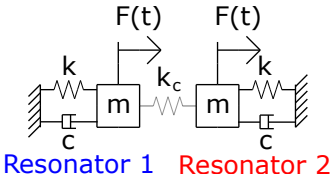

(b) Two resonators driven by in-phase forces

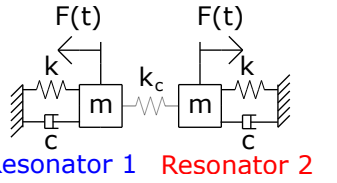

(c) Two resonators driven by out-of-phase forces

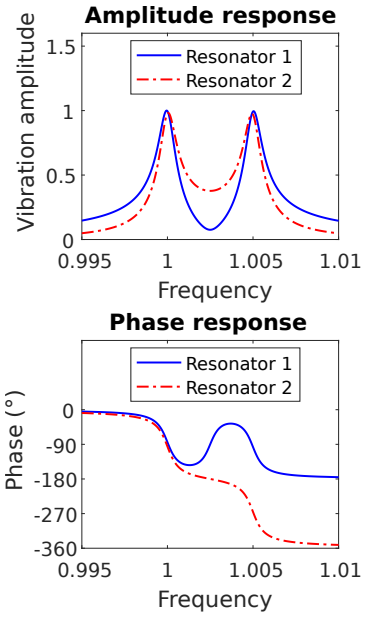

(d) Frequency responses for single drive scheme

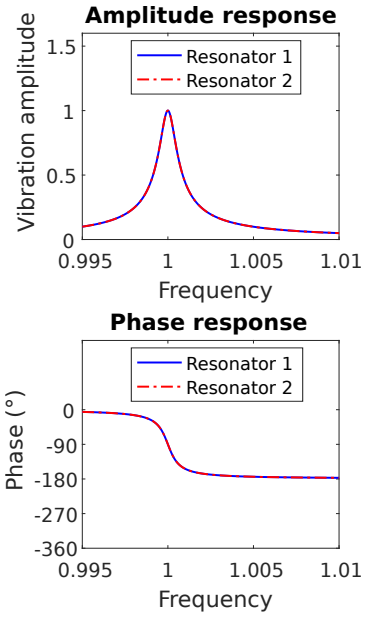

(e) Frequency responses for in-drive scheme

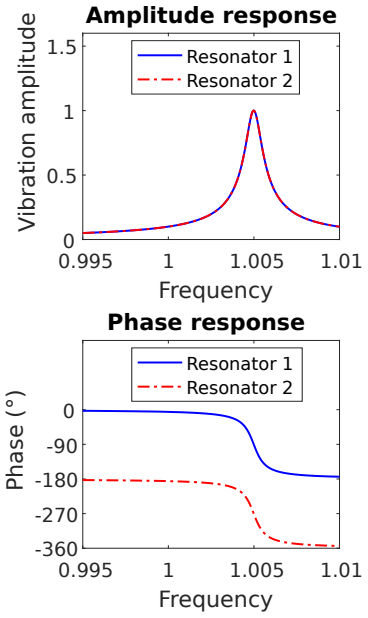

(f) Frequency responses for out-drive scheme

Figure 1.16: Actuation for 2-DoF mode localized mass sensors

In addition to these three actuation schemes, one can also have a case where each resonator is actuated with forces having a phase shift of $\pi/2$. This was proposed by Humbert et al. [61, 62, 80] for the actuation of a system involving physical and digital resonators.

For devices with a higher DoF, Zhao et al. [69] only actuate the side resonator of 3-DoF stiffness sensor. But for the other devices presented by other authors, they almost all use a piezoelectric actuation to drive all resonators at the same time. This corresponds to the in-drive scheme presented previously.

Output metrics

As we have multiple vibration modes in addition to the number of the resonators, we can also use different output metrics to measure the added perturbation in mode localized sensors. Zhao et al. [81] investigated the characteristics of different output metrics for weakly coupled resonators. These output metrics include the amplitude difference, the amplitude ratio and the eigenstate shift.

The difference between the amplitudes of two resonators for a given mode can be used to determine the added perturbation. For small perturbation, this output metric is a linear function of the mass change or stiffness. But with important perturbation, it becomes nonlinear with a decreasing sensitivity. Liu et al. [82] used this output metric in a coupled 5-beam array for force detection application.

The amplitude ratio is often used for mode localized sensors. It was first proposed by Gil-Santos et al. [83] as the quotient between the amplitudes of the same resonator at two different modes. As this requires a frequency sweep which is not suitable for a real time sensing, another approach that consists in calculating the ratio of two different resonators for a given mode was proposed [81]. It shows nonlinearity for very small perturbation, but becomes linear when the perturbation increases. Zhang et al. [84] proposed to use the algebraic summation of the amplitude ratios of two modes to suppress this nonlinearity.

Eigenstate shift was the first output metric used for mode localized sensors. It is an amplitude vector composed of the vibrational amplitudes of all the resonators of the system for a given vibration mode. We then use the relative change of this vector to calculate the perturbation. Like the amplitude difference, it is linear only for small perturbations.

In addition to these output metrics, there are other authors who propose to measure frequencies instead of amplitudes [85]. It consists in an inverse eigenvalue sensing based on the eigenfrequencies of one resonator only.

1.4.3 Other methods of mass sensing

In addition to the previous methods, we also have other mass sensing techniques for MEMS.

Bifurcation based mass sensing

Bifurcation based mass sensors use the amplitude jump of nonlinear resonators operating near saddle node bifurcation points, in order to detect masses. Nonlinear resonators can exhibit two types of frequency response, which correspond to a softening behavior (Figure 1.17a) and a hardening behavior (Figure 1.17b). The principle of this method consists in driving the device near point A_1 or point A_2 shown in these figures. When we add a small mass, the resonance frequency of the resonator decreases. This then induces a jump from point A_1 to point B_1 for the device with softening behavior, and from point A_2 to point B_2 for the device with hardening behavior. Consequence of this is a sudden change in the amplitude response, which can be used to detect the perturbation. But as the amplitude change is not proportional to the perturbation, it is not suitable for mass sensing.

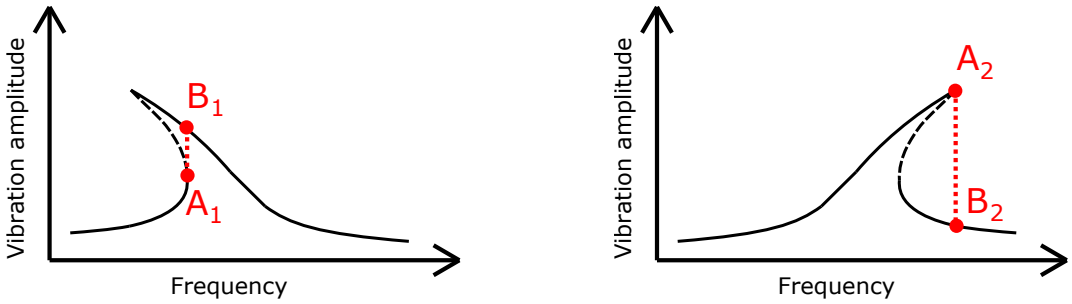

(a) Softening behavior (b) Hardening behavior

Figure 1.17: Bifurcation based mass sensing principle

The principle using resonators with softening behavior was first proposed by Kumar et al. [86, 87]. They used piezoelectrically actuated microcantilever to prove the concept. Nguyen et al. [88] then investigated this techniques by considering the two cases of nonlinear frequency responses. Al-Ghamdi et al. [89] have also proposed a MEMS gas sensor using dynamic bifurcation detection technique, but it uses the qualitative difference between the sensor state before and after the dynamic pull-in bifurcation.

Another similar mass sensing method was proposed by Zhang et al. [90, 91], but it is based on a frequency shit of a resonator driven near first order parametric resonance (twice the natural frequency). The mass perturbation is measured from the frequency shift at the first order parametric resonance tongue. A high sensitivity is achievable with this method thanks to the important amplitude jump caused by the parametric resonance.

Mass sensing using static mode of cantilevers

All of the above mentioned mass sensors use a resonator operating in dynamic mode. But mechanical resonators such as cantilevers can be used in static mode for mass sensing. As illustrated in Figure 1.18, the principle consists in measuring the static deflection of the cantilever due to the stress change caused by molecular adsorption.

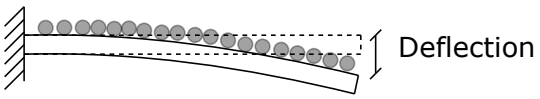

Figure 1.18: Static mode operation of cantilever mass sensor

The relation between the deflection Δw of the cantilever and the surface stress $\Delta\sigma$ is given in [92] by

$$\Delta w = \frac{3\,(1-\nu)\,L^2}{Eh^2}\Delta\sigma \tag{1.6}$$

where ν is the Poisson's ratio, E is the Young modulus, L the cantilever length and h its thickness. To measure the deflection, we can use piezoresistive methods [93], optical methods [94], capacitive methods [95] or interferometric methods [96].

1.5 Advantages of mode localization and problems encountered in mode localized sensors

As we have seen, mass sensors have different operating principles, but mode localization appears to be a novel technique that differs from the others because it uses more than one resonator. In this section, we present the main advantages of mode localization, but we also identify the problems encountered on existing mode localized sensors.

1.5.1 Advantages of mode localization

High normalized sensitivity

From Equation (1.3), the normalized sensitivity of mass sensors using frequency shift with a single resonator is given by

$$S_{1DoF} = \frac{\Delta f_0}{f_0} * \frac{m}{\Delta m} = \frac{1}{2} \tag{1.7}$$

while for mode localized sensors with 2 DoF , it is given from Equation (1.5) by,

$$S_{2DoF} = \frac{\left|u_i - u_i^0\right|}{\left|u_i^0\right|} * \frac{m}{\Delta m} = \left(\frac{1}{4} + \frac{1}{4\frac{k_c}{k}}\right) \approx \frac{k}{4k_c}, \quad i = 1,2 \tag{1.8}$$

It follows that for mode localized sensors where the coupling ratio k_c/k can be under 1%, the normalized sensitivity can be two to three orders of magnitude higher than that of sensors using frequency shift.

Common mode rejection

The advantage of using multiple resonators is the common mode rejection capability. Compared to single resonator devices, mode-localized sensors are less sensitive to changes in ambient conditions. A change in ambient conditions like temperature can induce a change in stiffness, thus creating an output

offset if the mass sensor uses a frequency variation. For 2 DoF mode localized sensors, this changes the effective stiffness of both resonators if they are of the same physical nature, but there is no output shift because the symmetry is not broken. Thiruvenkatanathan et al. [97] demonstrated it experimentally by using a pair of electrically coupled flexural wine glass mode ring resonators. They have shown that the eigenstates remain relatively constant to variations in ambient temperature and pressure, increasing relative robustness to environmental drift. Pandit et al. [98] also studied the common mode rejection by considering mechanically coupled and electrically coupled resonators.

1.5.2 Problems encountered in mode localized MEMS sensors

Issues related to microfabrication

The mode localization uses system with weakly coupled identical resonators. We have seen that for 2 DoF sensors, the vibration modes of the system without perturbation are the symmetric and the antisymmetric modes, which correspond to the veering point. They appear when the two resonators have exactly the same effective mass and stiffness. But as seen in Section 1.2.5, the relative tolerance of micromachining increases when the size of the device decreases, and the manufacturing defects become non-negligible. Consequently, the device is initially unbalanced, and localized vibrations take place without any additional mass perturbation. An example highlighting this problem is the frequency response of the device considered in [2], which is shown in Figure 1.19.

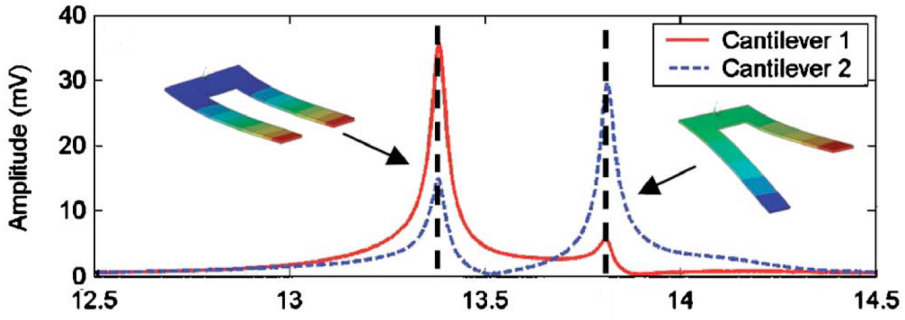

Figure 1.19: Amplitude response of the sensor used in [2]

For two coupled identical resonators driven by in-phase forces, Figure 1.16 in Section 1.4.2 shows that the frequency response of the system should only exhibit one resonance peak corresponding to the symmetric mode where the amplitudes of the two resonators are identical. The results obtained in Figure 1.19 is caused by manufacturing tolerances which induce a slight difference in the dimensions of the two cantilevers, thus introducing an initial imbalance.

Design of the mechanical coupling

We have seen that the devices presented in the literature use overhang and coupling beam to couple resonators with out of plane vibrations like cantilevers. But their designs are not accurately modeled. Most studies with a mode localized sensor have a mass-spring system for their model, but the param-

eters used in the model are not explicitly related to the geometry of the device and in particular the coupling stiffness. As the coupling is a parameter which defines the sensitivity of the device, it needs to be correctly designed.

Sensitivity limitation

For 2 DoF devices, Equation (1.8) shows that the normalized sensitivity is better when the coupling ratio k_c/k decreases. However, the more the coupling decreases, the closer the frequencies of the two vibration modes are to each other. Due to the energy loss that defines the quality factor of the device, this coupling ratio has a minimum value that prevents the mode aliasing. This corresponds to the minimum coupling that allows the separation between the peaks of each vibration mode. Thiruvenkatanathan et al. [99] proposed a practical value of this minimum coupling to be equal to $1/Q$, where Q is the quality factor of the device. As illustrated in Figure 1.20, the two peaks corresponding to the two vibration modes are distinguishable when the separation between them is higher than the bandwidth.

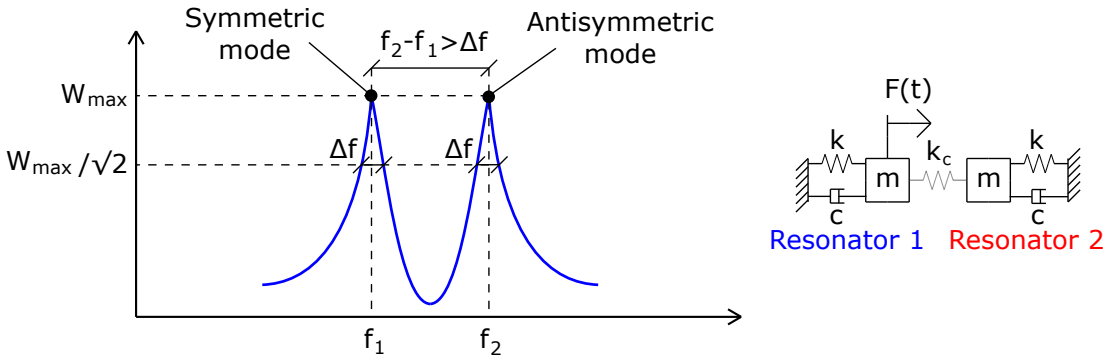

Figure 1.20: Minimum coupling for 2 DoF mass-spring system

For this system, we have the following relations

$$f_1 = \frac{1}{2\pi}\sqrt{\frac{k}{m}}; \quad f_2 = \frac{1}{2\pi}\sqrt{\frac{k+2k_c}{m}} \approx f_1\left(1+\frac{k_c}{k}\right) \tag{1.9}$$

$$Q = \frac{f_1}{\Delta f} \tag{1.10}$$

where k and m are respectively the stiffness and mass of each resonator, k_c is the stiffness of the coupling spring, f_1 and f_2 are respectively the frequencies of the symmetric and the antisymmetric mode, Δf is the bandwidth. To prevent the mode the aliasing, we should have $f_2 - f_1 > \Delta f$. From Equation (1.9) and Equation (1.10), we obtain

$$f_1\left(1+\frac{k_c}{k}\right) - f_1 > \frac{f_1}{Q} \tag{1.11}$$

So

$$\frac{k_c}{k} > \frac{1}{Q} \tag{1.12}$$

Resolution limitation

We have seen in Section 1.4.2 that we have different output metrics which allow us to measure the mass perturbation with mode localized sensors. But whatever we choose, all of them are based on vibration amplitude measurement. So the minimal detectable mass depends directly on the minimal detectable amplitude variation. Consequently, the dynamic range of the device limits its mass resolution. A device with a higher dynamic range is therefore required to detect a smaller mass perturbation.

1.6 Summary

In this chapter, a state of the art on MEMS devices and their fabrication has been conducted. We have also reviewed MEMS mass sensors and different mass sensing methods. At the end of the literature review, it was concluded that the mode localization appears to be a promising technique due to the benefits that it brings. The main advantages of mode localized sensors are their normalized sensitivity that can be two to three orders of magnitude higher than that of sensors using frequency shift, and their insensitivity to the change in ambient conditions. But four main problems encountered on current mode localized mass sensors have been identified. It concerns the fabrication of these sensors, their design, their sensitivity and their mass resolution. The following chapters will then deal with the proposed solutions to these problems. We consider two different MEMS devices for that, and the first one will be presented in the next chapter.

Chapter 2

The proposed device using attractive electrostatic forces: design and modeling

Contents

2.1 Introduction

In this chapter, we present the first device proposed in this work, which can bring solutions to the problems encountered on existing mode localized mass sensors. We have seen earlier that the main problem of 2DoF sensors is the manufacturing defects that introduce an initial disorder in the device. To counterbalance them, we propose a solution which consists in an initial asymmetric device, which will then be balanced with an electrostatic actuation using attractive forces. Cantilevers are often used, so we proposed a device composed of two cantilevers with different lengths. As illustrated in the equivalent mass-spring system of the device in Figure 2.1, the short cantilever has a smaller effective mass and a higher effective stiffness with this configuration.

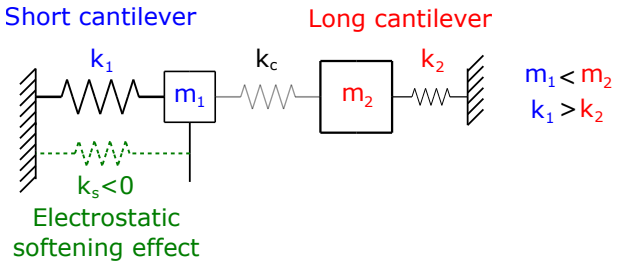

Figure 2.1: Equivalent mass-spring system of the proposed device composed of two coupled cantilevers with different lengths

As the short cantilever is electrostatically actuated with a combined AC-DC voltage, we use the softening effect of the electrostatic force to reduce its effective stiffness. By applying the appropriate DC voltage, we can counterbalance the length difference and the manufacturing defects, and reach the veering point. Tuning the DC voltage to counterbalance defects can be realized with two resonators with the same dimensions, but using an initial asymmetric device allows us to know which one is the stiffest and needs electrostatic softening. Preliminary study of this principle has already been made by Walter et al. [100] by using finite element model. In this work, we propose an analytical model based on Euler-Bernoulli beam theory to design the device.

We have also seen that the mechanical coupling is generally not modeled on the basis of its geometry. This modeling can be difficult in the case of an overhang coupling. So, we propose to use a coupling beam to connect the two cantilevers of the proposed device, and it is taken into account in the analytical model.

As electrostatic nonlinearities are often present in electrostatic actuation with attractive forces, we also take them into account in the analytical model.

2.2 Presentation of the device and the model

2.2.1 Device and model

As described in Figure 2.2a, the proposed device which uses attractive electrostatic forces is composed of two cantilevers with lengths L_1 and L_2 ($L_1 < L_2$), a width b, and a thickness h. They are connected

by a coupling beam with a length L_c, a width b_c, and a thickness h. It is located at a distance $\tilde{x}_c$ from the fixed end of each cantilever. We generate the vibration by applying a combined AC-DC voltage to the electrode located at a distance g from the short cantilever. To model this device, we use two Euler-Bernoulli beams connected by a rotational spring which is located at a distance $\tilde{x}_c$ from the fixed end of the cantilevers (Figure 2.2b).

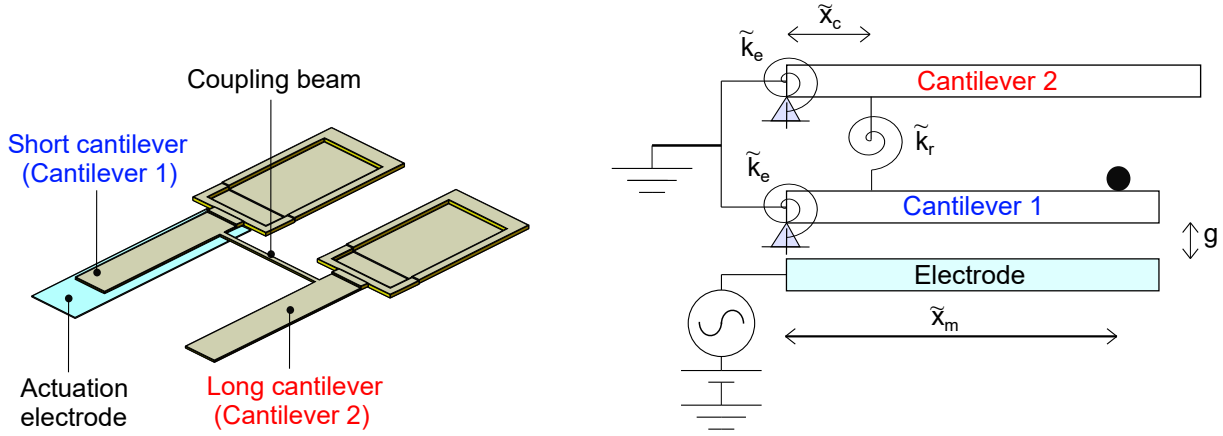

(a) The device using attractive electrostatic forces

(b) Model of two coupled beams with an added discrete point mass and an electrostatic actuation

Figure 2.2: Device and model

In the model, the torsional stiffness $\tilde{k}_r$ of the rotational spring represents the torsional stiffness of the coupling beam, and it is expressed as

$$\tilde{k}_r = \frac{G\beta b_c h^3}{L_c} \tag{2.1}$$

where G is the shear modulus, and β is a coefficient for the torsion of beams with a rectangular cross section [101]. This coefficient depends on the ratio between b_c and h, and it is calculated from the table in Appendix A.2. The coupling beam is subjected to both bending and torsion, and we should also add a translational spring to model it. But in our case, it is near the fixed end and we assume that the dominant stress is the torsion. So, the bending stiffness of the coupling beam is neglected in the model.

We often have a difference between theoretical and experimental natural frequencies when modeling beams. It is due to the surface micromachining process which does not allow ideal clamping conditions to be achieved. In order to consider this, we introduce a torsional stiffness $\tilde{k}_e$ at the supposed fixed ends of each cantilever. Normally, a complete model of the non-ideal boundary condition should include a translational spring [102, 103] because it allows small deflection and rotation at the fixed end. But we assume that the small deflection at the fixed end can be neglected.

To consider the mass perturbation, we also add a discrete point mass on the short cantilever, and it is located at a distance $\tilde{x}_m$ from the fixed end.

2.2.2 Dimensions of the device

For the manufacturing, we use the MUMPS® process described on Section 1.2.3, and this allows us to define some dimensions of the device imposed by the design rule of this process. The first dimension is the thickness of the microbeams which is equal to that of the structural layer used. By using the Poly2 for that, we should have the thickness given in Table 1.1. But it decreases slightly due to the etching process, and we measure a thickness of $1.30\,\mu m$. The second dimension concerns the capacitor gap. If we use the two layers of oxide as sacrificial layers, we should have a gap equal to the sum of the thicknesses of these two layers. But it also decreases due to the etching process, and we obtain a gap around $1.20\,\mu m$. The last dimension is the width of the coupling beam. We should decrease its section in order to have a weak coupling, but its width has to be greater than the smallest size imposed by the etching. The nominal feature for the Poly2 is equal to $3\,\mu m$, so we choose this value for the coupling beam width. Concerning the other dimensions of the two cantilevers, we set their width at $20\,\mu m$, and the length of the longer one at $100\,\mu m$, in order not to have a too slender structure. With this dimensions, the beam theory can still be applied, and the mass of the cantilevers is maximized in relation to that of the coupling beam. Finally, the dimensions of the device are given in Table 2.1, and the others that have not yet been defined will be determined later.

Table 2.1: Dimensions of the device using attractive electrostatic forces

Dimension	Designation	Value
Length of the short cantilever	L_1	-
Length of the long cantilever	L_2	$100\,\mu m$
Width of the cantilevers	b	$20\,\mu m$
Thickness of the cantilevers	h	$1.30\,\mu m$
Length of the coupling beam	L_c	-
Width of the coupling beam	b	$3\,\mu m$
Position of the coupling beam	$\tilde{x}_c$	-
Gap	g	$1.20\,\mu m$

2.3 Design of the coupling beam

To design the coupling beam, we first validate the proposed model of the coupling beam by carrying out a free vibration analysis and comparing the results with a finite element model. Then, we choose the appropriate length and position of the coupling beam according to the minimum coupling ratio.

2.3.1 Free vibration analysis

Eigenfrequency

To determine the eigenfrequency of the coupled cantilevers, we use the model in Figure 2.2b. But as illustrated in Figure 2.3, the discrete point mass and the electrostatic actuation are removed.

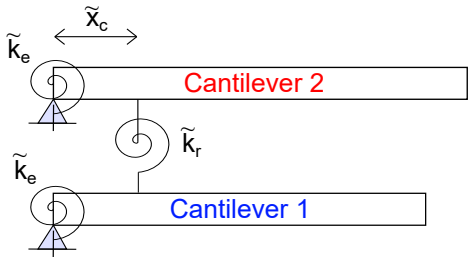

Figure 2.3: Model of two cantilevers connected by a rotational spring

Many authors have already studied the natural vibration of Euler-Bernoulli beams attached with mass-spring system [104–108], or a beam carrying lumped elements [109–113]. Some of them use the Green's function method to determine the natural frequencies of the system.The others studied separately each portion of the beams (before and after the spring) and continuity conditions at the attachment spring points are then applied. In our case, the second method is applied and each cantilever in Figure 2.3 is separated in two parts (before and after the connection with the rotational spring $\tilde{k}_r$). The equation governing the free undamped bending vibration of the system is given by

$$\begin{aligned} EI\tilde{w}_{1,1}'''' + \rho bh\ddot{\tilde{w}}_{1,1} = 0 \quad \text{for} \quad 0 \le \tilde{x} \le \tilde{x}_c \\ EI\tilde{w}_{1,2}'''' + \rho bh\ddot{\tilde{w}}_{1,2} = 0 \quad \text{for} \quad \tilde{x}_c \le \tilde{x} \le L_1 \\ EI\tilde{w}_{2,1}'''' + \rho bh\ddot{\tilde{w}}_{2,1} = 0 \quad \text{for} \quad 0 \le \tilde{x} \le \tilde{x}_c \\ EI\tilde{w}_{2,2}'''' + \rho bh\ddot{\tilde{w}}_{2,2} = 0 \quad \text{for} \quad \tilde{x}_c \le \tilde{x} \le L_2 \end{aligned} \tag{2.2}$$

where primes and dots denote respectively the partial differentiation with respect to the position along the microbeam $\tilde{x}$ and to the time $\tilde{t}$, E is the Young's modulus, I is the moment of inertia of the cross section of the cantilevers, $\tilde{w}_{1,1}$ and $\tilde{w}_{1,2}$ are the deflection of the first cantilever, $\tilde{w}_{2,1}$ and $\tilde{w}_{2,2}$ are the deflection of the second cantilever, and ρ is the material density.
By separating temporal and spatial variables, we have for $i = 1, 2$ and $j = 1, 2$

$$\tilde{w}_{i,j}\left(\tilde{x}, \tilde{t}\right) = \phi_{i,j}\left(\tilde{x}\right) * \cos\left(\tilde{\omega}\tilde{t}\right) \tag{2.3}$$

where $\phi_{i,j}\left(\tilde{x}\right)$ is the mode shape of each portion of cantilever i, and $\tilde{\omega}$ is the eigen angular frequency of the system.
The expression of the mode shape is

$$\begin{aligned} \phi_{i,1}\left(\tilde{x}\right) = A_i \cos\left(\tilde{\lambda}\tilde{x}\right) + B_i \sin\left(\tilde{\lambda}\tilde{x}\right) + C_i \cosh\left(\tilde{\lambda}\tilde{x}\right) + D_i \sinh\left(\tilde{\lambda}\tilde{x}\right) \\ \phi_{i,2}\left(\tilde{x}\right) = P_i \cos\left(\tilde{\lambda}\left(\tilde{x} - L_i\right)\right) + Q_i \sin\left(\tilde{\lambda}\left(\tilde{x} - L_i\right)\right) + R_i \cosh\left(\tilde{\lambda}\left(\tilde{x} - L_i\right)\right) + S_i \sinh\left(\tilde{\lambda}\left(\tilde{x} - L_i\right)\right) \end{aligned} \tag{2.4}$$

The boundary conditions of each cantilevers can be written as

$$\begin{aligned} \phi_{i,1}(0) &= 0 \\ EI\phi''_{i,1}(0) &= \tilde{k}_e \phi'_{i,1}(0) \\ \phi''_{i,2}(L_i) &= 0 \\ \phi'''_{i,2}(L_i) &= 0 \end{aligned} \tag{2.5}$$

By considering these conditions, we have the following relationships

$$\begin{aligned} C_i &= -A_i \\ D_i &= -\frac{2EI\tilde{\lambda}}{\tilde{k}_e} A_i - B_i \\ R_i &= P_i \\ S_i &= Q_i \end{aligned} \tag{2.6}$$

and the mode shapes in Equation (2.4) become

$$\begin{aligned} \phi_{i,1}(\tilde{x}) &= A_i \left[\cos\left(\tilde{\lambda}\tilde{x}\right) - \cosh\left(\tilde{\lambda}\tilde{x}\right) - \frac{2EI\tilde{\lambda}}{\tilde{k}_e} \sinh\left(\tilde{\lambda}\tilde{x}\right) \right] + B_i \left[\sin\left(\tilde{\lambda}\tilde{x}\right) - \sinh\left(\tilde{\lambda}\tilde{x}\right) \right] \\ \phi_{i,2}(\tilde{x}) &= P_i \left[\cos\left(\tilde{\lambda}(\tilde{x} - L_i)\right) + \cosh\left(\tilde{\lambda}(\tilde{x} - L_i)\right) \right] + Q_i \left[\sin\left(\tilde{\lambda}(\tilde{x} - L_i)\right) + \sinh\left(\tilde{\lambda}(\tilde{x} - L_i)\right) \right] \end{aligned} \tag{2.7}$$

Let's consider now the attachment point of the rotational spring $\tilde{k}_r$ which connects the two cantilevers (for $\tilde{x} = \tilde{x}_c$), the conditions between the deflections, the slopes, the bending moments and the shear forces of each portion of each cantilever give us the eight following relationships

$$\begin{aligned} \phi_{1,1}(\tilde{x}_c) &= \phi_{1,2}(\tilde{x}_c) \\ \phi'_{1,1}(\tilde{x}_c) &= \phi'_{1,2}(\tilde{x}_c) \\ \phi''_{1,1}(\tilde{x}_c) + \frac{\tilde{k}_r}{EI}\left[\phi'_{1,1}(\tilde{x}_c) - \phi'_{2,1}(\tilde{x}_c)\right] &= \phi''_{1,2}(\tilde{x}_c) \\ \phi'''_{1,1}(\tilde{x}_c) &= \phi'''_{1,2}(\tilde{x}_c) \\ \phi_{2,1}(\tilde{x}_c) &= \phi_{2,2}(\tilde{x}_c) \\ \phi'_{2,1}(\tilde{x}_c) &= \phi'_{2,2}(\tilde{x}_c) \\ \phi''_{2,1}(\tilde{x}_c) + \frac{\tilde{k}_r}{EI}\left[\phi'_{2,1}(\tilde{x}_c) - \phi'_{1,1}(\tilde{x}_c)\right] &= \phi''_{2,2}(\tilde{x}_c) \\ \phi'''_{2,1}(\tilde{x}_c) &= \phi'''_{2,2}(\tilde{x}_c) \end{aligned} \tag{2.8}$$

For convenience, we set

$$\begin{aligned}\phi_{i,1}(\tilde{x}) &= A_i f_{i,1}(\tilde{x}) + B_i g_{i,1}(\tilde{x}) \\ \phi_{i,2}(\tilde{x}) &= -P_i f_{i,2}(\tilde{x}) - Q_i g_{i,2}(\tilde{x})\end{aligned} \tag{2.9}$$

where

$$\begin{aligned}f_{i,1}(\tilde{x}) &= \cos\left(\tilde{\lambda}\tilde{x}\right) - \cosh\left(\tilde{\lambda}\tilde{x}\right) - \frac{2EI\tilde{\lambda}}{\tilde{k}_e}\sinh\left(\tilde{\lambda}\tilde{x}\right) \\ g_{i,1}(\tilde{x}) &= \sin\left(\tilde{\lambda}\tilde{x}\right) - \sinh\left(\tilde{\lambda}\tilde{x}\right) \\ f_{i,2}(\tilde{x}) &= -\cos\left(\tilde{\lambda}(\tilde{x}-L_i)\right) - \cosh\left(\tilde{\lambda}(\tilde{x}-L_i)\right) \\ g_{i,2}(\tilde{x}) &= -\sin\left(\tilde{\lambda}(\tilde{x}-L_i)\right) - \sinh\left(\tilde{\lambda}(\tilde{x}-L_i)\right)\end{aligned} \tag{2.10}$$

By replacing these expressions in Equation (2.8), we finally have the matrix equation below at $\tilde{x} = \tilde{x}_c$

$$\left[\ M\ \right] * \begin{bmatrix} A_1 \\ B_1 \\ P_1 \\ Q_1 \\ A_2 \\ B_2 \\ P_2 \\ Q_2 \end{bmatrix} = \begin{bmatrix} 0 \\ 0 \\ 0 \\ 0 \\ 0 \\ 0 \\ 0 \\ 0 \end{bmatrix} \tag{2.11}$$

where

$$\left[\ M\ \right] = \begin{bmatrix} f_{1,1} & g_{1,1} & f_{1,2} & g_{1,2} & 0 & 0 & 0 & 0 \\ f'_{1,1} & g'_{1,1} & f'_{1,2} & g'_{1,2} & 0 & 0 & 0 & 0 \\ f''_{1,1} + \frac{\tilde{k}_r}{\mathrm{EI}} f'_{1,1} & g''_{1,1} + \frac{\tilde{k}_r}{\mathrm{EI}} g'_{1,1} & f''_{1,2} & g''_{1,2} & -\frac{\tilde{k}_r}{\mathrm{EI}} f'_{2,1} & -\frac{\tilde{k}_r}{\mathrm{EI}} g'_{2,1} & 0 & 0 \\ f'''_{1,1} & g'''_{1,1} & f'''_{1,2} & g'''_{1,2} & 0 & 0 & 0 & 0 \\ 0 & 0 & 0 & 0 & f_{2,1} & g_{2,1} & f_{2,2} & g_{2,2} \\ 0 & 0 & 0 & 0 & f'_{2,1} & g'_{2,1} & f'_{2,2} & g'_{2,2} \\ -\frac{\tilde{k}_r}{\mathrm{EI}} f'_{1,1} & -\frac{\tilde{k}_r}{\mathrm{EI}} g'_{1,1} & 0 & 0 & f''_{2,1} + \frac{\tilde{k}_r}{\mathrm{EI}} f'_{2,1} & g''_{2,1} + \frac{\tilde{k}_r}{\mathrm{EI}} g'_{2,1} & f''_{2,2} & g''_{2,2} \\ 0 & 0 & 0 & 0 & f'''_{2,1} & g'''_{2,1} & f'''_{2,2} & g'''_{2,2} \end{bmatrix} \tag{2.12}$$

The existence of non-trivial solutions for Equation (2.11) requires :

$$det\left[\ M\ \right] = 0 \tag{2.13}$$

Solving this equation allows us to calculate all values of $\tilde{\lambda}$, and the eigenfrequency f_n of the nth mode

of the system is given by

$$f_n = \frac{\left(\tilde{\lambda}_n\right)^2}{2\pi}\sqrt{\frac{EI}{\rho bh}} \tag{2.14}$$

Comparison with a finite element model

In order to validate the model of the coupling beam, we use a finite element model of the coupled cantilevers with *Cast3M*. The model uses beam elements and the script is given in Appendix A.3. The device is made with polysilicon and the parameters used are given in Table 2.2. For the material properties of the polysilicon, we use values given in [114].

Table 2.2: Parameters used

Property	Designation	Value
Young's modulus	E	$163\,GPa$
Poisson's ratio	ν	0.22
Shear modulus	G	$67\,GPa$
Density	ρ	$2320\,kg/m^3$

For the dimensions of the device, we first use two cantilevers with the same length ($L_1 = L_2 = 100\,\mu m$) because the study of the coupling concerns the balanced system. The coupling beam has a length of $L_c = 65\,\mu m$, and three different values of its position $\tilde{x}_c$ are considered ($5.5\,\mu m$, $10.5\,\mu m$ and $15.5\,\mu m$). Only an experimental investigation would make it possible to determine the value of the torsional stiffness $\tilde{k}_e$, which allows the non-ideal aspect of the clamping condition to be taken into account in the model. So at this stage, a value of $\tilde{k}_e = 3\ 10^{-7}\,Nm/rad$ is taken. This value reduces the eigenfrequency of the model at 96 % of the eigenfrequency of the model with fully clamped cantilevers ($\tilde{k}_e = \infty$). The mode shapes corresponding to the symmetric and the antisymmetric modes are illustrated in Figure 2.4.

(a) Symmetric mode (b) Antisymmetric mode

Figure 2.4: Mode shapes of two coupled cantilevers

For the analytical model, we take the same material properties and dimensions, and the eigenfrequencies are calculated by solving Equation (2.13) with MATLAB® R2019. The results are shown in Table 2.3.

Table 2.3: Eigenfrequencies of the in-phase and the out-of-phase modes

$\tilde{x}_c$ (μm)	In-phase mode		Out-of-phase mode	
	f_1 theoretical (kHz)	f_1 FEM (kHz)	f_2 theoretical (kHz)	f_2 FEM (kHz)
5.5	169.398	169.392	170.288	170.306
10.5	169.398	169.383	171.676	171.861
15.5	169.398	169.357	173.507	174.215

By comparing frequencies, errors of less than 0.4 % are obtained, so the analytical model gives a good approximation. The error increases slightly as the coupling beam moves away from the fixed end because then the effects of its mass and bending stiffness become non-negligible.

2.3.2 Minimum coupling ratio

According to the expression of the eigenfrequencies of the equivalent discrete mass-spring system, the coupling ratio k_c/k of the coupled cantilevers can be determined by using the following relationship

$$\frac{k_c}{k} = \frac{1}{2}\left(\left(\frac{f_2}{f_1}\right)^2 - 1\right) \tag{2.15}$$

So, we use the eigenfrequencies given by the analytical model to calculate this parameter as a function of the position and the length of the coupling beam ($\tilde{x}_c$ and L_c). The results are shown in Figure 2.5.

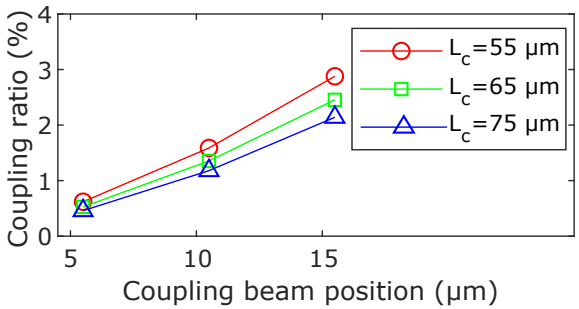

Figure 2.5: Coupling ratio as a function of the position and the length of the coupling beam

We notice that the coupling ratio is weaker when the coupling beam is near the fixed end, or when its length increases, but the influence of the length is not very important. According to [99], the practical minimum coupling ratio preventing mode aliasing is equal to the inverse of the quality factor. Recent work [115, 116] has shown that mass detection with mode-localized sensors is worse than with a single resonator when the coupling ratio is below this limit. As the quality factor of the device under vacuum is estimated to be around 500, the minimum coupling ratio is about $k_{c\,min}/k = 0.2\,\%$. Thus, the position of the coupling beam that is suitable for the device seems to be closer to $\tilde{x}_c = 5.5\,\mu m$.

2.4 Design of the length of the short cantilever

To design the length of the short cantilever, we determine the expression of the required DC voltage that balances the system. To do this, we can study the free vibration of the short cantilever under the effect of the DC voltage. By neglecting the effects of electrostatic nonlinearities, applying a DC voltage on the actuation electrode creates a continuous elastic support with a negative stiffness. The system is at the balanced state when the eigenfrequency of the short cantilever with this elastic support is equal to that of the long cantilever. Once we have the expression of the DC balancing voltage, we can choose the appropriate length of the short cantilever.

2.4.1 Free vibration of a cantilever with a continuous elastic support

We suppose that the effect of the non-ideal clamping condition on the DC balancing voltage can be neglected, so a fully clamped cantilever with a continuous elastic support is considered, as shown in Figure 2.6.

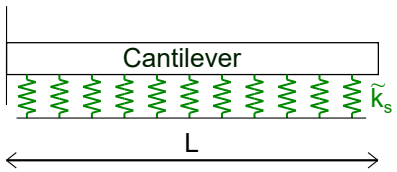

Figure 2.6: Cantilever on continuous elastic support

The equation governing the free undamped bending vibration of this system is given by

$$EI\tilde{w}'''' + \tilde{k}_s\tilde{w} + \rho bh\ddot{\tilde{w}} = 0 \tag{2.16}$$

where $\tilde{k}_s$ is the stiffness of the elastic support. By separating variables, we have

$$\tilde{w}\left(\tilde{x},\tilde{t}\right) = \phi\left(\tilde{x}\right) * \cos\left(\tilde{\omega}\tilde{t}\right) \tag{2.17}$$

where

$$\phi\left(\tilde{x}\right) = A\cos\left(\tilde{\lambda}\tilde{x}\right) + B\sin\left(\tilde{\lambda}\tilde{x}\right) + C\cosh\left(\tilde{\lambda}\tilde{x}\right) + D\sinh\left(\tilde{\lambda}\tilde{x}\right) \tag{2.18}$$

We have the same boundary conditions, so the mode shape and the value of $\tilde{\lambda}$ are the same as those of single cantilevers without continuous elastic support. As $\phi''''\left(\tilde{x}\right) = \tilde{\lambda}^4\phi\left(\tilde{x}\right)$, Equation (2.16) becomes

$$\left(EI\tilde{\lambda}^4 + \tilde{k}_s\right)\tilde{w} + \rho bh\ddot{\tilde{w}} = 0 \tag{2.19}$$

From Equation (2.19), the expression of the angular frequency $\tilde{\omega}$ is given by

$$\tilde{\omega}^2 = \frac{\left(\tilde{\lambda}L\right)^4}{L^4}\frac{EI}{\rho \mathrm{bh}} + \frac{\tilde{k}_s}{\rho bh} \tag{2.20}$$

where $\tilde{\lambda}L$ is the the weighted frequency.

2.4.2 DC balancing voltage

If we apply a DC voltage on the short cantilever, the expression of the electrostatic force per unit length is

$$\tilde{F}_E = \frac{1}{2}\varepsilon_0 b C_n \frac{{V_{DC}}^2}{(g-\tilde{w})^2} \tag{2.21}$$

where $\varepsilon_0 = 8.85\,10^{-12}\,F/m$ is the dielectric constant of the medium, C_n is the coefficient for the edge effect, and V_{DC} is the DC actuation voltage. We can expand the electrostatic force with a first order Taylor series expansion if we neglect the electrostatic nonlinearities, so

$$\tilde{F}_E = \frac{1}{2}\varepsilon_0 b C_n \frac{{V_{DC}}^2}{g^2}\left(1+2\frac{\tilde{w}}{g}\right) = \frac{1}{2}\varepsilon_0 b C_n \frac{{V_{DC}}^2}{g^2} + \varepsilon_0 b C_n \frac{{V_{DC}}^2}{g^2} * \frac{\tilde{w}}{g} \tag{2.22}$$

The first term creates the static deflection while the second term can be assimilated to a continuous elastic support. By using Equation (2.20) and setting

$$\tilde{k}_s = -\varepsilon_0 b C_n \frac{{V_{DC}}^2}{g^3} \tag{2.23}$$

the expression of the first angular frequency of the short cantilever as a function of the DC voltage is given by

$${\omega_1}^2 = \frac{\left(\tilde{\lambda}L\right)^4}{{L_1}^4}\frac{EI}{\rho b h} - \frac{\varepsilon_0 b C_n}{\rho b h}\frac{{V_{DC}}^2}{g^3} \tag{2.24}$$

For the long cantilever, its angular frequency is given by

$${\omega_2}^2 = \frac{\left(\tilde{\lambda}L\right)^4}{{L_2}^4}\frac{EI}{\rho b h} \tag{2.25}$$

The system is balanced when the two cantilevers have the same natural frequency. By equating Equation (2.24) to Equation (2.25), we obtain

$$V_{DC} = \frac{\left(\tilde{\lambda}L\right)^2}{{L_1}^2}\sqrt{\frac{EIg^3\left(1-\frac{{L_1}^4}{{L_2}^4}\right)}{\varepsilon_0 b C_n}} \tag{2.26}$$

where $\tilde{\lambda}L = 1.87$ if we consider the first mode of vibration [117]. This expression is an approximation because it does not take into account the effects of the static deflection and the electrostatic nonlinearities. As they increase the softening effects applied to the short cantilever, the actual value of the DC balancing voltage is slightly lower than that given by Equation (2.26).

2.4.3 Length of the short cantilever

To design the short cantilever, its length is chosen in order to have a DC balancing voltage around the half of the static pull-in voltage. To do so, we use Equation (2.26) to calculate the DC balancing voltage for different lengths of the short cantilever. For each length, we also calculate the pull-in voltage by using the following expression given in [25]

$$V_{PI} = \frac{1}{3}\sqrt{\frac{2Eh^3g^3}{\varepsilon_0 {L_1}^4}} \tag{2.27}$$

A length in the range $96\,\mu m$ to $100\,\mu m$ is considered, and the results are shown in Figure 2.7

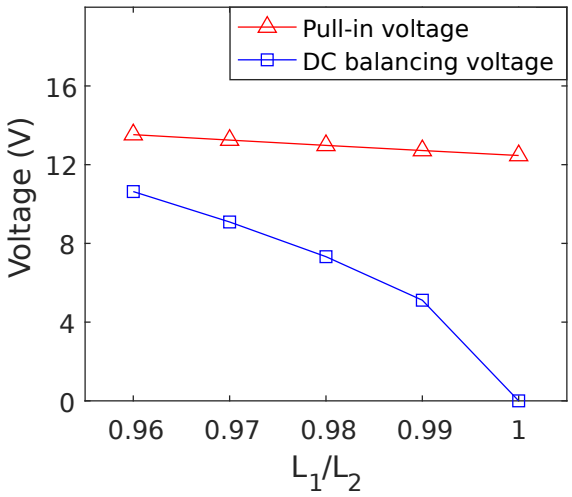

Figure 2.7: DC balancing voltage and pull-in voltage as a function of the length ratio between the two cantilevers.

We notice that the DC voltage that we have to use becomes close to the pull-in voltage when the length difference between the two cantilevers increases. By choosing a length ratio of 0.98, we get a DC balancing voltage around the half of this pull-in voltage, so the length of the short cantilever is fixed at $L_1 = 98\,\mu m$.

2.5 Modeling of the dynamic behavior of the device

After the design of the device, we present in this section the analytical model in order to study the forced vibration of the coupled cantilevers.

2.5.1 Equation governing the bending vibration of the device

We take back the model presented in section Section 2.2.1. By considering the equation of beams with intermediate spring support [109], the equation governing the bending vibration of the model in

Figure 2.2b is given by

$$\begin{cases} EI\tilde{w}_1'''' + (\rho bh + \tilde{m}\delta(\tilde{x}-\tilde{x}_m))\ddot{\tilde{w}}_1 + \tilde{c}_1\dot{\tilde{w}}_1 - \tilde{k}_r\left(\tilde{w}_1'(\tilde{x}_c) - \tilde{w}_2'(\tilde{x}_c)\right)\delta'(\tilde{x}-\tilde{x}_c) \\ \qquad = \frac{1}{2}\varepsilon_0 bC_n\frac{\left(V_{DC}+v_{AC}\cos\left(\tilde{\Omega}\tilde{t}\right)\right)^2}{(g-\tilde{w}_1)^2} \\ EI\tilde{w}_2'''' + \rho bh\ddot{\tilde{w}}_2 + \tilde{c}_2\dot{\tilde{w}}_2 - \tilde{k}_r\left(\tilde{w}_2'(\tilde{x}_c) - \tilde{w}_1'(\tilde{x}_c)\right)\delta'(\tilde{x}-\tilde{x}_c) = 0 \end{cases} \tag{2.28}$$

where $\tilde{w}_1$ and $\tilde{w}_2$ are respectively the deflections of the short and the long cantilevers, $\tilde{c}_1$ and $\tilde{c}_2$ are their damping coefficient, δ is the Dirac delta function, $\tilde{m}$ is the mass perturbation, v_{AC} is the AC actuation voltage, and $\tilde{\Omega}$ is the excitation frequency. The damping coefficient of each cantilever can be expressed by

$$\tilde{c} = \frac{\rho bh 2\pi f}{Q} \tag{2.29}$$

where f is the resonance frequency of the cantilever and Q is the quality factor.
For convenience, we introduce the non dimensional variables and parameters below

$$\begin{gathered} x = \frac{\tilde{x}}{L_1}\ ;\ x_c = \frac{\tilde{x}_c}{L_1}\ ;\ x_m = \frac{\tilde{x}_m}{L_1}\ ;\ m = \frac{\tilde{m}}{\rho bhL_1}\ ;\ w = \frac{\tilde{w}}{g}\ ;\ \tau = {L_1}^2\sqrt{\frac{\rho bh}{EI}}\ ;\ t = \frac{\tilde{t}}{\tau}\ ; \\ \Omega = \tilde{\Omega}\tau\ ;\ c = \frac{{L_1}^4\tilde{c}}{EI\tau}\ ;\ k_r = \frac{\tilde{k}_r L_1}{EI}\ ;\ \delta_0 = \frac{1}{2}\varepsilon_0 b\frac{{L_1}^4}{g^3 EI} \end{gathered} \tag{2.30}$$

The nonlinear terms of the electrostatic force can be approximated by using a Taylor series expansion [26, 118, 119], or by multiplying the equation with the denominator $(1-\tilde{w}_1)^2$ [119, 120]. For our case, the first method is used, and we expand the electrostatic force in a third order Taylor series. After these considerations, Equation (2.28) becomes

$$\begin{cases} w_1'''' + (1 + m\delta(x-x_m))\ddot{w}_1 + c_1\dot{w}_1 - k_r\left(w_1'(x_c) - w_2'(x_c)\right)\delta'(x-x_c) \\ \qquad = \delta_0(V_{DC}+v_{AC}\cos(\Omega t))^2 * \left(1 + 2{w_1} + 3{w_1}^2 + 4{w_1}^3\right) \\ w_2'''' + \ddot{w}_2 + c_2\dot{w}_2 - k_r\left(w_2'(x_c) - w_1'(x_c)\right)\delta'(x-x_c) = 0 \end{cases} \tag{2.31}$$

where primes and dots denote respectively the partial differentiation with respect to the new nondimensional variables x and t.

2.5.2 Static deflection

When the electrostatic actuation is composed of DC and AC voltages, the microbeam is bent by the DC component, and driven to vibrate by the AC component [121]. So the equilibrium position of the microbeam is shifted and it vibrates around a static deflection which depends on the DC voltage. To calculate this static deflection, we only consider the DC voltage in the actuation. After dropping all

time varying terms in Equation (2.31) [122], we obtain the following equation

$$\begin{cases} w_{1s}'''' - k_r \left(w_{1s}'(x_c) - w_{2s}'(x_c)\right) \delta'(x - x_c) = \delta_0 {V_{DC}}^2 \left(1 + 2w_{1s} + 3{w_{1s}}^2 + 4{w_{1s}}^3\right) \\ w_{2s}'''' - k_r \left(w_{2s}'(x_c) - w_{1s}'(x_c)\right) \delta'(x - x_c) = 0 \end{cases} \tag{2.32}$$

where w_{1s} and w_{2s} are respectively the normalized static deflection of the short and the long cantilevers.

Discretization of the equation

To solve Equation (2.32), we use Galerkin discretization approach and consider only one mode. As the coupling is weak, we assume that the mode shape of each cantilever is the same as the mode shape of a single cantilever with the flexible support (Appendix A.4). So the normalized static deflection of the microbeams can be approximated by

$$w_{1s}(x) = a_{1s}\phi_1(x) \quad \text{and} \quad w_{2s}(x) = a_{2s}\phi_2(x) \tag{2.33}$$

where $\phi_1(x)$ and $\phi_2(x)$ are respectively the mode shapes of the short and the long cantilevers, and a_{1s} and a_{2s} are the generalized coordinates of the static deflection.
The expressions of the mode shape are

$$\phi_i(x) = K_{i1}\left[K_{i2}\sin\left(\lambda_i x\frac{L_1}{L_i}\right) - K_{i3}\sinh\left(\lambda_i x\frac{L_1}{L_i}\right) + \frac{\sin\lambda_i + \sinh\lambda_i}{\cos\lambda_i + \cosh\lambda_i}\left(\cosh\left(\lambda_i x\frac{L_1}{L_i}\right) - \cos\left(\lambda_i x\frac{L_1}{L_i}\right)\right)\right] \tag{2.34}$$

where K_{i1} are chosen in order to have

$$\int_0^{\frac{L_i}{L_1}} {\phi_i}^2(x)\,dx = 1\,; \tag{2.35}$$

K_{i2} and K_{i3} are expressed as

$$K_{i2} = \frac{\cos\lambda_i + \cosh\lambda_i + \frac{2EI\lambda_i}{\tilde{k}_e L_i}\sinh\lambda_i}{\cos\lambda_i + \cosh\lambda_i}\,; K_{i3} = \frac{\cos\lambda_i + \cosh\lambda_i - \frac{2EI\lambda_i}{\tilde{k}_e L_i}\sin\lambda_i}{\cos\lambda_i + \cosh\lambda_i}\,; \tag{2.36}$$

and λ_i is the first solution of the following equation

$$\frac{\tilde{k}_e L_i}{EI\lambda_i}(\cos\lambda_i\cosh\lambda_i + 1) + \cos\lambda_i\sinh\lambda_i - \sin\lambda_i\cosh\lambda_i = 0 \tag{2.37}$$

By replacing the expressions of $w_{1s}(x)$ and $w_{2s}(x)$ and by taking into account the following relationships

$$\phi_1''''(x) = {\lambda_1}^4\phi_1(x) \quad \text{and} \quad \phi_2''''(x) = {\lambda_2}^4\frac{L_1^4}{L_2^4}\phi_2(x)\ , \tag{2.38}$$

Equation (2.32) becomes

$$\begin{cases} {a_{1s}}{\lambda_1}^4\phi_1(x) - k_r\left(a_{1s}\phi_1'(x_c) - a_{2s}\phi_2'(x_c)\right)\delta'(x-x_c) = \delta_0 {V_{DC}}^2\left(1+2a_{1s}\phi_1(x)\right. \\ \qquad\qquad \left. +3{a_{1s}}^2\phi_1^2(x) + 4{a_{1s}}^3\phi_1^3(x)\right) \\ {a_{2s}}{\lambda_2}^4\dfrac{{L_1}^4}{{L_2}^4}\phi_2(x) - k_r\left(a_{2s}\phi_2'(x_c) - a_{1s}\phi_1'(x_c)\right)\delta'(x-x_c) = 0 \end{cases} \tag{2.39}$$

Then, we multiply respectively the first and the second equations of Equation (2.39) by $\phi_1(x)$ and $\phi_2(x)$, and integrate them respectively from $x=0$ to $x=1$ and from $x=0$ to $x=L_2/L_1$. When the value of the torsional stiffness $\tilde{k}_e$ at the fixed end is sufficiently high to ensure a good clamping condition, we obtain the following parameters which remain almost unchanged

$$\int_0^1 \phi_1(x)\,dx \approx 0.784\,;\; 3\int_0^1 {\phi_1}^3(x)\,dx \approx 4.43\,;\; 4\int_0^1 {\phi_1}^4(x)\,dx \approx 9.39 \tag{2.40}$$

After this consideration and by taking into account the following properties of the Dirac delta function

$$\int_0^{\frac{L_i}{L_1}} \delta'(x-x_c)\,\phi_i(x)\,dx = -{\phi_i}'(x_c) \tag{2.41}$$

Equation (2.39) becomes

$$\begin{cases} {a_{1s}}{\lambda_1}^4\phi_1(x) + k_r\left(a_{1s}\phi_1'^2(x_c) - a_{2s}\phi_1'(x_c)\,\phi_2'(x_c)\right) = \delta_0 {V_{DC}}^2\left(0.784 + 2\,a_{1s} + 4.43\,{a_{1s}}^2 + 9.39\,{a_{1s}}^3\right) \\ {a_{2s}}{\lambda_2}^4\dfrac{{L_1}^4}{{L_2}^4} + k_r\left(a_{2s}\phi_2'^2(x_c) - a_{1s}\phi_1'(x_c)\,\phi_2'(x_c)\right) = 0 \end{cases} \tag{2.42}$$

Resolution of the equation

By substituting a_{2s} in the first equation of Equation (2.42), we obtain

$$\begin{cases} 9.39\,\delta_0 {V_{DC}}^2\,{a_{1s}}^3 + 4.43\,\delta_0 {V_{DC}}^2\,{a_{1s}}^2 \\ + \left[2\,\delta_0 {V_{DC}}^2 - {\lambda_1}^4 - k_r\left(\phi_1'^2(x_c) - \dfrac{k_r\phi_1'^2(x_c)\,{\phi_2'}^2(x_c)}{{\lambda_2}^4\frac{{L_1}^4}{{L_2}^4} + k_r{\phi_2'}^2(x_c)}\right)\right]a_{1s} + 0.784\delta_0 {V_{DC}}^2 = 0 \\ a_{2s} = \dfrac{k_r\phi_1'(x_c)\,\phi_2'(x_c)}{{\lambda_2}^4\frac{{L_1}^4}{{L_2}^4} + k_r{\phi_2}'^2(x_c)}\,a_{1s} \end{cases} \tag{2.43}$$

The first equation of Equation (2.43) is a cubic equation which can be solved with MATLAB® R2019. After calculating a_{1s}, we can deduce a_{2s} from the second equation of Equation (2.43). Finally, the static deflection at the end of each cantilevers is given by

$$W_{1s} = a_{1s} * \phi_1(1) * g \quad \text{and} \quad W_{2s} = a_{2s} * \phi_2\left(\frac{L_2}{L_1}\right) * g \tag{2.44}$$

2.5.3 Dynamic deflection

Discretization of the equation

After determining the static deflection, we use again the Galerkin discretization with one mode, and we suppose that the normalized total deflection of the cantilevers can be expressed by

$$w_1(x,t) = (a_{1s} + a_1(t)) * \phi_1(x) \quad \text{and} \quad w_2(x,t) = (a_{2s} + a_2(t)) * \phi_2(x) \tag{2.45}$$

So, Equation (2.31) becomes

$$\begin{cases} (a_{1s} + a_1(t))\,{\lambda_1}^4 \phi_1(x) + (1 + m\delta(x - x_m))\,\ddot{a}_1(t)\,\phi_1(x) + c_1\dot{a}_1(t)\,\phi_1(x) - k_r\left((a_{1s} + a_1(t))\,\phi_1'(x_c)\right. \\ \left. - (a_{2s} + a_2(t))\,\phi_2'(x_c)\right)\delta'(x - x_c) = \delta_0(V_{DC} + v_{AC}\cos(\Omega t))^2 \\ * \left(1 + 2(a_{1s} + a_1(t))\,\phi_1(x) + 3(a_{1s} + a_1(t))^2\phi_1^2(x) + 4(a_{1s} + a_1(t))^3\phi_1^3(x)\right) \\ \\ (a_{2s} + a_2(t))\,{\lambda_2}^4 \dfrac{{L_1}^4}{{L_2}^4}\phi_2(x) + \ddot{a}_2(t)\,\phi_2(x) + c_2\dot{a}_2(t)\,\phi_2(x) \\ -k_r\left((a_{2s} + a_2(t))\,\phi_2'(x_c) - (a_{1s} + a_1(t))\,\phi_1'(x_c)\right)\delta'(x - x_c) = 0 \end{cases} \tag{2.46}$$

Like for the static deflection, we multiply respectively the first and the second equations in Equation (2.46) by $\phi_1(x)$ and $\phi_2(x)$, and integrate them respectively from $x = 0$ to $x = 1$ and from $x = 0$ to $x = L_2/L_1$. In the resulting equation, we can eliminate some terms which concern the static deflection by using relationships in Equation (2.42). As the AC voltage is very low compared to the DC voltage, we can also drop all terms with ${v_{AC}}^2$. After this consideration, we obtain

$$\begin{cases} \left(1 + m{\phi_1}^2(x_m)\right)\ddot{a}_1 + c_1\dot{a}_1 + \left({\lambda_1}^4 - \delta_0{V_{DC}}^2\left(2 + 8.86\,a_{1s} + 28.2\,{a_{1s}}^2\right)\right)a_1 \\ +k_r\left(a_1\phi_1'^2(x_c) - a_2\phi_1'(x_c)\,\phi_2'(x_c)\right) = F_1\cos(\Omega t) + F_2\cos(\Omega t) * a_1 \\ +F_3\cos(\Omega t) * {a_1}^2 + F_4\cos(\Omega t) * {a_1}^3 + F_5 * {a_1}^2 + F_6 * {a_1}^3 \\ \\ \ddot{a}_2 + c_2\dot{a}_2 + {\lambda_2}^4\dfrac{{L_1}^4}{{L_2}^4}a_2 + k_r\left(a_2\phi_2'^2(x_c) - a_1\phi_1'(x_c)\,\phi_2'(x_c)\right) = 0 \end{cases} \tag{2.47}$$

where

$$\begin{aligned} F_1 &= \left(1.56 + 4\,a_{1s} + 8.86\,{a_{1s}}^2 + 18.8\,{a_{1s}}^3\right)\delta_0 V_{DC} v_{AC} \\ F_2 &= \left(4 + 17.7\,a_{1s} + 56.3\,{a_{1s}}^2\right)\delta_0 V_{DC} v_{AC} \\ F_3 &= (8.86 + 56.3\,a_{1s})\,\delta_0 V_{DC} v_{AC} \\ F_4 &= 18.8\,\delta_0 V_{DC} v_{AC} \\ F_5 &= (4.43 + 28.2\,a_{1s})\,\delta_0 {V_{DC}}^2 \\ F_6 &= 9.39\,\delta_0 {V_{DC}}^2 \end{aligned} \tag{2.48}$$

By keeping only the harmonic load $F_1 \cos(\Omega t)$, the quadratic nonlinearity $F_5 * {a_1}^2$ and the cubic nonlinearity $F_6 * {a_1}^3$, and after moving some terms to the right side, Equation (2.47) becomes

$$\begin{cases} \left(1 + m{\phi_1}^2(x_m)\right)\ddot{a}_1 + \left({\lambda_1}^4 - \delta_0 {V_{DC}}^2\left(2 + 8.86\,a_{1s} + 28.2\,{a_{1s}}^2\right)\right)a_1 \\ \quad = -c_1\dot{a}_1 + (4.43 + 28.2\,a_{1s})\,\delta_0 {V_{DC}}^2\,{a_1}^2 + 9.39\,\delta_0 {V_{DC}}^2\,{a_1}^3 \\ + \left(1.56 + 4\,a_{1s} + 8.86\,{a_{1s}}^2 + 18.8\,{a_{1s}}^3\right)\delta_0 V_{DC} v_{AC}\cos(\Omega t) - k_r\left(a_1\phi_1'^2(x_c) - a_2\phi_1'(x_c)\,\phi_2'(x_c)\right) \\ \\ \ddot{a}_2 + {\lambda_2}^4\dfrac{{L_1}^4}{{L_2}^4}a_2 = -c_2\dot{a}_2 - k_r\left(a_2\phi_2'^2(x_c) - a_1\phi_1'(x_c)\,\phi_2'(x_c)\right) \end{cases} \tag{2.49}$$

This equation describes a linear oscillator coupled to a nonlinear oscillator with quadratic and cubic nonlinearities.

Resolution of the equation with the method of multiple scales

In this part, we use the method of multiple scales [123] to solve the equation governing the forced vibration of the coupled cantilever. We choose this method because it is commonly used for nonlinear systems [124, 125], and it can find a good approximate solution. The principle of this method consists in introducing different scales of times T_n depending on a parameter ε, and defined by

$$T_n = \varepsilon^n t \quad \text{where} \quad \varepsilon \ll 1 \tag{2.50}$$

Hence, the partial differentiation with respect to the time t becomes

$$\begin{aligned} \frac{d}{dt} &= \frac{dT_0}{dt}\frac{\partial}{\partial T_0} + \frac{dT_1}{dt}\frac{\partial}{\partial T_1} + \frac{dT_2}{dt}\frac{\partial}{\partial T_2} + \ldots = D_0 + \varepsilon D_1 + \varepsilon^2 D_2 + \ldots \\ \frac{d^2}{\mathrm{dt}^2} &= {D_0}^2 + 2\varepsilon D_0 D_1 + \varepsilon^2\left({D_1}^2 + 2D_0 D_2\right) + \ldots \end{aligned} \tag{2.51}$$

As the damping, the quadratic and cubic nonlinearities, the harmonic load and the coupling are very weak, we can express them as a function of ε or ε^2. Equation (2.49) can be we rewritten as follows

$$\begin{cases} \ddot{a}_1 + {\omega_1}^2 a_1 = -2\varepsilon^2\mu_1\,\dot{a}_1 - \varepsilon\alpha_2\,{a_1}^2 - \varepsilon^2\alpha_3\,{a_1}^3 + \varepsilon^2 f_1\cos(\Omega t) - \varepsilon^2 k\left(\gamma_1\,a_1 - \gamma_2\,a_2\right) \\ \ddot{a}_2 + {\omega_2}^2 a_2 = -2\varepsilon^2\mu_2\,\dot{a}_2 - \varepsilon^2 k\left(\gamma_3\,a_2 - \gamma_4\,a_1\right) \end{cases} \tag{2.52}$$

where

$$
\begin{aligned}
{\omega_1}^2 &= \frac{{\lambda_1}^4 - \delta_0 {V_{DC}}^2 \left(2 + 8.86\, a_{1s} + 28.17\, {a_{1s}}^2\right)}{1 + m{\phi_1}^2 (x_m)} \\
2\varepsilon^2 \mu_1 &= \frac{c_1}{1 + m{\phi_1}^2 (x_m)} \\
-\varepsilon \alpha_2 &= \frac{(4.43 + 28.17\, a_{1s})\, \delta_0 {V_{DC}}^2}{1 + m{\phi_1}^2 (x_m)} \\
-\varepsilon^2 \alpha_3 &= \frac{9.39\, \delta_0 {V_{DC}}^2}{1 + m{\phi_1}^2 (x_m)} \\
\varepsilon^2 f_1 &= \frac{\left(1.56 + 4\, a_{1s} + 8.86\, {a_{1s}}^2 + 18.8\, {a_{1s}}^3\right) \delta_0 V_{DC} v_{AC}}{1 + m{\phi_1}^2 (x_m)} \\
\varepsilon^2 k &= k_r \\
\gamma_1 &= \frac{{\phi_1}^2 (x_c)}{1 + m{\phi_1}^2 (x_m)} \\
\gamma_2 &= \frac{\phi_1' (x_c)\, \phi_2' (x_c)}{1 + m{\phi_1}^2 (x_m)} \\
{\omega_2}^2 &= {\lambda_2}^4 \frac{{L_1}^4}{{L_2}^4} \\
2\varepsilon^2 \mu_2 &= c_2 \\
\gamma_3 &= {\phi_2}^2 (x_c) \\
\gamma_4 &= \phi_1' (x_c)\, \phi_2' (x_c)
\end{aligned}
\tag{2.53}
$$

As the frequency Ω of the harmonic load and the frequencies ω_1 and ω_2 of the two oscillators are very close, we can also set the folling relationships

$$
\begin{aligned}
\Omega &= \omega_1 + \varepsilon^2 \sigma_1 \\
\Omega t &= \omega_1 T_0 + \sigma_1 T_2 \\
\omega_1 &= \omega_2 + \varepsilon^2 \sigma_2 \\
\omega_1 T_0 &= \omega_2 T_0 + \sigma_2 T_2
\end{aligned}
\tag{2.54}
$$

where σ_1 is a detuning parameter and

$$
\sigma_2 = \frac{\omega_1 - \omega_2}{\varepsilon^2} \tag{2.55}
$$

We assume now that the solution of Equation (2.49) can be expressed by a second order expansion having the form

$$
\begin{aligned}
a_1 &= a_{10}(T_0, T_1, T_2) + \varepsilon a_{11}(T_0, T_1, T_2) + \varepsilon^2 a_{12}(T_0, T_1, T_2) \\
a_2 &= a_{20}(T_0, T_1, T_2) + \varepsilon a_{21}(T_0, T_1, T_2) + \varepsilon^2 a_{22}(T_0, T_1, T_2)
\end{aligned}
\tag{2.56}
$$

By substituting a_1 in the first equation of Equation (2.52) and using the derivative formulas in Equation (2.51), we obtain terms which depend on ε^0, ε^1 and ε^2, and the other terms with higher order are

neglected. By equating these terms to zero, we obtain

$$\text{terms with } \varepsilon^0 : {D_0}^2 a_{10} + {\omega_1}^2 a_{10} = 0 \tag{2.57a}$$

$$\text{terms with } \varepsilon^1 : {\omega_1}^2 a_{11} + D_0 \left(D_0 a_{11} + D_1 a_{10}\right) + D_1 D_0 a_{10} = -\alpha_2 {a_{10}}^2 \tag{2.57b}$$

$$\begin{aligned}\text{terms with } \varepsilon^2 : & D_0 \left(D_0 a_{12} + D_1 a_{11} + D_2 a_{10}\right) + D_1 \left(D_0 a_{11} + D_1 a_{10}\right) + D_2 D_0 a_{10} \\ & + {\omega_1}^2 a_{12} = -2\mu_1 D_0 a_{10} - k\left(\gamma_1 a_{10} - \gamma_2 a_{20}\right) - \alpha_3 {a_{10}}^3 \\ & - 2\alpha_2 a_{10} a_{11} + f_1 . \cos\left(\omega_1 T_0 + \sigma_1 T_2\right)\end{aligned} \tag{2.57c}$$

Equation (2.57a) describes the equation of a simple harmonic oscillator, so its solution is given by

$$a_{10} = A_1\left(T_1, T_2\right) \exp\left(i\omega_1 T_0\right) + \overline{A_1}\left(T_1, T_2\right) \exp\left(-i\omega_1 T_0\right) \tag{2.58}$$

where A_1 is a complex function and $\overline{A_1}$ is its complex conjugate.
Substituting a_{10} in Equation (2.57b) gives us

$${D_0}^2 a_{11} + {\omega_1}^2 a_{11} = -2i\omega_1 D_1 A_1 \exp\left(i\omega_1 T_0\right) - \alpha_2 \left({A_1}^2 \exp\left(2i\omega_1 T_0\right) + A_1 \overline{A_1}\right) + cc \tag{2.59}$$

where cc is the complex conjugate of the term in the right side. Eliminating the term in Equation (2.59) that produces secular terms in a_{11} leads to

$$D_1 A_1 = 0 \quad \text{or} \quad A_1 = A_1\left(T_2\right) \tag{2.60}$$

The solution of Equation (2.59) becomes

$$a_{11} = \frac{\alpha_2}{{\omega_1}^2}\left(-A_1 \overline{A_1} + \frac{1}{3}{A_1}^2 \exp\left(2i\omega_1 T_0\right)\right) + cc \tag{2.61}$$

By substituting a_{10} and a_{11} in Equation (2.57c), we obtain

$$\begin{aligned}{D_0}^2 a_{12} + {\omega_1}^2 a_{12} = \Big(&-2i\omega_1\left(A_1' + \mu_1 A_1\right) - k\gamma_1 A_1 + k\gamma_2 A_2 \exp\left(-i\sigma_2 T_2\right) - \alpha_3 3 {A_1}^2 \overline{A_1} \\ &+ \frac{10}{3}\frac{{\alpha_2}^2}{{\omega_1}^2}{A_1}^2 \overline{A_1} + \frac{1}{2} f_1 \exp\left(i\sigma_1 T_2\right)\Big) \exp\left(i\omega_1 T_0\right) + cc + NST\end{aligned} \tag{2.62}$$

where NST (non-secular terms) are terms which are proportional to $\exp\left(\pm 3i\omega_1 T_0\right)$.
Let's consider now the second equation of Equation (2.52). By substituting the expression of a_2 in Equation (2.56) in this equation, we also obtain terms which depend on ε^0, ε^1 and ε^2, and equating

them to zero gives us

$$\text{terms with } \varepsilon^0 : {D_0}^2 a_{20} + {\omega_2}^2 a_{20} = 0 \tag{2.63a}$$

$$\text{terms with } \varepsilon^1 : {\omega_2}^2 a_{21} + D_0 \left(D_0 a_{21} + D_1 a_{20}\right) + D_1 D_0 a_{20} = 0 \tag{2.63b}$$

$$\begin{aligned}\text{terms with } \varepsilon^2 : & D_0 \left(D_0 a_{22} + D_1 a_{21} + D_2 a_{20}\right) + D_1 \left(D_0 a_{21} + D_1 a_{20}\right) + D_2 D_0 a_{20} \\ & + {\omega_2}^2 a_{22} = -2\mu_2 D_0 a_{20} - k\left(\gamma_3 a_{20} - \gamma_4 a_{10}\right)\end{aligned} \tag{2.63c}$$

By using the same approach, we obtain

$${D_0}^2 a_{22} + {\omega_2}^2 a_{22} = \left(-2i\omega_2 \left(A_2' + \mu_2 A_2\right) - k\gamma_3 A_2 + k\gamma_4 A_1 \exp\left(i\sigma_2 T_2\right)\right) \exp\left(i\omega_2 T_0\right) + cc + NST \tag{2.64}$$

By eliminating all terms in Equation (2.62) and Equation (2.64) that produce respectively secular terms in a_{12} and a_{22}, we finally obtain

$$\begin{cases} -2i\omega_1 \left(A_1' + \mu_1 A_1\right) - k\gamma_1 A_1 + k\gamma_2 A_2 \exp\left(-i\sigma_2 T_2\right) - \alpha_3 3 {A_1}^2 \overline{A_1} + \dfrac{10}{3} \dfrac{{\alpha_2}^2}{{\omega_1}^2} {A_1}^2 \overline{A_1} \\ \qquad + \dfrac{1}{2} f_1 \exp\left(i\sigma_1 T_2\right) = 0 \\ \\ -2i\omega_2 \left(A_2' + \mu_2 A_2\right) - k\gamma_3 A_2 + k\gamma_4 A_1 \exp\left(i\sigma_2 T_2\right) = 0 \end{cases} \tag{2.65}$$

We let now

$$\begin{aligned} A_1 &= u_1 \exp\left(i\theta_1\right) \\ A_1' &= u_1' \exp\left(i\theta_1\right) + u_1 i\theta_1' \exp\left(i\theta_1\right) \\ A_2 &= u_2 \exp\left(i\theta_2\right) \\ A_2' &= u_2' \exp\left(i\theta_2\right) + u_2 i\theta_2' \exp\left(i\theta_2\right) \\ \beta_1 &= \sigma_1 T_2 - \theta_1 \\ \beta_2 &= -\theta_1 - \sigma_2 T_2 + \theta_2 \end{aligned} \tag{2.66}$$

After multiplying respectively the first and the second equations of Equation (2.65) by $\exp\left(-i\theta_1\right)$ and $\exp\left(-i\theta_2\right)$, and equating real and imaginary parts to zero, we obtain the four following relationships

$$2\omega_1 u_1 \theta_1' + \left(\frac{10}{3} \frac{{\alpha_2}^2}{{\omega_1}^2} - 3\alpha_3\right) {u_1}^3 + \frac{1}{2} f_1 . \cos\beta_1 - k\gamma_1 u_1 + k\gamma_2 u_2 \cos\beta_2 = 0 \tag{2.67a}$$

$$-2\omega_1 \mu_1 u_1 - 2\omega_1 u_1' + \frac{1}{2} f_1 . \sin\beta_1 + k\gamma_2 u_2 \sin\beta_2 = 0 \tag{2.67b}$$

$$2\omega_2 u_2 \theta_2' - k\gamma_3 u_2 + k\gamma_4 u_1 \cos\beta_2 = 0 \tag{2.67c}$$

$$-2\omega_2 \mu_2 u_2 - 2\omega_2 u_2' - k\gamma_4 u_1 \sin\beta_2 = 0 \tag{2.67d}$$

At steady state motion, we have

$$u_1' = 0 \;\; ; \;\; \beta_1' = 0 \;\; ; \;\; u_2' = 0 \;\; ; \;\; \beta_2' = 0 \tag{2.68}$$

and

$$\theta_1' = \sigma_1 \;\; ; \;\; \theta_2' = \sigma_1 + \sigma_2 \tag{2.69}$$

Equation (2.67) becomes

$$\frac{1}{2} f_1 \cos\beta_1 = -\left(\frac{10}{3}\frac{{\alpha_2}^2}{{\omega_1}^2} - 3\alpha_3\right) {u_1}^3 + \left(-2\omega_1\sigma_1 + k\gamma_1\right) u_1 - k\gamma_2 u_2 \cos\beta_2 \tag{2.70a}$$

$$\frac{1}{2} f_1 \sin\beta_1 = 2\omega_1\mu_1 u_1 - k\gamma_2 u_2 \sin\beta_2 \tag{2.70b}$$

$$\cos\beta_2 = \frac{-2\omega_2\left(\sigma_1+\sigma_2\right) + k\gamma_3}{k\gamma_4} * \frac{u_2}{u_1} \tag{2.70c}$$

$$\sin\beta_2 = -\frac{2\omega_2\mu_2}{k\gamma_4} * \frac{u_2}{u_1} \tag{2.70d}$$

From Equation (2.70c) and Equation (2.70d), we obtain

$$u_2 = \frac{k\gamma_4}{\sqrt{\left[-2\omega_2\left(\sigma_1+\sigma_2\right) + k\gamma_3\right]^2 + \left(2\omega_2\mu_2\right)^2}} u_1 \tag{2.71}$$

From Equation (2.70a) and Equation (2.70b), and substituting u_2, we obtain

$$\begin{aligned}\left[\left(3\alpha_3 - \frac{10}{3}\frac{{\alpha_2}^2}{{\omega_1}^2}\right) {u_1}^3 + \left(\left(-2\omega_1\sigma_1 + k\gamma_1\right) - k\gamma_2 \frac{\left[-2\omega_2\left(\sigma_1+\sigma_2\right) + k\gamma_3\right] k\gamma_4}{\left[-2\omega_2\left(\sigma_1+\sigma_2\right) + k\gamma_3\right]^2 + \left(2\omega_2\mu_2\right)^2}\right) u_1\right]^2 \\ + \left[\left(2\omega_1\mu_1 + k\gamma_2 \frac{2\omega_2\mu_2 k\gamma_4}{\left[-2\omega_2\left(\sigma_1+\sigma_2\right) + k\gamma_3\right]^2 + \left(2\omega_2\mu_2\right)^2}\right) u_1\right]^2 - \frac{1}{4}{f_1}^2 = 0\end{aligned} \tag{2.72}$$

Expanding Equation (2.72) leads to a sixth order equation, and by proceeding to a variable change ${U_1} = {u_1}^2$, we can reduce it to a cubic equation. By choosing a value of σ_1 and fixing $\varepsilon = 0.01$, we can solve the resulting equation and get the value of u_1, while u_2 is deduced from Equation (2.71). Finally, the frequency and the vibration amplitude at the end of each cantilever is given by

$$\begin{aligned} f &= \frac{\omega_1 + \varepsilon^2\sigma_1}{2\pi\tau} \\ W_1 &= 2u_1 * \phi_1\left(1\right) * g \\ W_2 &= 2u_2 * \phi_2\left(\frac{L_2}{L_1}\right) * g \end{aligned} \tag{2.73}$$

To plot the frequency response, the excitation frequency f is varied by changing σ_1 in Equation (2.73), and we calculate the vibration amplitudes W_1 and W_2 for each value of f. As the cubic equation derived from Equation (2.72) can lead to three real solutions, we can have a multivalued amplitude in the frequency response.

2.5.4 Amplitude responses at the balanced state

We plot the amplitude responses of the device by using the analytical model. We choose a coupling beam with a length $L_c = 65\,\mu m$, and located at $\tilde{x}_c = 10.5\,\mu m$. For the quality factor, we set $Q = 500$. For the DC balancing voltage, we can start the simulation by using the value given by Equation (2.26) in Section 2.4.2, but we will have to make some adjustments after because it does not take into account the effects of the static deflection and the electrostatic nonlinearities. The system is at the balanced state when it exhibits the symmetric and antisymmetric modes with an amplitude response similar to the one shown in Figure 1.16d (Section 1.4.2).

Frequency response with low vibration amplitudes

To consider the linear case where the effects of electrostatic nonlinearities are negligible, we use a small AC actuation voltage in order to have low vibration amplitudes. With $v_{AC} = 5\,mV$, the results are shown in Figure 2.8.

We notice that with a DC voltage below the DC balancing voltage (Figure 2.8a), the short cantilever still has a higher effective stiffness than the long cantilever. The vibrations are localized on the long cantilever for the first mode, and on the short cantilever for the second mode. At the balanced state (Figure 2.8b) we have identical amplitudes on both cantilevers, either for the first or for the second mode. With a DC voltage above the DC balancing voltage (Figure 2.8c), the effective stiffness of the short cantilever becomes lower than that of the long cantilever. The vibrations are localized on the short cantilever for the first mode, and on the long cantilever for the second mode. For each case where the DC voltage is below or above the DC balancing voltage, the vibrations can then be localized either on the short cantilever or on the long cantilever, depending on the considered mode. But this localization is more marked when it is the short cantilever that vibrates the most. It is due to the fact that it is difficult to have a vibration localized on the cantilever which is not actuated.

Concerning the frequencies of the two modes, we notice by comparing Figures 2.8a to 2.8c that both decrease as the applied DC voltage increases. Normally, only the frequency of the second mode decreases before the veering point. After the veering point, it remains unchanged and only the frequency of the first mode decreases. But this appears only when the coupling ratio is very weak. As we choose $\tilde{x}_c = 10.5\,\mu m$ for the simulation, the coupling ratio is more important. We can also do this observation if we look at the loci veering in Figure 1.12.

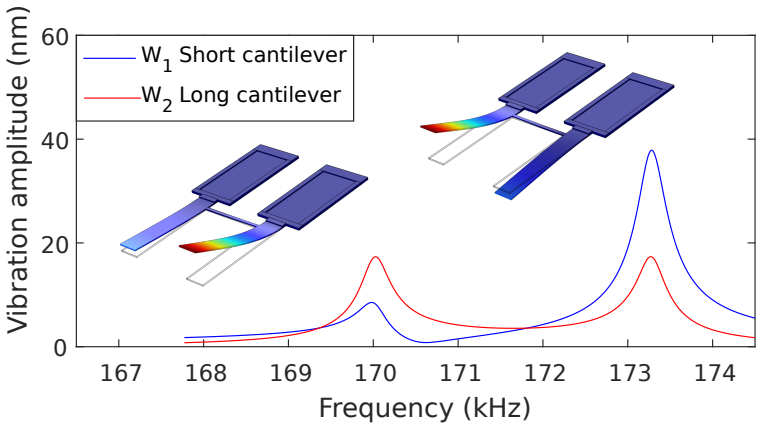

(a) DC voltage below the DC balancing voltage ($v_{AC} = 5\,mV$ and $V_{DC} = 5.64\,V$)

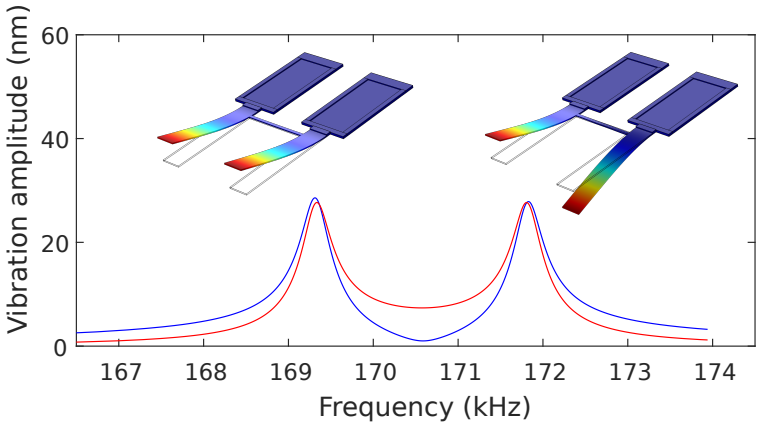

(b) Balanced state ($v_{AC} = 5\,mV$ and $V_{DC} = 6.64\,V$)

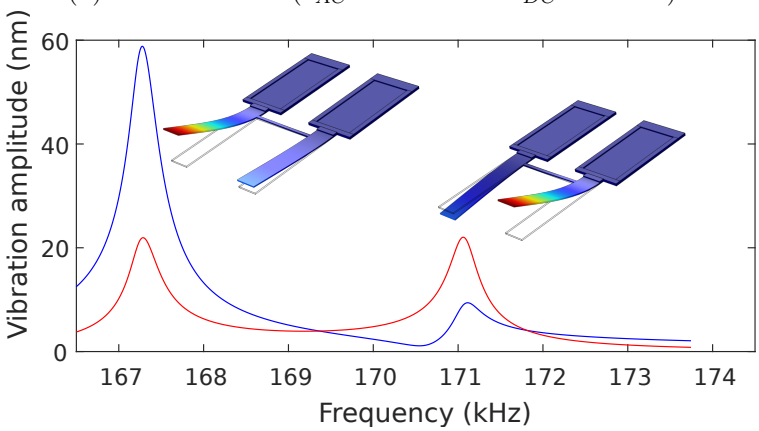

(c) DC voltage above the DC balancing voltage ($v_{AC} = 5\,mV$ and $V_{DC} = 7.64\,V$)

Figure 2.8: Frequency responses of the device with low vibration amplitudes

Frequency response with high vibration amplitudes

To consider the nonlinear case involving high vibration amplitudes, we use a higher AC actuation voltage. With $v_{AC} = 75\,mV$, the results are shown in Figure 2.9.

We notice that like in the linear case, the vibrations are localized in one of the two cantilevers when a DC voltage different from the DC balancing voltage is applied. At the balance state (Figure 2.9b), we also have identical amplitudes on both cantilevers. But compared to the linear case, a lower DC

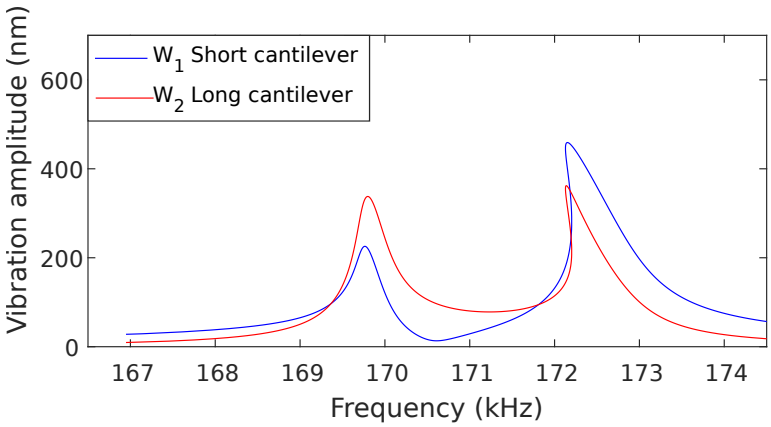

(a) DC voltage below the DC balancing voltage ($v_{AC} = 75\,mV$ and $V_{DC} = 6.05\,V$)

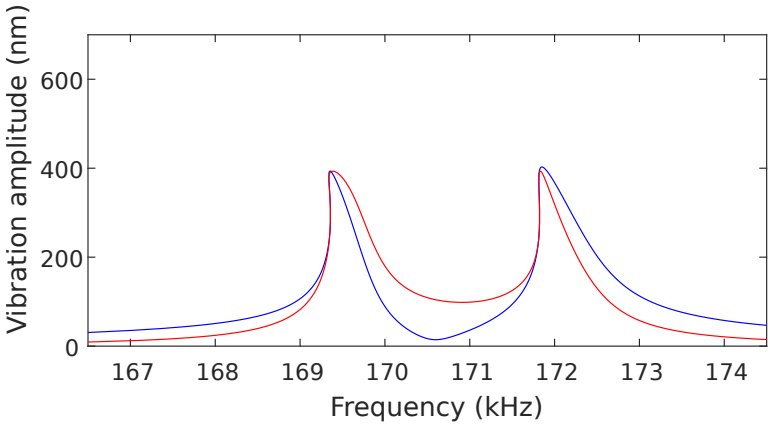

(b) Balanced state ($v_{AC} = 75\,mV$ and $V_{DC} = 6.35\,V$)

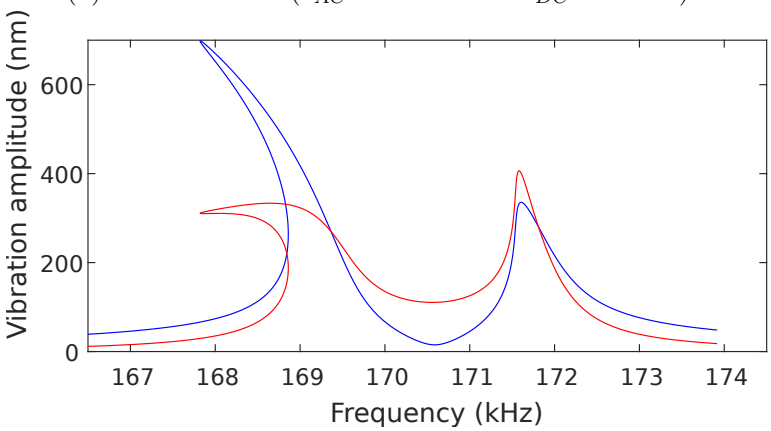

(c) DC voltage above the DC balancing voltage ($v_{AC} = 75\,mV$ and $V_{DC} = 6.65\,V$)

Figure 2.9: Frequency responses of the device with high vibration amplitudes

voltage is required to balance the device ($6.35\,V$ instead of $6.64\,V$). It is due to the additional softening effects of electrostatic nonlinearities which appear when the vibration amplitudes increase. We also notice that the short and the long cantilevers exhibit a softening behavior, and the frequency response curve is bent to the left for each mode. As the long cantilever is connected to the shorter one, there is a bifurcation topology transfer [126] between the two resonators when the sensor is driven beyond its critical amplitude [26]. Consequently, the long cantilever also shows a softening behavior even if it is not electrostatically actuated.

2.6 Summary

In this chapter, the proposed device using attractive electrostatic forces has been presented. The use of electrostatic softening effects on a device composed of two coupled cantilevers with different lengths has been proposed to counterbalance the problems of manufacturing defects. The analytical model based on Euler-Bernoulli beams has been presented, allowing us to choose the appropriate length difference according to the DC voltage required to balance the device. This model also takes into account the coupling beam, allowing us to design it according to the minimum coupling ratio. For the dynamic analysis with forced vibrations, the Galerkin discretization with one mode has been used, and the method of multiple scales has been applied to solve the equation. This enabled us to study the frequency response of the device at the balanced state in both linear and nonlinear regimes. It was found that the electrostatic nonlinearity can affect the DC balancing voltage.
Once the design completed, we can present the fabricated device and proceed with the experimental investigation in the next chapter.

Chapter 3

Experimental investigation and functionalization of electrostatic nonlinearities

Contents

3.1 Introduction

This chapter deals with the experimental investigation on the fabricated devices and the validation of the proposed model. We first consider devices composed of single cantilevers in order to determine unknown parameters concerning the material properties used and the clamping condition of the microbeams. We then consider the devices with two coupled cantilevers, and validate the proposed model by comparing experimental and theoretical results. Concerning the mass sensing, we have seen in Section 1.5.2 that the sensitivity of mode localized mass sensor is limited by the minimum coupling imposed by the mode aliasing. But it only concerns devices with linear resonators, and the effects of nonlinearities on mode localized mass sensors have not yet been investigated. In the litterature, nonlinearities have already been exploited in order to improve the performances of some devices in terms of autonomy, sensitivity, resolution and output power. One can cite the use of nonlinearities to increase the bandwidth of energy harvester [127–129], the use of simultaneous resonance for dynamic stabilization of nanomechanical resonators [130], and the nonlinearity cancellation [26,131,132] allowing to enhance the dynamic range of single NEMS resonators. In our case, we propose to functionalize electrostatic nonlinearities to overcome the sensitivity limitation of mode localized sensors. So, we also present this concept in this chapter. It includes both theoretical and experimental demonstrations.

3.2 The fabricated devices

We have fabricated the devices with the MUMPS® process (Run #124), and they are on chips of $5 * 5\,mm^2$. As shown in Figure 3.1, the cantilevers are made with a single polysilicon layer Poly2, reinforced by a second polysilicon layer Poly1 at the fixed end.

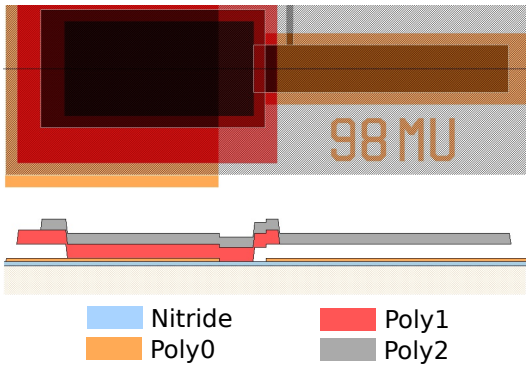

Figure 3.1: Top view and cross section of a cantilever

The dimensions of the device are the same as those given by the design. We have previously concluded that the best position for the coupling beam is $\tilde{x}_c = 5.5\,\mu m$, but we also consider the other positions at $\tilde{x}_c = 10.5\,\mu m$ and $\tilde{x}_c = 15.5\,\mu m$. The influence of the length of the coupling beam is not very important compared to that of its position, so it is fixed at $L_c = 65\,\mu m$. We finally have devices with three different coupling, and they are shown in Figure 3.2.

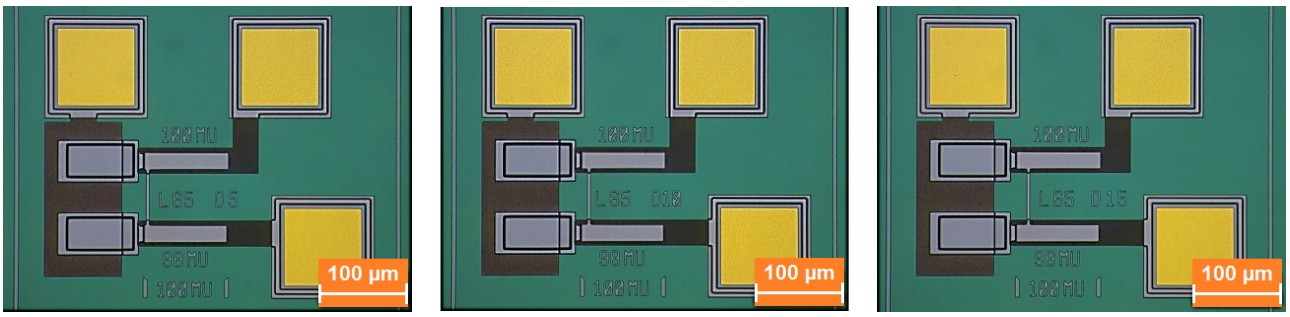

(a) Device 1 ($\tilde{x}_c = 5.5\,\mu m$) (b) Device 2 ($\tilde{x}_c = 10.5\,\mu m$) (c) Device 3 ($\tilde{x}_c = 15.5\,\mu m$)

Figure 3.2: Optical microscope image of the devices with two coupled cantilevers

3.3 Material properties used and characterization of the clamping condition

There are some parameters used in the model that are still unknown. The first parameter is the Young's modulus E of the polysilicon, which is expected to be between 150 and 170 GPa, and the second parameter is the stiffness of the rotational spring modeling the fixed end. To determine these parameters, we propose to use single cantilevers which are not coupled. These cantilevers are similar to those of the devices shown in Figure 3.2, but they are fabricated in another chip of a second run of fabrication (Run #128). They have a width of 20 μm, a thickness of 1.25 μm, and a length varying from 100 μm to 300 μm. We have four different cantilevers in total, and the principle consists in measuring their natural frequencies. From these results, we use the least squares method to find the best value of E and $\tilde{k}_e$.

3.3.1 Experimental setup

For the experimental setup, the chip containing the single cantilevers is placed in a vacuum chamber to decrease the pressure at around 0.50 $mbar$. To generate the vibrations, since the electrostatic actuation changes the natural frequency due to electrostatic softening, a piezoelectric transducer (Micro80, Mistras group) placed under the chip is used. Thus, we can actuate all the devices on the chip. The vibration at the free end of the cantilevers are then measured with a single point laser Doppler vibrometer (Polytec OFV-5000). The illustration of the experimental setup is shown in Figure 3.3.
The lengths and the natural frequencies of the four considered single cantilevers are given in Table 3.1.

Table 3.1: Lengths and natural frequencies of the single cantilevers

Length (μm)	First natural frequency (kHz)
100	161.250
110	133.310
200	40.870
300	18.240

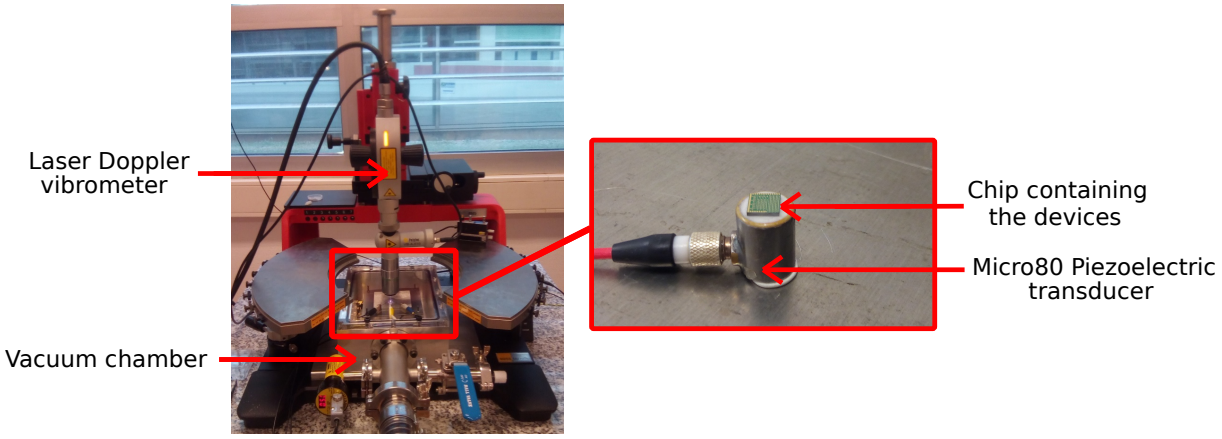

(a) The laser Doppler vibrometer and the piezoelectric transducer used

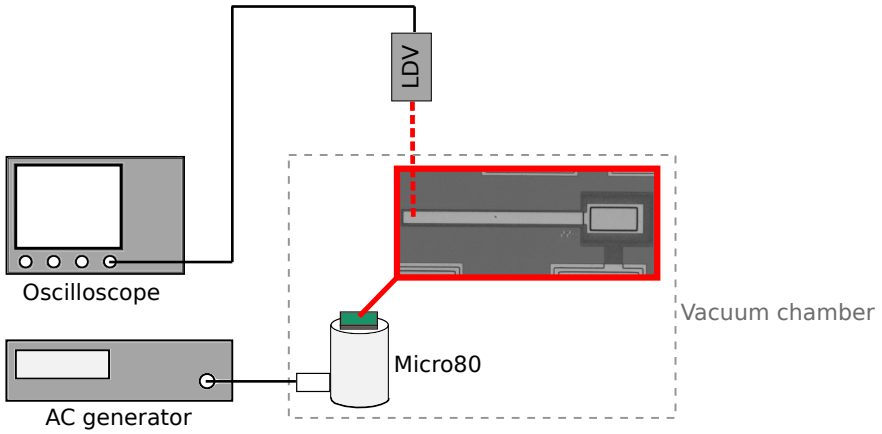

(b) Schematic of the experimental setup

Figure 3.3: Experimental setup for the measurement of the natural frequency of the single cantilevers

3.3.2 Determination of the Young's modulus E and the stiffness $\tilde{k}_e$ of the rotational spring modeling the fixed end

From the results given in Table 3.1, let's create a vector L and f given by

$$L = \begin{bmatrix} 100 \\ 110 \\ 200 \\ 300 \end{bmatrix} ; \quad f = \begin{bmatrix} 161250 \\ 133310 \\ 40870 \\ 18240 \end{bmatrix} \tag{3.1}$$

From the study of single cantilevers with a flexible support in Appendix A.4, the equation relating E and $\tilde{k}_e$ for each length and frequency of the vectors L and f is given by

$$g_j(E, \tilde{k}_e) = \frac{\tilde{k}_e}{EI\tilde{\lambda}(j)} \left[\cos\left(\tilde{\lambda}(j)L(j)\right)\cosh\left(\tilde{\lambda}(j)L(j)\right) + 1\right] + \cos\left(\tilde{\lambda}(j)L(j)\right)\sinh\left(\tilde{\lambda}(j)L(j)\right) - \sin\left(\tilde{\lambda}(j)L(j)\right)\cosh\left(\tilde{\lambda}(j)L(j)\right) = 0 \tag{3.2}$$

where

$$\tilde{\lambda}(j) = \sqrt{2\pi f(j)\sqrt{\frac{\rho b h}{EI}}} \quad \text{and} \quad j = 1, 2, 3, 4 \tag{3.3}$$

Since the equations are nonlinear and more numerous than unknowns, we propose to use the nonlinear least squares method to find the best value of E and $\tilde{k}_e$. It consists in defining the Jacobian matrix

$$J = \begin{bmatrix} \frac{\partial}{\partial E} g_1\left(E, \tilde{k}_e\right) & \frac{\partial}{\partial \tilde{k}_e} g_1\left(E, \tilde{k}_e\right) \\ \vdots & \vdots \\ \frac{\partial}{\partial E} g_4\left(E, \tilde{k}_e\right) & \frac{\partial}{\partial \tilde{k}_e} g_4\left(E, \tilde{k}_e\right) \end{bmatrix} \tag{3.4}$$

E and $\tilde{k}_e$ are then determined with an iterative calculation

$$\begin{bmatrix} E \\ \tilde{k}_e \end{bmatrix}_{k+1} = \begin{bmatrix} E \\ \tilde{k}_e \end{bmatrix}_k + \left(J^T J\right)^{-1} J^T \Delta y \tag{3.5}$$

where

$$\Delta y = \begin{bmatrix} g_1\left(E, \tilde{k}_e\right)_k \\ \vdots \\ g_4\left(E, \tilde{k}_e\right)_k \end{bmatrix} \tag{3.6}$$

By setting

$$\begin{bmatrix} E \\ \tilde{k}_e \end{bmatrix}_0 = \begin{bmatrix} 150\,10^9 \\ 1\,10^{-7} \end{bmatrix} \tag{3.7}$$

the results are given in Figure 3.4

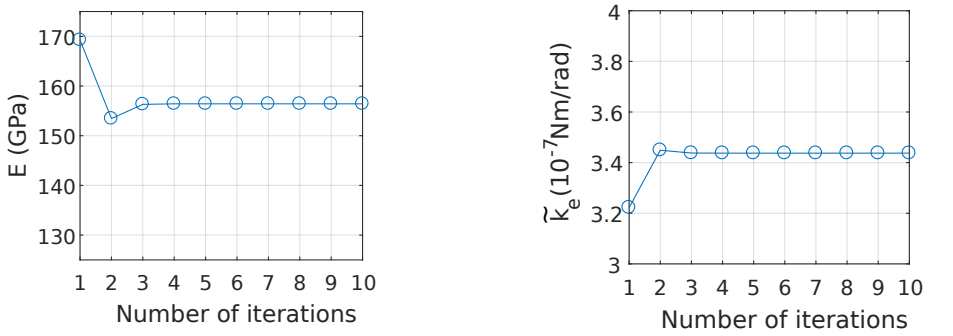

(a) Young's modulus (b) Stiffness of the rotational spring

Figure 3.4: E and $\tilde{k}_e$ as a function of the number of iterations

After just four iterations, results converge and we obtain

$$E = 156\,GPa \quad \text{and} \quad \tilde{k}_e = 3.43\,10^{-7} Nm/rad \tag{3.8}$$

These values will then be used in the proposed model of the device with coupled cantilevers.

3.4 Static deflection

Once we have determined the Young's modulus and the stiffness of the rotational spring modeling the fixed end of the cantilevers, we can proceed to the model validation. The first validation consists in comparing the experimental and theoretical static deflections of the cantilevers.

3.4.1 Experimental setup

For the experimental measurement of the static deflection, we consider the device with a coupling beam at $\tilde{x}_c = 5.5\,\mu m$ (Figure 3.2a). A DC voltage is applied on the electrode under the short cantilever, while the two cantilevers and the electrode under the long cantilever are grounded. The deflection of each cantilevers is then measured with an optical interferometer (Figure 3.5).

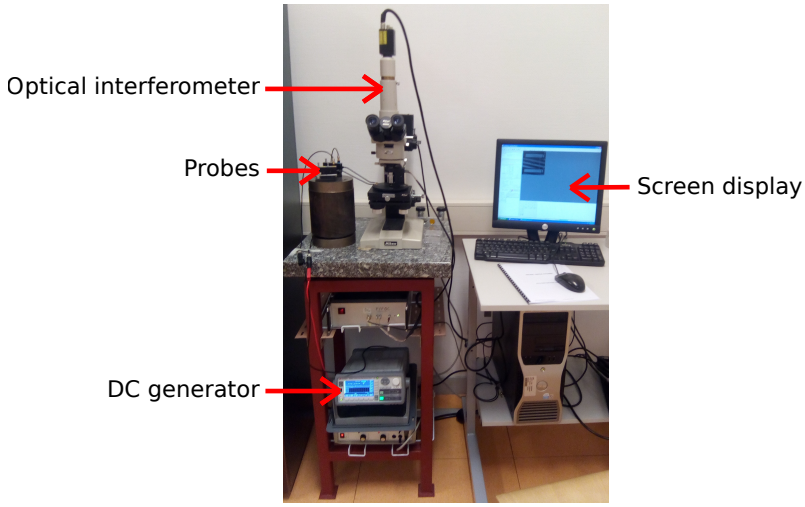

Figure 3.5: Experimental setup for the measurement of the static deflection of the cantilevers

After measurements, the topography of the device is obtained (Figure 3.6a) as well as the profile of each cantilever for some DC voltage values (Figure 3.6b and Figure 3.6c).
From these profiles, the measured gap is $g = 1.29\,\mu m$. We notice in Figure 3.6b that the short cantilever sticks to the bottom electrode for a DC voltage of $15.3\,V$. Consequently, this corresponds to the pull-in voltage of the short cantilever. For the long cantilever (Figure 3.6c), the deflection is not important regardless of the applied DC voltage. It is due to the weak coupling between the two cantilevers.

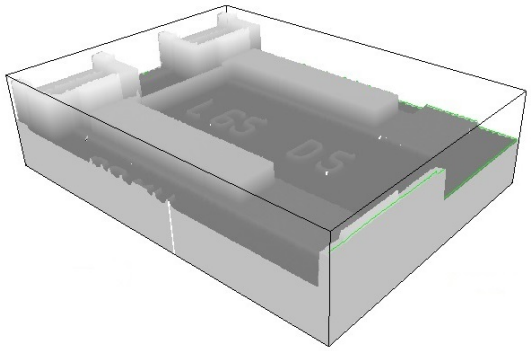

(a) Topography of the device with coupled cantilevers

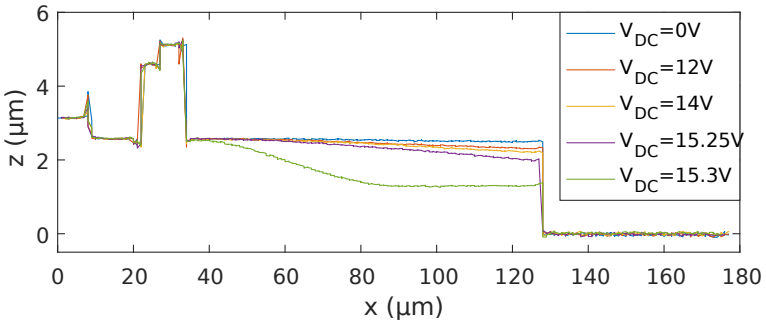

(b) Profile of the short cantilever

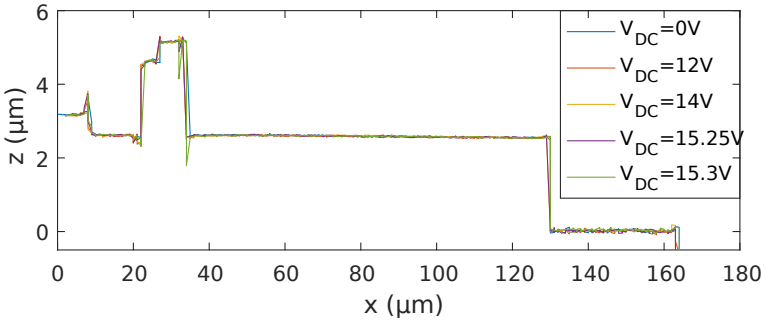

(c) Profile of the long cantilever

Figure 3.6: Topography of the device and profile of each cantilever (the fixed end is on the left side)

3.4.2 Comparison between experimental and theoretical results

After experimental measurements, we compare the theoretical and experimental static deflections at the end of each cantilever. The experimental static deflection is determined from the profile of the cantilevers while the theoretical static deflection is calculated with the model. We use the measured gap for the model, and the results are shown in Figure 3.7.

The comparison shows that we have a good agreement between experimental and theoretical results, although there is a noticeable difference when the DC voltage exceeds $12\,V$. With the DC balancing voltage which is about half of the pull-in voltage, the static deflection is about $100\,nm$ and the model is predictive. When actuated, the short cantilever will vibrate around this equilibrium position which is close to $10\,\%$ of the gap.

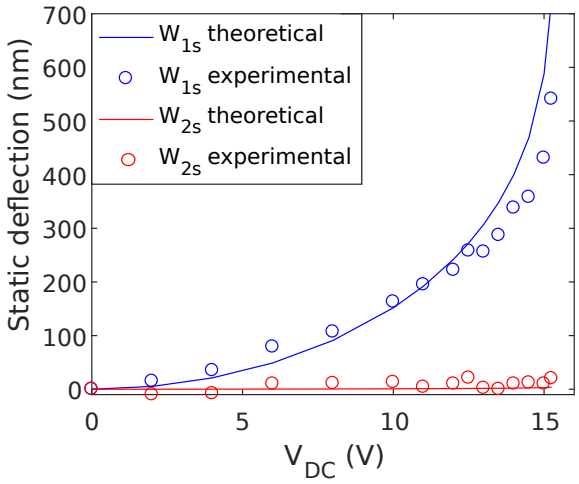

Figure 3.7: Static deflection of each cantilever as a function of the applied DC voltage

3.5 Dynamic response

After the static deflection, we study the dynamic response of the device with coupled cantilevers by actuating electrostatically the short cantilever.

3.5.1 Experimental setup

For the experimental setup, we also put the chip containing the device in the vacuum chamber. The vibration is then generated by using probes connected to a generator. We use again the single point laser Doppler vibrometer to measure the vibration at the end of each cantilever. As the results of interest are the frequency responses of each cantilever, we use a Picoscope® 5444B to automatically collect the data. As illustrated in Figure 3.8, this PC based oscilloscope is piloted with a MATLAB® R2019 program to produce the AC actuation voltage and to obtain the signal coming from the laser Doppler vibrometer.

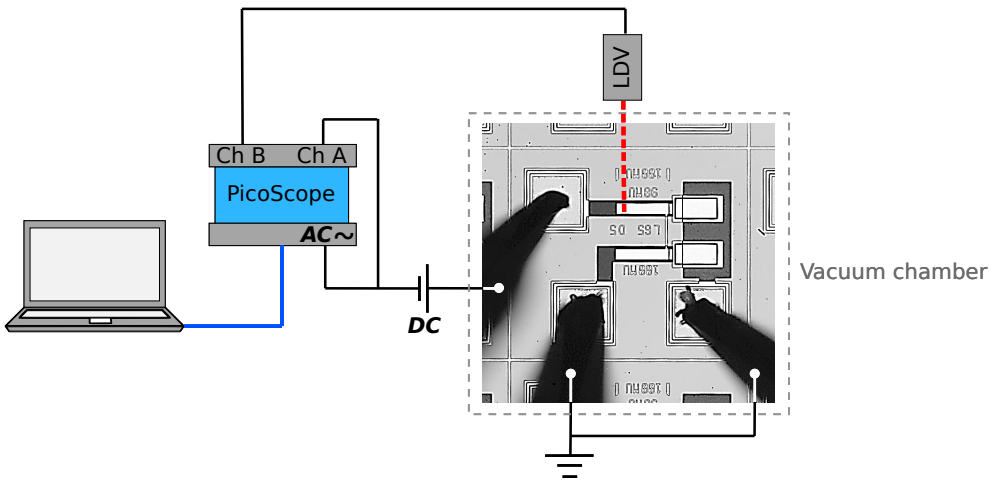

Figure 3.8: Experimental setup for the frequency responses of the devices with coupled cantilevers

3.5.2 Comparison between experimental and theoretical results

To validate the model, the results given by the experimental measurements are compared with those given by the analytical model.

For the experimental results, we consider the three devices with three different coupling, which are shown in Figure 3.2. The experimental measurements are carried out from the experimental setup shown previously.

For the theoretical results, we use the analytical model and perform the simulation with the given dimensions and parameters. However, there are some parameters which are identified experimentally. The first parameter is the quality factor Q. There are theoretical approaches to determine its value, but they are not very predictive. For cantilevers vibrating in air, the quality factor depends on extrinsic loss (viscous losses and acoustic radiation) and intrinsic loss (support loss, thermoelastic damping, volume loss and surface loss) [133]. For cantilevers vibrating at moderately low pressure, the viscous damping with rarefied gas effect is shown to be dominant [134]. In addition to it, attachment loss [135] can also be among the main damping source. But all of these losses mechanisms are complex and it does not allow us to estimate the quality factor with a high accuracy. So, it is determined directly from experimental results by using the half-power bandwidth method on a single cantilever on the same chip, and with the same dimensions.
The second parameter is the torsional spring which modelizes the actual clamping condition. We have already calculated this parameter in Section 3.3 ($\tilde{k}_e = 3.43\,10^{-7} Nm/rad$), but the clamping condition of the cantilevers may vary slightly from one device to another. At the veering point, the coupling beam does not interfere in the vibration when the two cantilevers vibrate in phase. Therefore, the frequency of the symmetric mode is equal to the natural frequency of each resonator, i.e. the natural frequency of the long cantilever, or the natural frequency of the short cantilever under the softening effect of the DC voltage. So, if the clamping condition is the same for each device, the frequency of the symmetric mode should also be the same, regardless of the coupling. However, experimental measurements show that this is not the case. Thus, we have adjusted the value of this parameter so that the theoretical and experimental frequencies of the symmetric mode are identical.
And the last parameter is the gap. It is first measured, but we then adjust the obtained value so that the experimental and theoretical DC balancing voltages are identical.

Frequency loci veering and amplitude ratio

The first results that we compare are the frequencies and the amplitude ratios of the two cantilevers (W_1/W_2) for each mode (the in-phase mode and the out-of-phase mode) as a function of the applied DC voltage. The simulation is performed with the parameters in Table 3.2 that are identified from the experimental measurement on Device 2, and the results are shown in Figure 3.9.

Table 3.2: Parameters used for the model

Parameter	Value
Q	450 ($p \approx 0.60\,mbar$)
$\tilde{k}_e$	$3\,10^{-7}\,Nm/rad$
g	$1.12\,\mu m$

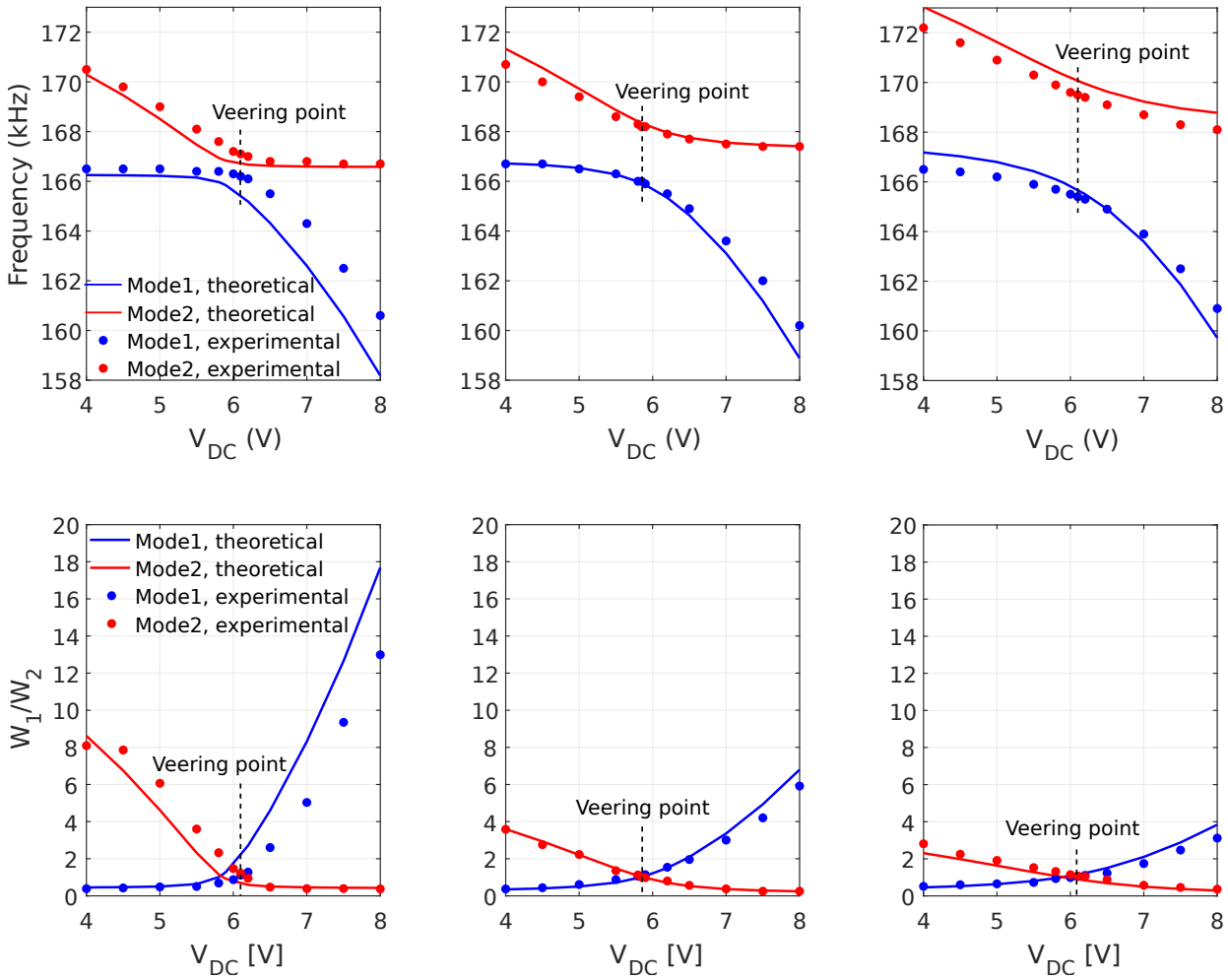

(a) Device 1 (b) Device 2 (c) Device 3

Figure 3.9: Frequencies of each mode and amplitude ratio for each mode as a function of the DC voltage

Concerning the balanced state, it is reached at the veering point. This corresponds to the case where the frequencies of each mode are the closest to each other, and the amplitude ratio is equal to one. At this state, the mode shapes of the coupled microbeams are similar to those of a device with two cantilevers exactly identical. They correspond to the symmetric and antisymmetric modes.
At this balanced state, the theoretical DC balancing voltage of the three devices is equal to $5.85\,V$, while the experimental DC balancing voltage is equal to $6.10\,V$ for Device 1, $5.85\,V$ for Device 2, and $6.10\,V$ for Device 3. Normally, the DC balancing voltage does not depend on the position of the coupling beam, that is why its theoretical value remains unchanged for the three devices. But

in reality, we have manufacturing defects which mean that the three devices do not have exactly the same dimensions even if they are placed beside each other in the chip. On each device, we can have small imperfections such as the non-uniformity of the thicknesses or planar dimensions, and they can all affect the value of the DC balancing voltage.
Concerning the frequency of the in-phase mode at the veering point (symmetric mode), its theoretical value is equal to $166.0\,kHz$ for the three devices, while the experimental measurement gives $166.3\,kHz$ for Device 1, $166.0\,kHz$ for Device 2, and $165.3\,kHz$ for Device 3. Normally, only the frequency of the antisymmetric mode depends on the coupling ratio. The frequency of the symmetric mode should be the same regardless of the position of the coupling beam. If we look at the results of the FEM model in Table 2.3, there are just slight differences due to the effect of the mass of the coupling beam, but they are not important. But if we have these experimental frequencies which are different, it is because the three devices are not exactly identical. The clamping condition can also be different from one device to another. As the torsional stiffness $\tilde{k}_e$ is identified only from Device 2, the frequencies are in good agreement for this device, but its is not the case for the others.

For the pull-in instability, the DC balancing voltage that we use are all low compared to the static pull-in voltage which is around $12\,V$. It means that the length difference between the two designed cantilevers is suitable for the device. We notice that this pull-in voltage is lower than that of the device used for the study of the static deflection in Section 3.4. It is due to the fact that these devices belong to different chips, and they do not have the same gap.

When we are not at the veering point, the amplitude ratio shows that the vibration on either side of the balancing state is localized. The vibration of the first mode is localized on the softest microbeam and that of the second mode is localized on the stiffest microbeam. With the same applied DC voltage, the vibration is more localized for Device 1. Indeed, a DC voltage not corresponding to the balanced state constitutes a stiffness perturbation, and the device with the weakest coupling is the most sensitive. The theoretical results of the amplitude ratio show a curve with the same shape, but the difference with the experimental results is more important when the DC voltage is too low or too high. In Device 1, these cases correspond to the mode (1; 0) or the mode (0; 1). In these modes, the vibration is localized in one of the two cantilevers, and the vibration amplitude of the other one becomes too small to be accurately measured.

If we look at Figure 3.9 in general, the comparison shows that the theoretical results fit the experimental results. Both results show the same trends, but we notice a slight offset between the curves in Figures 3.9a and 3.9c, which correspond to Device 1 and Device 3. It is due to the fact that some parameters are identified from the experimental measurement on Device 2, while they may vary from one device to another. This is confirmed by the fact that the experimental frequencies of the symmetric mode and the experimental DC balancing voltages are different for the three considered devices, while they do not depend on the coupling ratio. By testing other devices in the same chip, the frequencies of the symmetric mode vary from $162.0\,kHz$ to $166.3\,kHz$, with an average of $165.2\,kHz$ and a standard deviation of $1.4\,kHz$, while the DC balancing voltage is between $5.85\,V$ and $7\,V$, with an average of

$6.20\,V$ and a standard deviation of $0.4\,V$. This also confirms the disparity between each device.

Frequency responses at the veering point

The second result that we compare is the frequency response at the balanced state. We consider Device 2 and two cases are studied: the linear case involving low vibration amplitudes and the nonlinear case involving high vibration amplitudes.

- Linear frequency response at the veering point

For the linear case, we use $v_{AC} = 10\,mV$ and $V_{DC} = 5.85\,V$, and the results are shown in Figure 3.10.

The amplitude responses (Figures 3.10a and 3.10b) show that we have the same amplitude on both cantilevers at the resonance, so we get the symmetric and the antisymmetric modes. The comparison also shows that there is a good agreement between both results obtained from the model and from experimental measurement. As the difference between the frequencies of the two modes depends on the coupling parameter, this result implies that the modeling of the coupling beam is validated. It can also be verified in the two other devices by comparing the difference between the frequencies of the two modes at the veering point (Figures 3.9b and 3.9c). Concerning the phase response, we note in Figure 3.10c that the phase shift between the vibrations of the two cantilevers and the excitation is equal to $-90°$ for the symmetric mode. This same phase shift means that the two cantilevers vibrate in-phase. For the antisymmetric mode, the phase shift of the short cantilever is $-90°$ while that of the long cantilever is $-270°$. The difference of $180°$ between the phase of the two cantilevers means that their vibrations are out-of-phase.

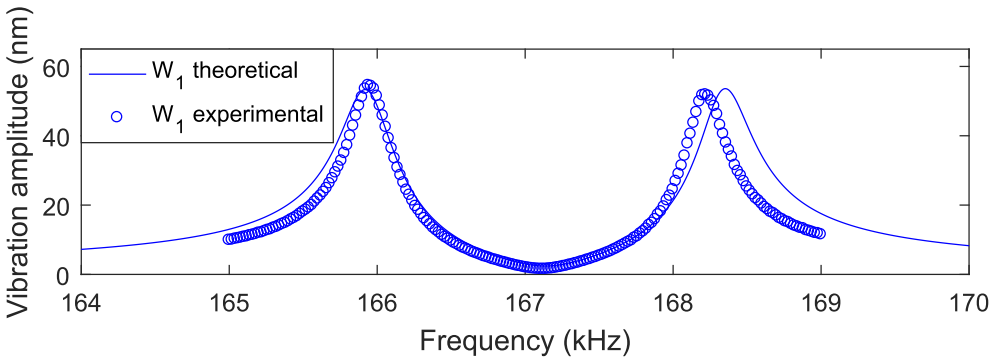

(a) Short cantilever

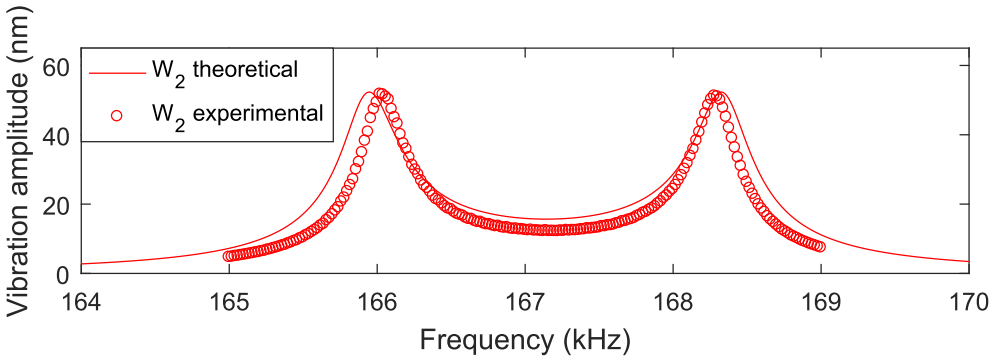

(b) Long cantilever

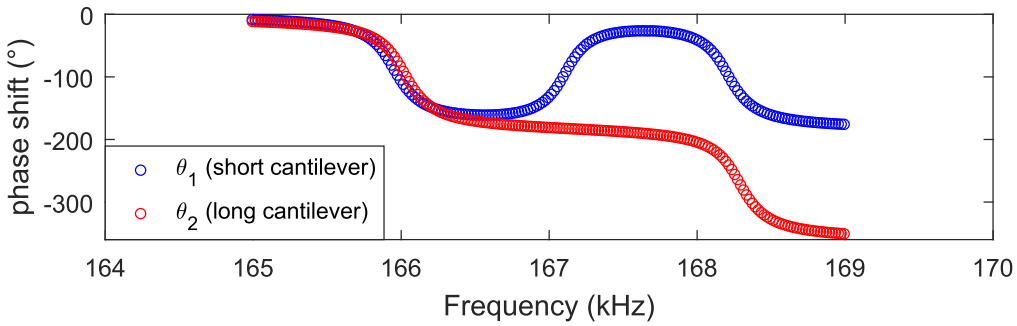

(c) Experimental phase response

Figure 3.10: Theoretical and experimental frequency responses of Device 2 at the balanced state and with low vibration amplitudes ($v_{AC} = 10\,mV$ and $V_{DC} = 5.85\,V$)

- Nonlinear frequency response at the veering point

For the nonlinear case, we use $v_{AC} = 60\,mV$ and $V_{DC} = 5.60\,V$, and the results are shown in Figure 3.11.

At the veering point, the experimental amplitude responses in Figures 3.11a and 3.11b show that we still have identical amplitude on both cantilevers. But due to the electrostatic nonlinearities, we notice that the frequency response in both vibration modes is bent to the left. We can also notice that the DC voltage to counterbalance the length difference drops to $5.60\,V$, because of the additional softening effect of the electrostatic nonlinearities. For the theoretical amplitude responses, we have a slight difference when we use the same actuation voltage. It could be due to the parameters used in the model,

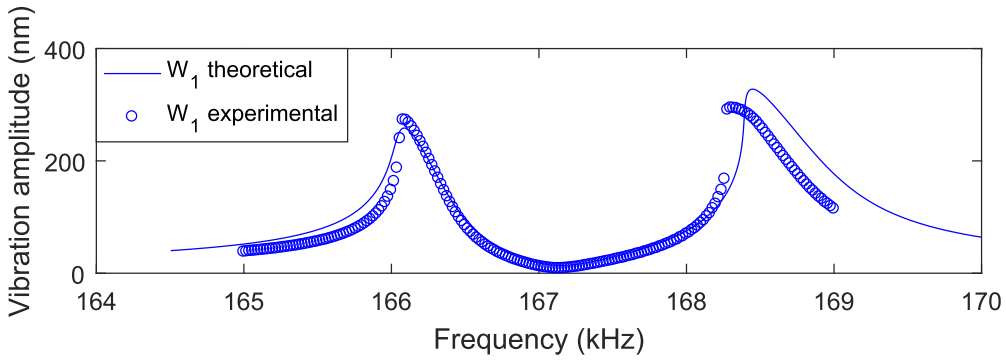

(a) Short cantilever

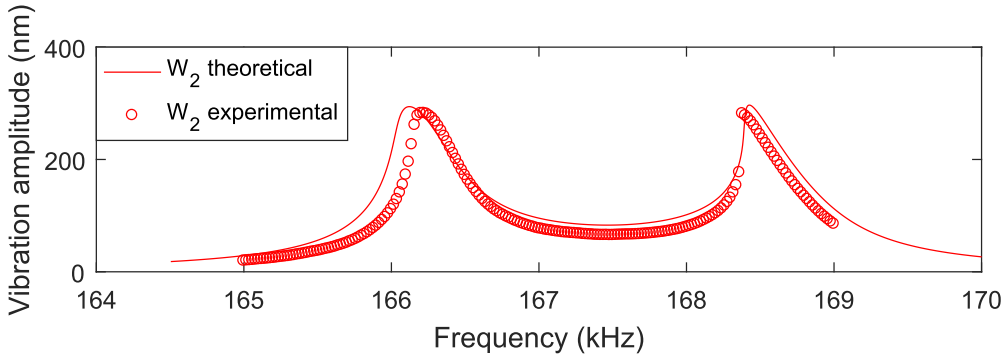

(b) Long cantilever

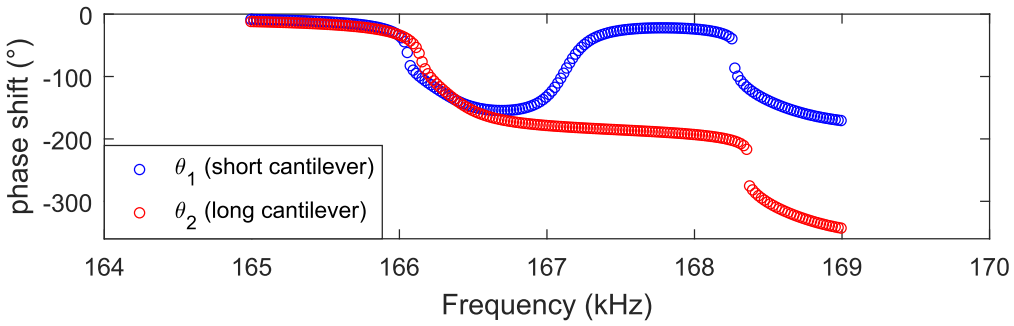

(c) Experimental phase response

Figure 3.11: Theoretical and experimental frequency responses of Device 2 at the balanced state and with high vibration amplitudes ($v_{AC} = 60\,mV$ and $V_{DC} = 5.60\,V$)

which are related to electrostatic nonlinearities, like the quality factor or the capacitor gap. For the phase response in Figure 3.11c, we still have the difference of 0° and 180° between the phase of the two cantilevers on the symmetric and antisymmetric modes. They reflect the in-phase and out-of-phase vibrations in these two modes.

3.6 Mass detection and functionalization of electrostatic nonlinearities

In this section, we investigate the mass detection with the fabricated device. We also demonstrate both theoretically and experimentally the functionalization of the electrostatic nonlinearities for the mass sensing. It consists in implementing and tuning them in order to improve the device performances.

3.6.1 Principle of the functionalization of electrostatic nonlinearities

In order to investigate the effects of electrostatic nonlinearities on the mode localization, we start by reviewing its principle. When two identical resonators are weakly coupled, we have two modes of vibration corresponding to the symmetric and the antisymmetric modes, as illustrated in Figure 3.12a. When a small mass perturbation is added on the first resonator only, its resonance frequency decreases, so it vibrates more in the first mode of the coupled system, i.e., at the lowest frequency. The second resonator vibrates more in the second mode of the coupled system. The vibration of the system thus becomes localized on the first resonator for the first mode, and on the second one for the second mode, as illustrated in Figure 3.12b. Because only the first resonator is actuated to generate the vibration of the system, the mode localization will be more marked on the first mode in terms of vibration amplitudes. So, it is better to use the ratio of vibration amplitudes on mode 1 as output metrics to measure the mass perturbation. By plotting the added mass as a function of this amplitude ratio, we get the sensitivity of the device. In linear regime, this sensitivity only depends on the coupling. It increases as the coupling decreases, but it is limited by the minimum coupling.

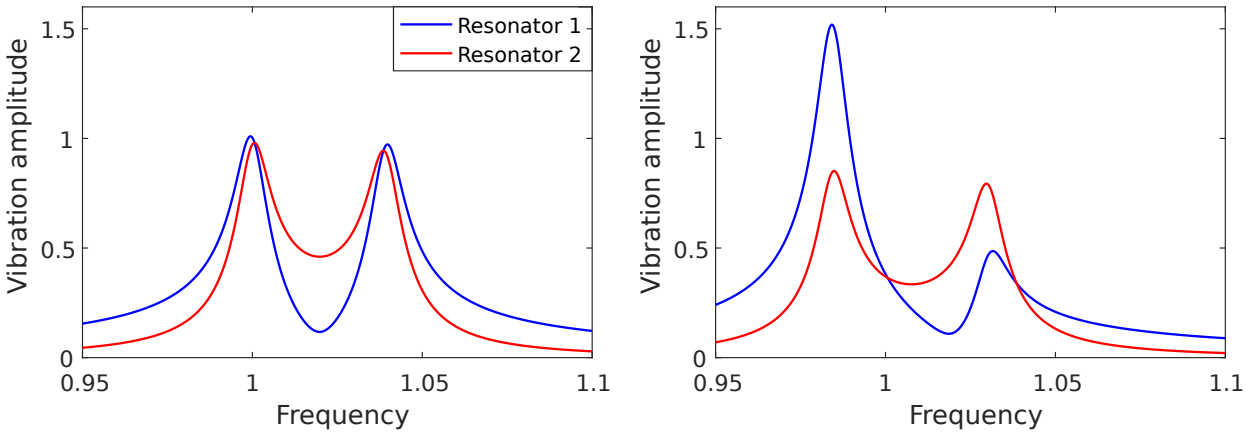

(a) Without a mass perturbation

(b) With a mass on Resonator 1

Figure 3.12: Effect of a mass perturbation on the amplitude response of linear mode localized sensors

If we now introduce electrostatic nonlinearities in the first resonator, its resonance frequency becomes amplitude-dependent. More precisely, the nonlinearity bends the frequency response graph to the left when the vibration amplitude increases, so the resonance frequency decreases, as illustrated in Figure 3.13. This appears when we only have electrostatic nonlinearity or when it is dominant, leading to a softening behavior.

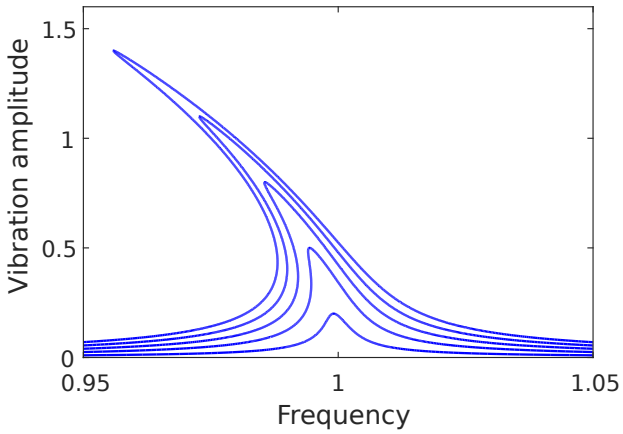

Figure 3.13: Amplitude dependence of the resonance frequency of a single resonator with electrostatic nonlinearities

We have on the one hand, the mass perturbation decreasing the resonance frequency and increasing the vibration amplitude of the first resonator on the first mode, and on the other hand, the electrostatic nonlinearities further decreasing the resonance frequency when the vibration amplitude increases. As the added mass and the nonlinearity both lead to a decrease in the resonance frequency, we should have a more localized vibration than in coupled linear resonators, for the same mass perturbation. Thus, the sensitivity of the sensor can be improved.

3.6.2 Theoretical demonstration

In order to highlight the benefits of electrostatic nonlinearities on mass sensing, we perform several simulations with the model. To be near the limit of the mode aliasing, we use the dimensions of Device 1 which has the weakest coupling.

We first consider the linear case and find the DC voltage balancing the system. With a capacitance gap $g = 1.24\,\mu m$ and a quality factor $Q = 770$, the theoretical frequency response of the device at the balanced state is shown in Figure 3.14a, where the actuation is $v_{AC} = 6\,mV$ and $V_{DC} = 6.82\,V$. If we add a discrete point mass of $10\,pg$ at the end of the short cantilever, the vibration becomes localized as shown in Figure 3.14b. On the first mode, the ratio between the amplitude of the short cantilever and the long cantilever which is initially close to 1 becomes $W_1/W_2 = 2.2$ (measured on the circled dots). Afterwards, we perform simulations with a high AC voltage. The result is shown in Figure 3.14c in which the actuation is $v_{AC} = 25\,mV$ and $V_{DC} = 6.74\,V$. We notice that a lower DC voltage is required because of the additional softening effect of the electrostatic nonlinearities. With the same added mass of 10 pg, the result in Figure 3.14d shows that the vibration on the first mode is more localized than in the linear case. The amplitude ratio on the first mode becomes $W_1/W_2 = 3$. If we increase again the vibration amplitude by using $v_{AC} = 35\,mV$ and $V_{DC} = 6.67\,V$ (Figure 3.14e), the amplitude ratio after adding the same mass becomes $W_1/W_2 = 4.2$ (Figure 3.14f).

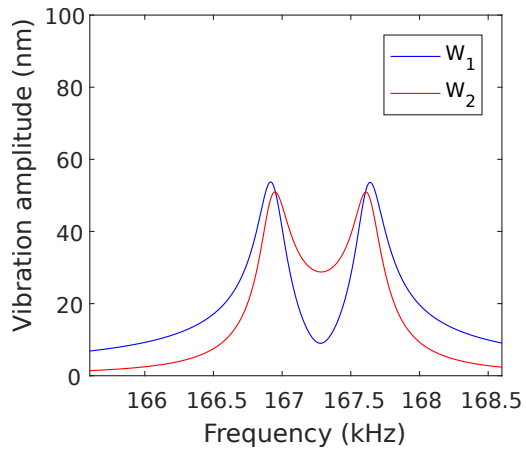

(a) $\tilde{m} = 0\,pg$, $v_{AC} = 6\,mV$ and $V_{DC} = 6.82\,V$

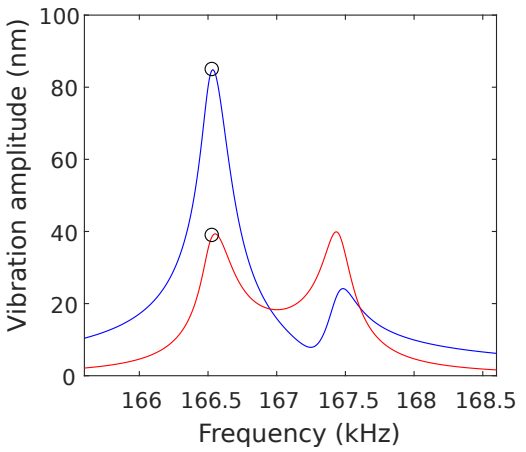

(b) $\tilde{m} = 10\,pg$, $v_{AC} = 6\,mV$ and $V_{DC} = 6.82\,V$

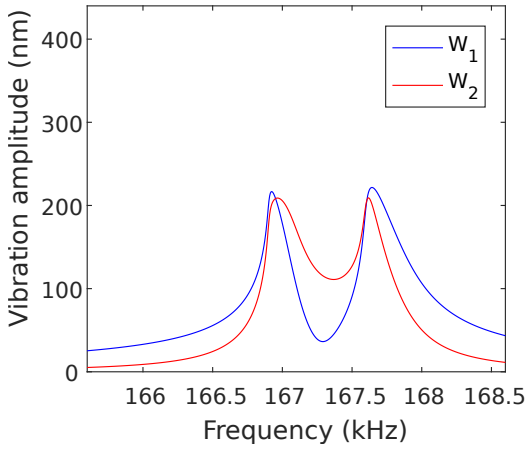

(c) $\tilde{m} = 0\,pg$, $v_{AC} = 25\,mV$ and $V_{DC} = 6.74\,V$

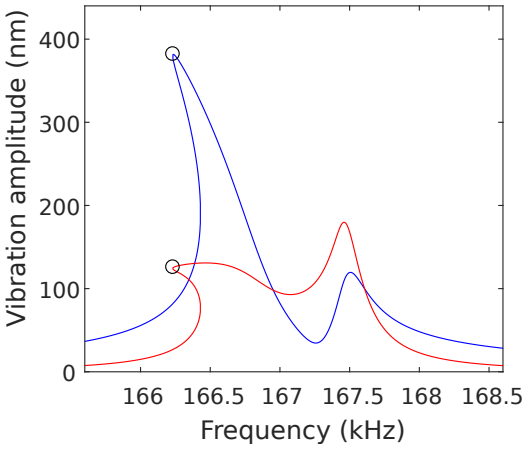

(d) $\tilde{m} = 10\,pg$, $v_{AC} = 25\,mV$ and $V_{DC} = 6.74\,V$

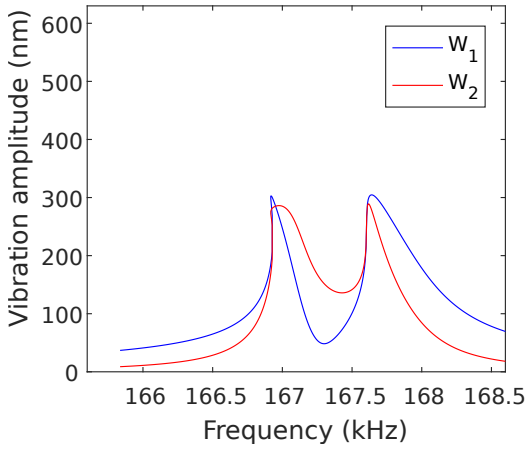

(e) $\tilde{m} = 0\,pg$, $v_{AC} = 35\,mV$ and $V_{DC} = 6.67\,V$

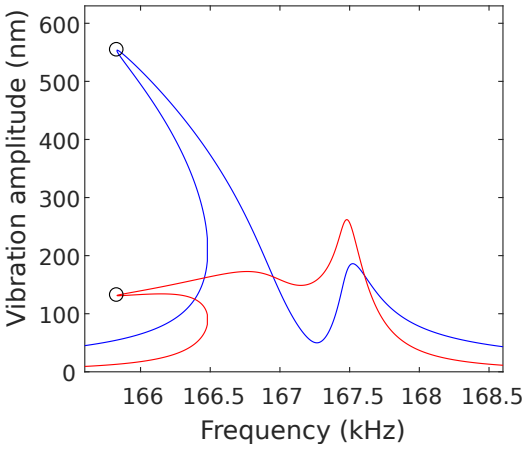

(f) $\tilde{m} = 10\,pg$, $v_{AC} = 35\,mV$ and $V_{DC} = 6.67\,V$

Figure 3.14: Theoretical frequency responses of the device before and after adding a discrete point mass of $10\,pg$ at the end of the short cantilever

To study the sensor sensitivity, we perform simulations over a mass range from $0\,pg$ to $10\,pg$ for different values of the AC voltage, and the results are shown in Figure 3.15.

With an AC voltage lower than $6\,mV$, Figure 3.15 shows that the same amplitude ratio is obtained for a given added mass reflecting the linear regime. In this case, the amplitude ratio is still a linear

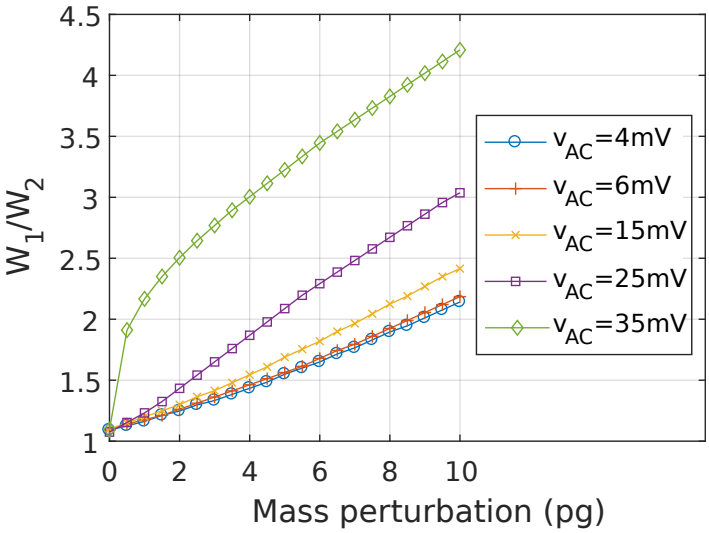

Figure 3.15: Variation of the amplitude ratio on the first mode as a function of the mass added at the end of the short cantilever and the AC voltage

function of the added mass. Therefore the sensitivity of the device remains constant, and it is around $0.12\,/pg$. The slope of the curve mass-amplitude ratio then increases as the AC voltage increases. The sensitivity becomes $0.20\,/pg$ for $v_{AC} = 25\,mV$. Thus, by introducing electrostatic nonlinearities, the sensitivity of the device has been increased by about $67\,\%$. As the coupling ratio is at its optimal value in terms of sensitivity in the linear regime (i.e., close to the value for which the mode aliasing appears), it can be considered that this limit has been overcome by the implementation of electrostatic nonlinearities.

With a very high AC voltage ($v_{AC} = 35\,mV$), we still have a higher amplitude ratio, but it is no longer a linear function of the added mass. At first, the slope of the curve is very high, but it decreases afterwards. As the sensitivity of the device is not constant, this case is not suitable for mass sensing, but it can be used for mass detection.

3.6.3 Experimental verification

To validate the theoretical results, an experimental verification is also conducted. For that, we add a mass perturbation on the short cantilever of the device by using a focused ion beam deposition of platinum. The first step is to determine the density of the material used for the mass deposition. To achieve this, we deposit a larger mass at the free end of a single cantilever of $98\,\mu m$ length. We then measure its resonance frequency before and after the mass deposition. As a simplification, the effective mass of a cantilever is equal to one quarter of its mass [136]. The mass perturbation Δm_0 is then calculated from the following relation

$$\Delta m_0 = \frac{m_0 \Delta f_0}{2 f_0} * \frac{\phi_1^2(1)}{\phi_1^2(x_m)} \tag{3.9}$$

where $m_0 = 5911\,pg$ is the mass of the cantilever, $\Delta f_0 = 2.58\,kHz$ is the frequency shift, $f_0 = 170.90\,kHz$ is the resonance frequency before the mass deposition, and $x_m = 96/98$ is the normalized position of the added mass. The result gives us a mass around $47\,pg$, which corresponds to a density about $12.7\,kg/m^3$.

Once we have the density of the material used, we consider the device with coupled cantilevers. The device is first placed in the vacuum chamber and we measure the experimental frequency responses at the balanced state. To achieve this, we always use the vibrometer to measure the vibration at the end of each cantilever. Low and high actuating voltages are used in order to consider the linear and the nonlinear cases. Once the results are obtained, the device is placed in a scanning electron microscope (SEM), and a small mass perturbation is deposited at the end of the short cantilever. Figure 3.16 shows the SEM images of the device (Figure 3.16a) and the deposited mass (Figure 3.16b).

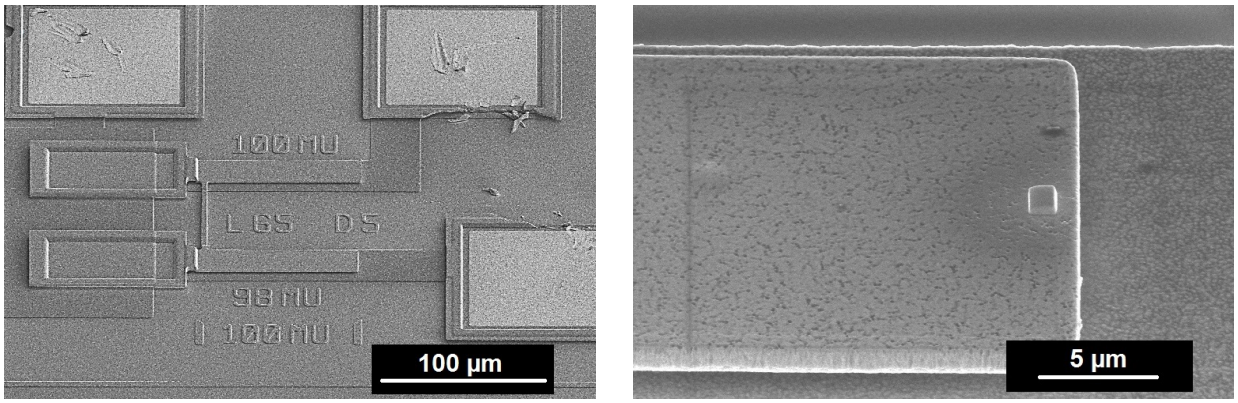

(a) SEM image of Device 1

(b) SEM image of the deposited mass at the end of the short cantilever

Figure 3.16: SEM image of the considered device and the deposited mass

From the material density, the deposited mass shown in Figure 3.16b is estimated to be about $10\,pg$. The device is then placed back into the vacuum chamber, and the experimental frequency responses are measured again. The results are shown in Figure 3.17.

Without the mass perturbation, Figure 3.17a corresponds to the experimental frequency response of the linear case where $v_{AC} = 6\,mV$ and $V_{DC} = 6.82\,V$, and Figure 3.17c corresponds to that of the nonlinear case where $v_{AC} = 25\,mV$ and $V_{DC} = 6.74\,V$. After adding the mass perturbation, we obtain the frequency responses shown in Figures 3.17b and 3.17d. The amplitude ratio of the first mode for the linear case is $W_1/W_2 = 2.3$ (Figure 3.17b, measured on the circled dots). With a higher AC voltage where the vibrations are nonlinear, Figure 3.17d gives an amplitude ratio equal to $W_1/W_2 = 3.9$. As shown by the simulation, the vibration of the sensor becomes more localized when the electrostatic nonlinearities are introduced at high vibration amplitudes. If we increase again the AC voltage, we should have a higher amplitude ratios like in the simulation. But experimentally, it becomes more difficult to obtain the balanced state by tuning the DC voltage because the system becomes too sensitive.

By comparing the results, we note a slight difference between experimental and theoretical amplitude

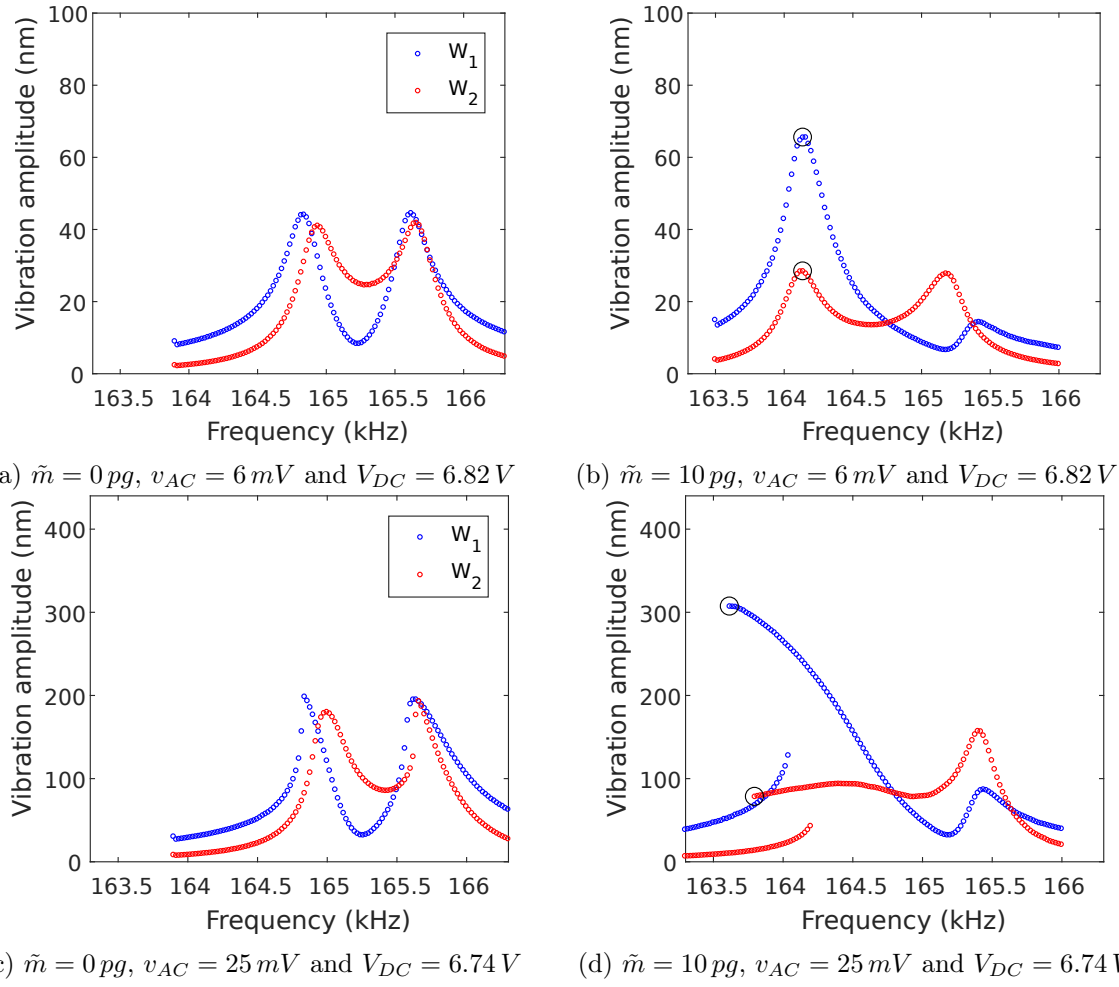

(a) $\tilde{m} = 0\,pg$, $v_{AC} = 6\,mV$ and $V_{DC} = 6.82\,V$

(b) $\tilde{m} = 10\,pg$, $v_{AC} = 6\,mV$ and $V_{DC} = 6.82\,V$

(c) $\tilde{m} = 0\,pg$, $v_{AC} = 25\,mV$ and $V_{DC} = 6.74\,V$

(d) $\tilde{m} = 10\,pg$, $v_{AC} = 25\,mV$ and $V_{DC} = 6.74\,V$

Figure 3.17: Experimental frequency responses of the device before and after adding a mass of $10\,pg$ at the end of the short cantilever

ratios in the nonlinear regime. It could be due to the fact that we have some uncertainties about the parameters used in the model. The first parameter concerns the quality factor which can change the vibration amplitude and the effect of electrostatic nonlinearities. As the pressure inside the vacuum chamber can change slightly, the quality factor before and after depositing the mass may not be the same. The second parameter concerns the gap which can change the cubic nonlinearity, the effect of electrostatic nonlinearities, and thus the sensitivity in the nonlinear regime. In addition, the analytical model may have limitations. A linear damping force is used while other authors proposed a model with a quadratic damping coefficient [137]. There is also the expression of the electrostatic force, a third order Taylor series is used to expand it in the model, but this method may not be very accurate with very high vibration amplitudes [138]. As the device is more sensitive when it is operated in the nonlinear regime, the influence of these uncertainties becomes more important.

3.7 Problems encountered on the measurements of the dynamic response and identification of their causes

3.7.1 Problems encountered

In the previous section, we used the amplitude ratio of the first mode to determine the added mass perturbation. In the simulation, this amplitude ratio corresponds to the quotient between the peak amplitudes of each cantilever, which are almost always at the same frequency (the frequency of the first mode). For the nonlinear case, the amplitudes before the jump phenomenon are used to calculate this ratio, and they are also at the same frequency. The fact that the considered amplitudes are on the same frequency allows the sensors to operate in closed-loop system, thus enabling a real-time measurements [139]. However, we notice that the experimental amplitude responses shown in Figure 3.17 are slightly different. If we take some of them back, we can see in Figure 3.18 that there is an offset between the frequencies at peak amplitude.

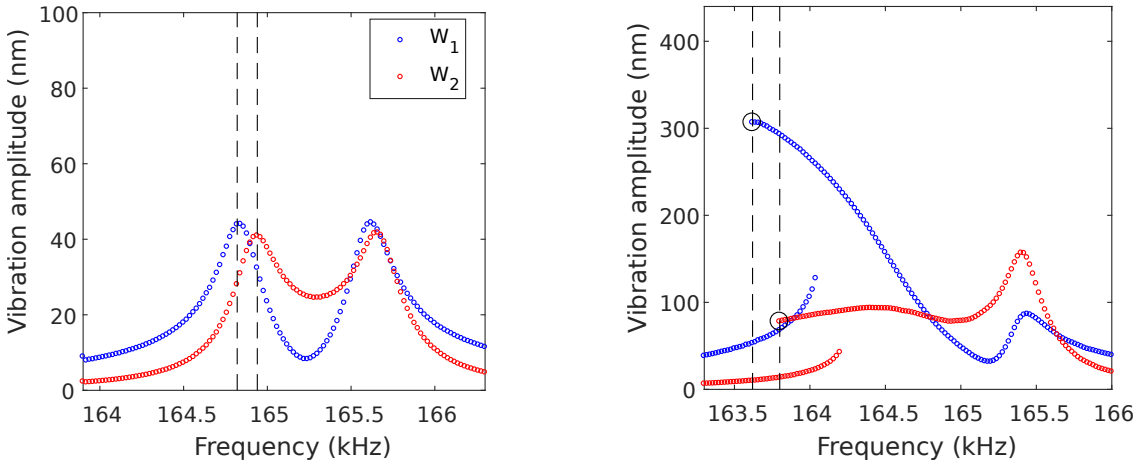

(a) Linear case and at the balanced state

(b) Nonlinear case and with a mass perturbation

Figure 3.18: Offset between the frequencies at peak amplitude

For the first mode at the balanced state, we notice in Figure 3.18a that the peak amplitude of the short cantilever (blue curve) is before that of the long cantilever (red curve). Theoretically, the two peak amplitudes of the red curve are between those of the blue curve, but the frequency difference is not as significant as in Figure 3.18a. For the the nonlinear case and with the mass perturbation (Figure 3.18b), the amplitude jumps of each cantilever do not appear at the same frequency. But in reality, this should not be possible because the two cantilevers are mechanically connected, and the longer one that is not actuated must behave like the shorter one.

To identify the cause of the offset between these experimental curves, we need to look at how we measure the vibration amplitudes. As we have a single point LDV, we do a first frequency sweep to get the blue curve, and a second one to get the red curve. For each measurement, the laser spot of the vibrometer is either on the short cantilever or on the long one. Some authors have already studied the effects of a vibrometer laser on MEMS devices. They show that it concerns mainly thermal effects [140],

that can lead to a thermoelastic bending [141, 142] and a shift of the resonance frequency [143]. In our case, we have two coupled cantilevers. If the vibrometer only perturbs the cantilever on which the amplitude measurement is made, the system will be in a different state each time the position of the laser spot changes, hence the difference between the two experimental curves. In order to verify this and ensure that we should not have this offset, another method is used to measure the vibration of the short cantilever while the vibration of the long cantilever is always measured with the LDV. With this measurement method, we can have the frequency response of both cantilevers while the position of the laser spot does not change.

3.7.2 Measurement of the vibration amplitudes of the short cantilever with an impedance analyzer

Experimental setup

To measure the vibration amplitudes of short cantilever, we use an impedance analyzer (Keysight E4990A) in addition to the LDV. As the short cantilever is electrostatically actuated, we can measure the motional current that is proportional to its vibration. For the long cantilever which is not actuated, the LDV is always used. In the experimental setup (Figure 3.19), the impedance analyzer supplies both the AC and the DC actuation voltages while the picoscope collects the data from the LDV. To synchronize the two measurements, the impedance analyzer is controlled by the picoscope with a trigger signal.

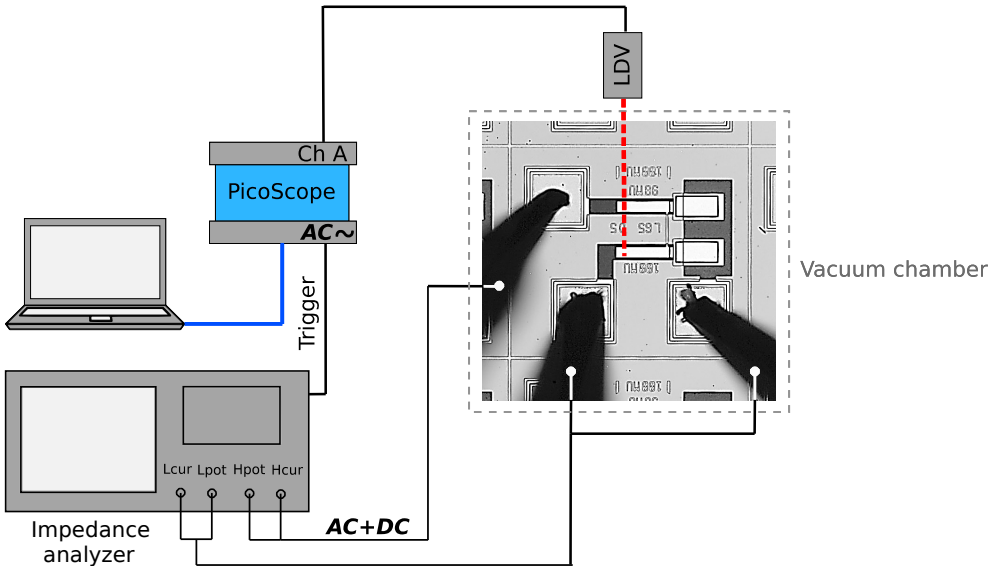

Figure 3.19: Experimental setup for the simultaneous measurement of the vibration amplitude of each cantilever by using the LDV and the impedance analyzer

Measurement of the motional current

For MEMS device with two coupled resonators, we can use the simplified equivalent electrical scheme shown in Figure 3.20 [144, 145].

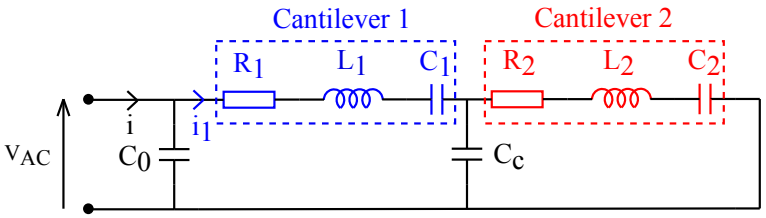

Figure 3.20: Equivalent electrical scheme of the device

In this figure, R_1, L_1 and C_1 represent the short cantilever, R_2, L_2 and C_2 represent the long cantilever, C_c represents the coupling beam, and C_0 represents the feedthrough capacitance which is composed of the static capacitance of the short cantilever and other parasitic capacitance. C_0 can be estimated from the admittance of the device when it is not driven around the resonance frequencies [26]. Afterwards, the motional current i_1 of the short cantilever is given by

$$i_1 = v_{AC} * \sqrt{(|Y|\cos(\arg(Y)))^2 + (|Y|\sin(\arg(Y)) - 2\pi f C_0)^2} \tag{3.10}$$

where Y is the admittance measured with the impedance analyzer, and f is the excitation frequency. We notice in the electrical scheme in Figure 3.20 that we should also have a motional current on the long cantilever. But in reality, the long cantilever and the electrode under it are grounded. So, only the vibrations of the short cantilever create a motional current.

3.7.3 Results

Comparison between the motional current and the vibration amplitudes

To ensure that the motional current can be used to characterize the vibration of the short cantilever, we first perform an experimental measurement where the laser of the vibrometer is on the short cantilever. A device with the weakest coupling (Device 1) is considered, and the two results from the LDV and the impedance analyzer are then compared. The measured admittance Y around the resonance frequency is shown in Figure 3.21a. We notice that for $|Y|$, we have antiresonances due to the feedthrough capacitance. When the device is not driven around its resonance frequency, the measured admittance corresponding to the electrical response of the feedthrough capacitor is shown in Figure 3.21b.
From this two results, we calculate the motional current i_1 as a function of the excitation frequency by using Equation (3.10). It is then compared with the vibration amplitude W_1 of the same cantilever measured with the LDV (Figure 3.22).
From Figure 3.22, we can say that the motional current is proportional to the vibration amplitude. So, it can be used to plot the frequency response of the short cantilever. In reality, the motional current is proportional to the vibration velocity, but as the variation of the frequency is negligible,

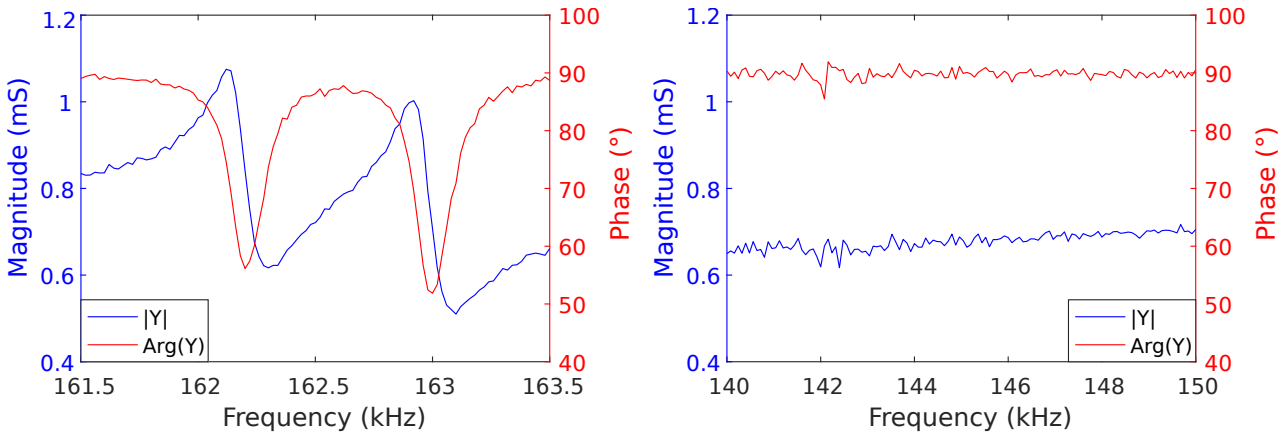

(a) Admittance around the resonance

(b) Off-resonance admittance

Figure 3.21: Admittance measured with the impedance analyzer

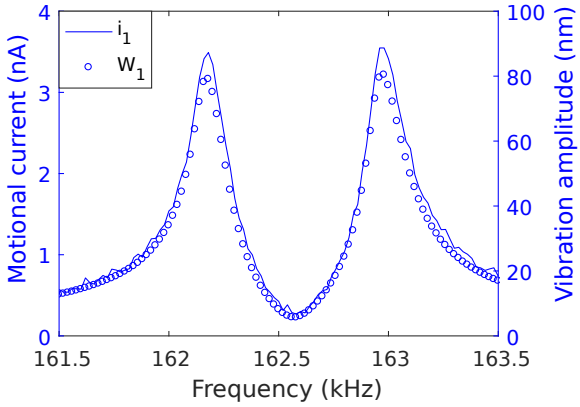

Figure 3.22: Comparison between the motional current i_1 and the vibration W_1 of the short cantilever measured with the LDV

it is also proportional to the vibration. We can also deduce the vibration from the motional current (Appendix A.5), but we have a slight difference after a comparison with the result obtained from the LDV.

Frequency response of the two cantilevers

To obtain the frequency response of the two cantilevers, we put now the laser of the vibrometer on the long cantilever. For the short cantilever, the electrical response with the motional current reflecting its vibration is used. We still consider the previous device, and the results are shown in Figure 3.23. At the balanced state, we notice in Figure 3.23a that there is no more offset between the frequencies at peak amplitude. If we perturb the system with the DC voltage (Figure 3.23b), there is also no offset between the two curves. For the nonlinear case where we have the amplitude jump on each cantilever (Figure 3.23c), the jump also appears at the same frequency. So, with a simultaneous measurement of the amplitudes, the experimental frequency responses are similar to those of the model. It follows that the offset we have obtained previously is due to the fact that the position of the laser spot changes.

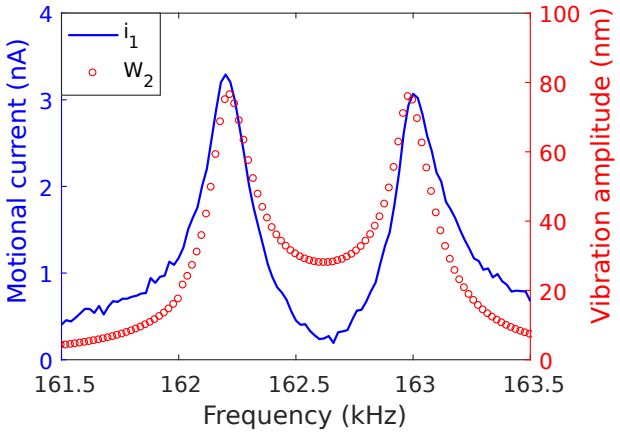

(a) $v_{AC} = 5\,mVrms$ and $V_{DC} = 6.02\,V$

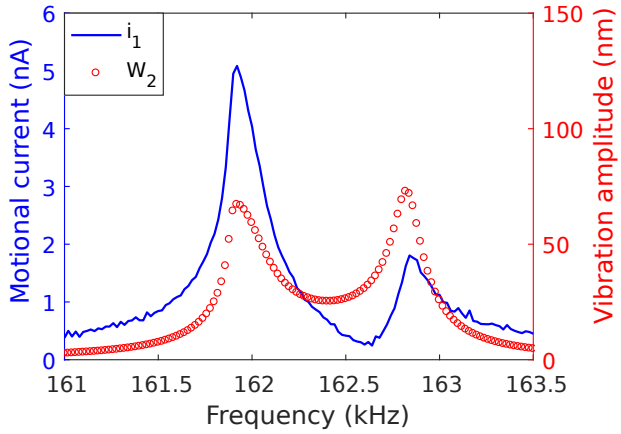

(b) $v_{AC} = 5\,mVrms$ and $V_{DC} = 6.20\,V$

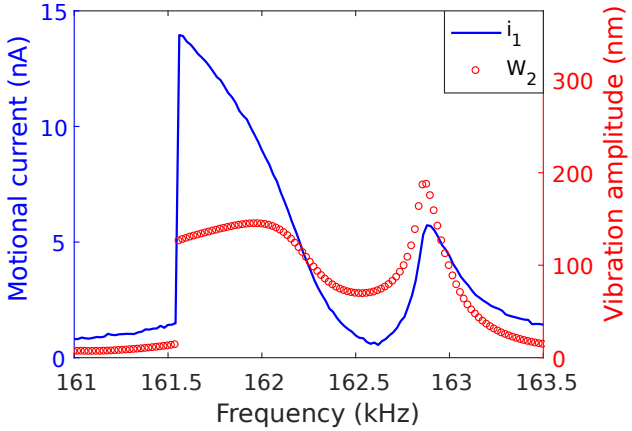

(c) $v_{AC} = 12\,mVrms$ and $V_{DC} = 6.10\,V$ (sweep down)

Figure 3.23: Experimental frequency responses with the simultaneous measurement of the vibration of each cantilever: i_1 is the motional current of the short cantilever and W_2 is the vibration amplitude measured with the LDV at the end of the long cantilever

Effect of the LDV on the device

In order to highlight that the vibrometer perturbs the device, we compare the electrical response of the short cantilever for different positions of the laser spot, and the results are shown in Figure 3.24. After comparison, Figure 3.24 shows that there is a slight difference between the electrical responses of the short cantilever when the laser spot is at its free end or at the free end of the long cantilever. The amplitude change in each mode means that it creates a small perturbation that slightly unbalances the device. If we reproduce these two cases with simulations, we notice that to move from the case where the laser spot is on the long cantilever to the case where it is on the short one, we need to add perturbation not only on one cantilever, but also on both cantilevers at the same time. So, a part of the perturbation due to the position of the laser spot may also affect the entire system.

However, if we compare the case where the laser spot is at the free end of the long cantilever with a case where the laser is turned off, the two electrical responses are almost identical. We can then conclude that the laser does not affect the long cantilever. Since this cantilever is not actuated, one can assume that the perturbation of the vibrometer is related to the electrostatic actuation.

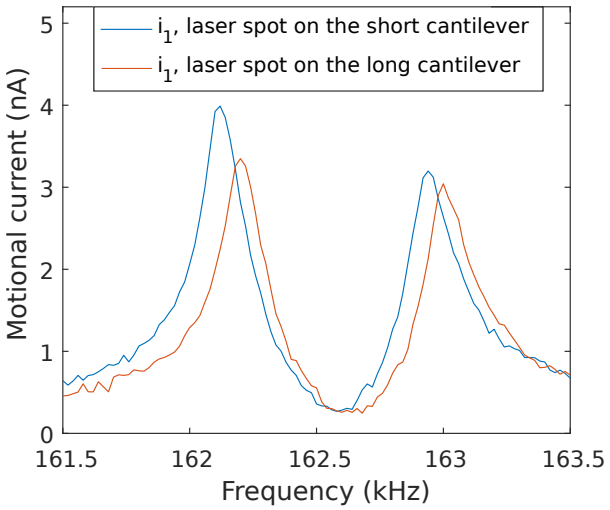

Figure 3.24: Motional current as a function of the position of the laser spot

3.8 Summary

In this chapter, an experimental investigation on the proposed mode localized mass sensor has been conducted. After presenting the fabricated devices, a first study on single cantilevers has been carried out. From this, the Young's modulus and the stiffness of the fixed end of the microbeams have been determined. After that, we have considered the device with coupled cantilevers, and studied its static and dynamic behaviors. We have compared the experimental results with the theoretical results, and the good agreement between them allows us to validate the developed model. At the same time, we have also demonstrated experimentally that the DC voltage can be tuned in order to balance the device, thus allowing to overcome the manufacturing defects. Concerning the mass sensing, the functionalization of electrostatic nonlinearities has been proposed to improve the device sensitivity. Simulations have shown that the sensitivity limitation due to mode aliasing is overcome with a significant improvement of up to 67 %. After experimental measurements, we have also obtained the same improvement, which confirms the simulations. Finally, we have noticed a small offset between the experimental amplitude responses of the two cantilevers. It has been shown that the LDV has an effect which can slightly perturb the device.

The investigation on the proposed mode localized MEMS mass sensor using attractive electrostatic forces ends with this chapter, which allows us to move on to the last chapter of this thesis that concerns the second proposed device using another type of electrostatic actuation.

Chapter 4

The proposed device using repulsive electrostatic forces

Contents

4.1 Introduction

We have seen in Section 1.5.2 that one of the problems of MEMS mass sensors using mode localization is the limitation of the mass resolution due to the minimal detectable amplitude variation. To increase this limitation, the device should have a high dynamic range, and the resonators must be driven at high amplitude. For the device using attractive electrostatic forces, we have demonstrated in Chapter 3 the use of electrostatic nonlinearities in order to improve its sensitivity. But we use high vibration amplitudes to introduce these nonlinearities in the device. So, with this type of actuation, we have already enhanced the dynamic range of the device with the functionalization of electrostatic nonlinearities. However, there is another kind of electrostatic actuation which also allows us to drive resonators at high vibration amplitudes. As we have seen in Section 1.3.3, it uses repulsive electrostatic force which occurs between a fixed and a movable electrode. This actuation can be used for several kinds of device like MEMS actuators [146–148], RF MEMS switch [149] or MEMS mirror [150]. We can have many configurations but the most appropriate for microbeams is the one with out-of-plane repulsive actuator illustrated in Figure 1.8c. It has already been used to actuate MEMS cantilevers [151–153], but its use for mass sensing application with the mode localization has not yet been sufficiently investigated. So, we propose to use it for the coupled cantilevers. As this actuation also shows both softening and hardening effects, we can balance the device by tuning the DC voltage. In this chapter, we first present the second proposed device using repulsive electrostatic forces, and the analytical model which allows us to design it. Then, we proceed to the experimental investigation with the fabricated device. It includes the study of its static and dynamic behavior, in order to validate the analytical model. Finally, we study the dependance between the mass detection and the vibration amplitudes.

4.2 Presentation of the device and evaluation of the intensity of the electrostatic force

4.2.1 Presentation of the device

As shown in Figure 4.1, the second proposed device is also composed of two cantilevers connected by a coupling beam. The only thing that has changed is the electrostatic actuation, which now includes three electrodes: a bottom electrode under the actuated cantilever (Cantilever 1) and two side electrodes located on each side of it.

To generate the vibration, we actuate one of the two cantilevers. For that, we apply a combined AC-DC voltage on the side electrodes while the device and the bottom electrode are grounded.

Concerning the dimensions of the device, those of the cantilevers and the coupling beam remain unchanged. The length of Cantilever 2 which is not actuated is also fixed at $100\,\mu m$ while the length of the other one (Cantilever 1) will be determined later. As we can create both softening and hardening effects, Cantilever 1 can be shorter or longer. The dimensions of the two side electrodes and the bottom

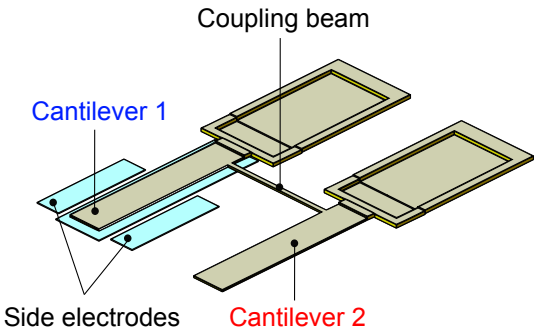

Figure 4.1: The device using repulsive electrostatic forces

electrode have to be reduced so that they do not interact with the cantilever which is not actuated. So, we choose a width of 28 μm for the bottom electrode, and a width of 15 μm for the side electrodes. As the nominal space suggested by the MUMPS® design rule is 3 μm, we choose this value for the distance between each electrode. In order not to interact with the coupling beam, the side electrodes are also placed at 40 μm from the fixed end of the cantilevers. Finally, the dimensions of the device are given in Table 4.1.

Table 4.1: Dimensions of the device using repulsive electrostatic forces

Dimension	Designation	Value
Length of Cantilever 1	L_1	-
Length of Cantilever 2	L_2	100 μm
Width of the cantilevers	b	20 μm
Thickness of the cantilevers	h	1.25 μm
Length of the coupling beam	L_c	65 μm
Width of the coupling beam	b	3 μm
Position of the coupling beam	$\tilde{x}_c$	5 μm
Gap	g	1.00 μm
Width of the bottom electrode	b_b	28 μm
Width of the side electrodes	b_{se}	15 μm
Position of the side electrodes	$\tilde{x}_e$	40 μm
Distance between each electrode	g_e	3 μm

4.2.2 Evaluation of the intensity of the electrostatic force

Before modeling the device, we first need to determine the expression of the electrostatic force. Siyuan et al. [154] have already proposed an analytical model for a two-layer repulsive-force out-of-plane micro electrostatic actuator. As for the attractive electrostatic force, the repulsive force is also proportional to the square of the applied voltage and the derivative of the capacitance with respect to the distance between the bottom electrode and the moving electrode. Due to the complex geometry of this actuation, the expression they have obtained is less simple than that of the actuation using attractive force. But there is also another method which consists in using a FEM model. As it is simpler and more effective, this method will be used to evaluate the intensity of the repulsive electrostatic force.

FEM model of the electrostatic actuation and expression of the electrostatic force

To calculate the electrostatic force, we perform simulations with COMSOL Multiphysics® by using a 2D FEM model that represents the cross section of the device where we have side electrodes. This assumes that all dimensions in the width direction of the cantilever are small compared to those in its length direction. This model also does not take into account the actual distribution of the electrostatic fields along the length direction of the cantilevers. But compared to a 3D model, this allows to reduce the computational time. As shown in Figure 4.2, the model is composed of the two cantilevers, the actuation electrodes and the media surrounding the device. In order to have a symmetric structure, we also add a bottom electrode and side electrodes on Cantilever 2.

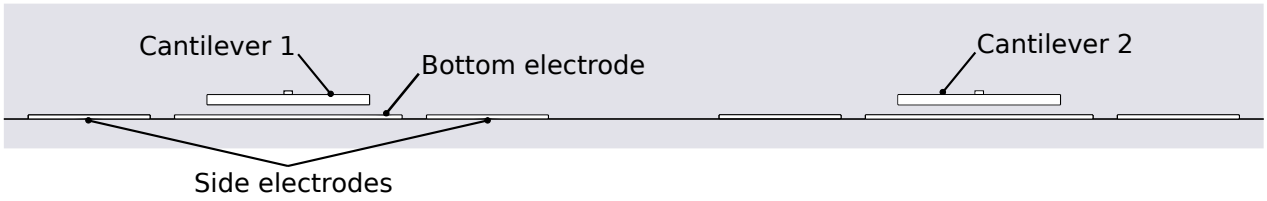

Figure 4.2: 2D FEM model of the device

In the model, the surrounding media has a width of 200 μm and a height of 150 μm, but only the mesh arround the cantilevers and the electrodes are refined. Concerning the distance between each cantilever, it is equal to the length of the coupling beam. To perform the simulation, we apply a DC voltage of 1 V on the two electrodes on each side of Cantilever 1 while Cantilever 2 and the other electrodes are grounded. For the boundary condition, the displacement of the lower line corresponding to the substrate is blocked. As a mechanical condition cannot be applied on electromechanical interfaces, we add a small element above each cantilever in order to block its displacement when the repulsive force will push it up. By calculating the reaction force of this element, we can determine the electrostatic force applied to the cantilever.

Results and expression of the electrostatic force

For a given value of the distance between the cantilever and the bottom electrode, the simulation results are shown in Figure 4.3.

Figure 4.3a shows that the distribution of the electric potential and the electric field lines is influenced by the presence of Cantilever 2 (on the right side) and the electrodes around it. As shown in Figure 4.3b, the deformation of the actuated cantilever is not symmetrical. It means that on Cantilever 1, the applied electrostatic force due to each side electrode is not the same. The reaction force on each element blocking the displacement of the cantilevers shows that there is a small part of the electrostatic force which is applied on Cantilever 2, even if it is not near the actuation electrodes. But this force is not important, its intensity is around 3 % of that of the force applied on Cantilever 1.

For the expression of the electrostatic force, we perform simulations with different values of the distance between Cantilever 1 and the bottom electrode. Distance values in the range 0.3 μm to 3.8 μm are

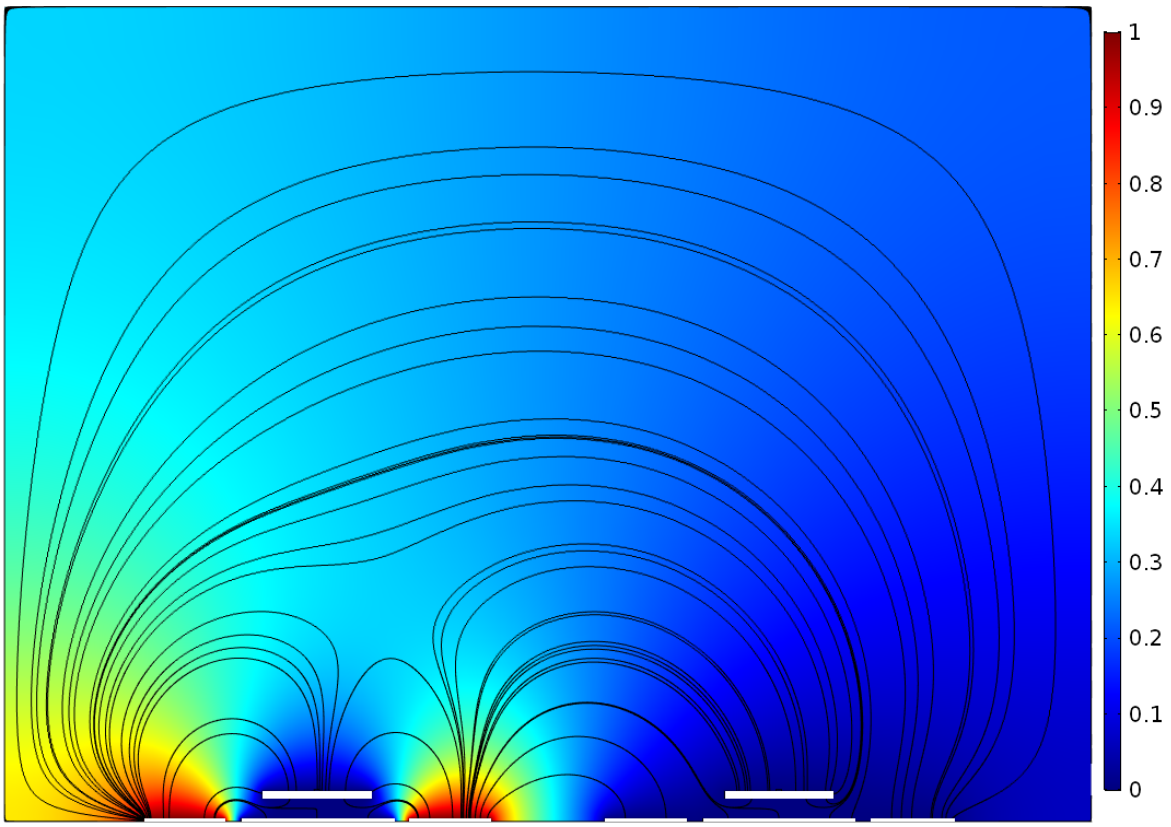

(a) Electric potential and Electric field lines

(b) Deformation (with a scaling factor of $1\,10^{10}$)

Figure 4.3: Simulation results

considered, and we determine the intensity of the electrostatic force for each of them. Once we get the results, we use MATLAB® R2019 to find the coefficients of the third order polynomial that is a best fit for the data obtained. All results are shown in Figure 4.4.

The expression of the third order polynomial P is given by

$$P\left(g+\tilde{w}_1\right) = \tilde{C}_0 + \tilde{C}_1\left(g+\tilde{w}_1\right) + \tilde{C}_2(g+\tilde{w}_1)^2 + \tilde{C}_3(g+\tilde{w}_1)^3 \tag{4.1}$$

where

$$\begin{aligned} \tilde{C}_0 &= 1.80\,10^{-7}\,N/m, \\ \tilde{C}_1 &= 2.84\,10^{-2}\,N/m^2, \\ \tilde{C}_2 &= -1.16\,10^{4}\,N/m^3 \quad \text{and} \\ \tilde{C}_3 &= 8.70\,10^{8}\,N/m^4 \end{aligned} \tag{4.2}$$

If we change the value of the applied DC voltage V, the quotient between the intensity of the electrostatic force and the square of V remains unchanged. So, we can deduce that the elctrostatic force also

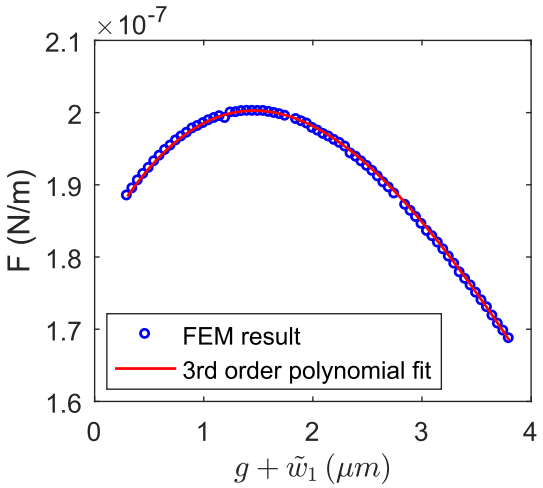

Figure 4.4: Electrostatic force as a function of $g + \tilde{w}_1$ (g is the initial gap and $\tilde{w}_1$ is the displacement of Cantilever 1)

depends on V^2. Thus, the expression of the electrostatic force applied per unit length of the cantilever is given by

$$\tilde{F}_E\left(V, \tilde{w}_1\right) = V^2 \left[\tilde{C}_0 + \tilde{C}_1\left(g + \tilde{w}_1\right) + \tilde{C}_2(g + \tilde{w}_1)^2 + \tilde{C}_3(g + \tilde{w}_1)^3\right] \tag{4.3}$$

where

$$\begin{aligned} \tilde{C}_0 &= 1.80\,10^{-7}\,N/m/V^2, \\ \tilde{C}_1 &= 2.84\,10^{-2}\,N/m^2/V^2, \\ \tilde{C}_2 &= -1.16\,10^{4}\,N/m^3/V^2 \quad \text{and} \\ \tilde{C}_3 &= 8.70\,10^{8}\,N/m^4/V^2 \end{aligned} \tag{4.4}$$

Comparison with the attractive electrostatic force

To compare the repulsive electrostatic force with the attractive one, we plot in the same figure the variation of their intensity as a function of $g+\tilde{w}_1$. The applied voltage for the repulsive force is equal to $1\,V$ while for the attractive force, we set it in order to have the same force when the distance between the cantilever and the bottom electrode is equal to the initial gap ($1\,\mu m$). We choose this out-of-plane position of the cantilever because it gives us an approximate value of the harmonic load when the device is actuated. The results are shown in Figure 4.5.

We notice in Figure 4.5 that to have the same electrostatic force for $g + \tilde{w}_1 = 1\,\mu m$, we have to use a voltage of $45\,mV$ for the actuation using attractive force. It means that in order to have the same vibration amplitude, the actuation using repulsive force requires the use of voltages that are almost twenty times higher. Concerning the variation of the intensity of the force as a function of the out-of-plane position of the cantilever, we notice that unlike the attractive force, the repulsive force is almost constant. Consequently, the softening or the hardening effects of this actuation are less important. Another consequence is that we no longer have electrostatic nonlinearities. As the other repulsive forces that depend on the displacement of the cantilever are negligible, the vibration of the device

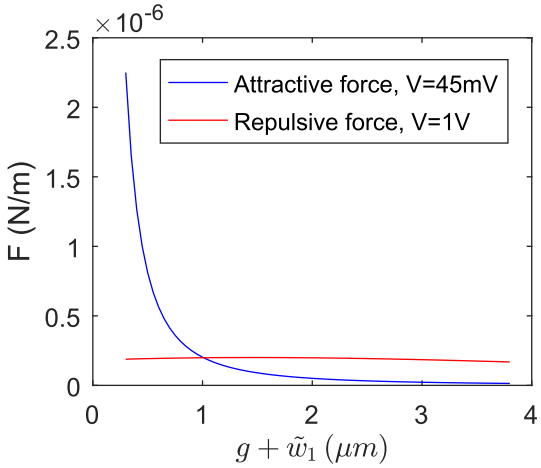

Figure 4.5: Comparison between the actuation using attractive and repulsive electrostatic forces

remains linear regardless of its amplitudes. Thus, we can increase the dynamic range of the device without having the effects of electrostatic nonlinearities.

4.3 Modeling of the device

After determining the expression of the repulsive electrostatic force, we present in this section the analytical model of the device.

4.3.1 Equation governing the bending vibration of the device

Assuming that the electrostatic force is only applied where we have side electrodes, the bending vibration of the device shown in Figure 4.1 is given by

$$\begin{cases} EI\tilde{w}_1'''' + (\rho bh + \tilde{m}\delta(\tilde{x}-\tilde{x}_m))\,\ddot{\tilde{w}}_1 + \tilde{c}_1\dot{\tilde{w}}_1 - \tilde{k}_r\left(\tilde{w}_1'(\tilde{x}_c) - \tilde{w}_2'(\tilde{x}_c)\right)\delta'(\tilde{x}-\tilde{x}_c) \\ = H(\tilde{x}-\tilde{x}_e)\left(V_{DC} + v_{AC}\cos\left(\tilde{\Omega}\tilde{t}\right)\right)^2\left[\tilde{C}_0 + \tilde{C}_1(g+\tilde{w}_1) + \tilde{C}_2(g+\tilde{w}_1)^2 + \tilde{C}_3(g+\tilde{w}_1)^3\right] \\ EI\tilde{w}_2'''' + \rho bh\ddot{\tilde{w}}_2 + \tilde{c}_2\dot{\tilde{w}}_2 - \tilde{k}_r\left(\tilde{w}_2'(\tilde{x}_c) - \tilde{w}_1'(\tilde{x}_c)\right)\delta'(\tilde{x}-\tilde{x}_c) = 0.03\,\tilde{F}_E \end{cases} \tag{4.5}$$

where H is the Heaviside function, and $\tilde{F}_E$ is equal to the force applied to Cantilever 1. By using the same non dimensional parameters w, m, c, k_r, x and t, Equation (4.5) becomes

$$\begin{cases} w_1'''' + (1 + m\delta(x-x_m))\,\ddot{w}_1 + c_1\dot{w}_1 - k_r\left(w_1'(x_c) - w_2'(x_c)\right)\delta'(x-x_c) \\ = \dfrac{{L_1}^4}{EIg}H(x-x_e)\left(V_{DC} + v_{AC}\cos(\Omega t)\right)^2 * \left[\tilde{C}_0 + g\tilde{C}_1(1+w_1) + g^2\tilde{C}_2(1+w_1)^2 + g^3\tilde{C}_3(1+w_1)^3\right] \\ w_2'''' + \ddot{w}_2 + c_2\dot{w}_2 - k_r\left(w_2'(x_c) - w_1'(x_c)\right)\delta'(x-x_c) = \dfrac{{L_1}^4}{EIg}0.03\,\tilde{F}_E \end{cases} \tag{4.6}$$

By setting

$$\begin{gathered} C_0 = \frac{{L_1}^4}{EIg}\left(\tilde{C}_0 + \tilde{C}_1 g + \tilde{C}_2 g^2 + \tilde{C}_3 g^3\right) \;\; ; \;\; C_1 = \frac{{L_1}^4}{EIg}\left(\tilde{C}_1 g + 2\tilde{C}_2 g^2 + 3\tilde{C}_3 g^3\right) \;\; ; \\ C_2 = \frac{{L_1}^4}{EIg}\left(\tilde{C}_2 g^2 + 3\tilde{C}_3 g^3\right) \;\; ; \;\; C_3 = \frac{{L_1}^4}{EIg}\tilde{C}_3 g^3 \;\text{ and }\; F_E = \frac{{L_1}^4}{EIg}\tilde{F}_E \end{gathered} \tag{4.7}$$

Equation (4.6) becomes

$$\begin{cases} w_1'''' + \left(1 + m\delta\left(x - x_m\right)\right)\ddot{w}_1 + c_1\dot{w}_1 - k_r\left(w_1'\left(x_c\right) - w_2'\left(x_c\right)\right)\delta'\left(x - x_c\right) \\ \quad = H\left(x - x_e\right)\left(V_{DC} + v_{AC}\cos\left(\Omega t\right)\right)^2 * \left(C_0 + C_1 w_1 + C_2 {w_1}^2 + C_3 {w_1}^3\right) \\ \\ w_2'''' + \ddot{w}_2 + c_2\dot{w}_2 - k_r\left(w_2'\left(x_c\right) - w_1'\left(x_c\right)\right)\delta'\left(x - x_c\right) = 0.03\, F_E \end{cases} \tag{4.8}$$

4.3.2 Static and dynamic deflection

To solve Equation (4.8), we also use one mode Galerkin discretization approach like for the model of the device using attractive electrostatic forces. So, the total deflection of each cantilever can also be expressed by

$$w_1\left(x,t\right) = \left(a_{1s} + a_1\left(t\right)\right) * \phi_1\left(x\right) \quad \text{and} \quad w_2\left(x,t\right) = \left(a_{2s} + a_2\left(t\right)\right) * \phi_2\left(x\right) \tag{4.9}$$

Static deflection

For the static deflection, we drop all time varying terms in Equation (4.8), multiply respectively the first and the second equations by $\phi_1(x)$ and $\phi_2(x)$, and integrate them respectively from $x = 0$ to $x = 1$ and from $x = 0$ to $x = L_2/L_1$. As the electrostatic force applied to Cantilever 2 is not very important, we can first neglect it. By considering the following integrals

$$\begin{gathered} \int_0^1 H\left(x - x_e\right)\phi_1\left(x\right)dx = \int_{x_e}^1 \phi_1\left(x\right)dx \approx 0.719\,; \int_0^1 H\left(x - x_e\right){\phi_1}^2\left(x\right)dx = \int_{x_e}^1 {\phi_1}^2\left(x\right)dx \approx 0.98\,; \\ \int_0^1 H\left(x - x_e\right){\phi_1}^3\left(x\right)dx = \int_{x_e}^1 {\phi_1}^3\left(x\right)dx \approx 1.46\,; \int_0^1 H\left(x - x_e\right){\phi_1}^4\left(x\right)dx = \int_{x_e}^1 {\phi_1}^4\left(x\right)dx \approx 2.31 \end{gathered} \tag{4.10}$$

we finally obtain

$$\begin{cases} {\lambda_1}^4\phi_1\left(x\right) + k_r\left(a_{1s}\phi_1'^2\left(x_c\right) - a_{2s}\phi_1'\left(x_c\right)\phi_2'\left(x_c\right)\right) \\ \quad = {V_{DC}}^2\left(0.719\, C_0 + 0.98\, C_1\, a_{1s} + 1.46\, C_2\, {a_{1s}}^2 + 2.31\, C_3\, {a_{1s}}^3\right) \\ \\ {\lambda_2}^4\dfrac{{L_1}^4}{{L_2}^4} + k_r\left(a_{2s}\phi_2'^2\left(x_c\right) - a_{1s}\phi_1'\left(x_c\right)\phi_2'\left(x_c\right)\right) = 0 \end{cases} \tag{4.11}$$

By using MATLAB® R2019, we can solve Equation (4.11) and determine the static deflection at the end of each cantilever.

Dynamic deflection

For the dynamic deflection, we replace the expressions of w_1 and w_2 by those given in Equation (4.9). We then discretize the equation like for the static deflection. We assume that the AC voltage is always low compared to the DC voltage, so we can drop all terms with ${v_{AC}}^2$. As we have seen in Figure 4.5, the repulsive force is almost constant compared to the attractive one, so we can also neglect all electrostatic nonlinearities and keep only the harmonic load. Finally, we obtain the matrix equation below

$$\left[\ M\ \right]\begin{bmatrix}\ddot{a}_1\\ \ddot{a}_2\end{bmatrix}+\left[\ C\ \right]\begin{bmatrix}\dot{a}_1\\ \dot{a}_2\end{bmatrix}+\left[\ K\ \right]\begin{bmatrix}a_1\\ a_2\end{bmatrix}=\left[\ F\ \right]*\cos\left(\Omega t\right) \tag{4.12}$$

where

$$\begin{gathered}\left[\ M\ \right]=\begin{bmatrix}1+m\phi_1^2\left(x_m\right) & 0\\ 0 & 1\end{bmatrix};\ \left[\ C\ \right]=\begin{bmatrix}c_1 & 0\\ 0 & c_2\end{bmatrix};\\ \left[\ K\ \right]=\begin{bmatrix}{\lambda_1}^4-{V_{DC}}^2\left(0.98\,C_1+2.92\,C_2\,a_{1s}+6.94\,C_3\,{a_{1s}}^2\right)+k_r{\phi_1'}^2\left(x_c\right) & -k_r\phi_1'\left(x_c\right)\phi_2'\left(x_c\right)\\ -k_r\phi_1'\left(x_c\right)\phi_2'\left(x_c\right) & {\lambda_2}^4\frac{{L_1}^4}{{L_2}^4}+k_r{\phi_2'}^2\left(x_c\right)\end{bmatrix};\\ \left[\ F\ \right]=\begin{bmatrix}v_{AC}V_{DC}\left(1.44\,C_0+1.96\,C_1\,a_{1s}+2.92\,C_2\,{a_{1s}}^2+4.63\,C_3\,{a_{1s}}^3\right)\\ 0.03\,v_{AC}V_{DC}\left(1.44\,C_0+1.96\,C_1\,a_{1s}+2.92\,C_2\,{a_{1s}}^2+4.63\,C_3\,{a_{1s}}^3\right)\end{bmatrix}\end{gathered} \tag{4.13}$$

The amplitudes of a_1 and a_2 are given by

$$\begin{bmatrix}A_1\\ A_2\end{bmatrix}=\begin{bmatrix}\left|\tilde{A}_1\right|\\ \left|\tilde{A}_2\right|\end{bmatrix} \tag{4.14}$$

where

$$\begin{bmatrix}\tilde{A}_1\\ \tilde{A}_2\end{bmatrix}=\left(-\Omega^2\left[\ M\ \right]+j\Omega\left[\ C\ \right]+\left[\ K\ \right]\right)^{-1}*\left[\ F\ \right]\quad\text{and}\quad j^2=-1 \tag{4.15}$$

Finally, the vibration amplitudes at the end of Cantilever 1 and Cantilever 2 are given by

$$W_1=A_1*\phi_1\left(1\right)*g\quad\text{and}\quad W_2=A_2*\phi_2\left(\frac{L_2}{L_1}\right)*g \tag{4.16}$$

We notice in the rigidity matrix K in Equation (4.13) the term $-{V_{DC}}^2\left(0.98\,C_1+2.92\,C_2\,a_{1s}+6.94\,C_3\,{a_{1s}}^2\right)$ which modifies the effective stiffness of the actuated cantilever. As this term can be positive or negative, we can have softening or hardening effects, depending on the applied voltage.

4.3.3 Amplitude response at the balanced state and length of Cantilever 1

Amplitude response at the balanced state

For the device using attractive electrostatic forces, we have seen that when only one of the two cantilevers is actuated, the amplitude ratio of each mode at the balanced state is equal to one. We also notice that the amplitude of each mode are identical because their frequencies are almost the same. But if the second resonator is also actuated, the amplitude response at the balanced state will slightly change. The amplitude ratio should remain unchanged, but the amplitude of each mode will no longer be the same. Indeed, if we apply on Cantilever 2 3 % of the force applied to Cantilever 1, the vibration amplitude of the symmetric mode will be increased by 3 % because the vibrations are in phase. For the vibration amplitude of the antisymmetric mode, it will be decreased by 3 % because the vibrations are out of phase. Thus, the ratio between the amplitudes of the symmetric and the antisymmetric modes should be equal to 1.06. To highlight this, we have in Figure 4.6 the amplitude response of a system with two weakly coupled identical resonators. On Resonator 1, we apply a force equal to 1 while on Resonator 2, we apply a force equal to 0.03.

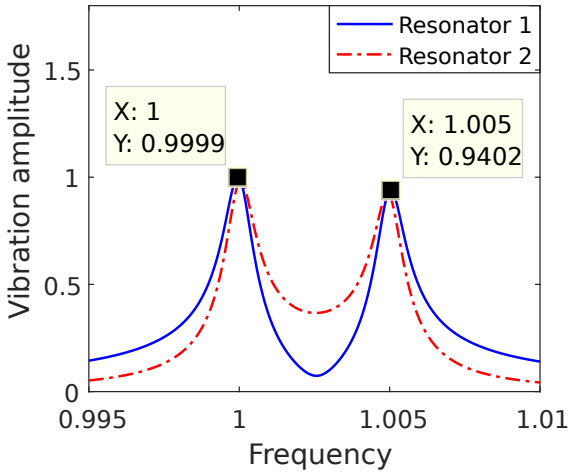

Figure 4.6: Amplitude response of a system with two weakly coupled identical resonators when the forces applied to Resonator 1 and Resonator 2 are respectively equal to 1 and 0.03

We notice in Figure 4.6 that the amplitude ratio of each mode is still equal to 1. But as predicted previously, the amplitudes of the symmetric mode is 6 % higher than those of the antisymmetric mode due to the actuation of the second resonator. However, the difference between the amplitude response of this system and that of a system with only one resonator actuated is not important. As we use the amplitude ratio of one mode as output metric, this will not affect the mass detection.

Length of Cantilever 1

In order to choose the length of Cantilever 1, we perform simulations with several values of L_1. For each value, we determine the DC voltage which gives us an amplitude response similar to the one shown in Figure 4.6. As the device using repulsive electrostatic forces is fabricated with the same

process, the parameters used for the model are similar to those used for the model of the device with attractive force. The result is then shown in Figure 4.7.

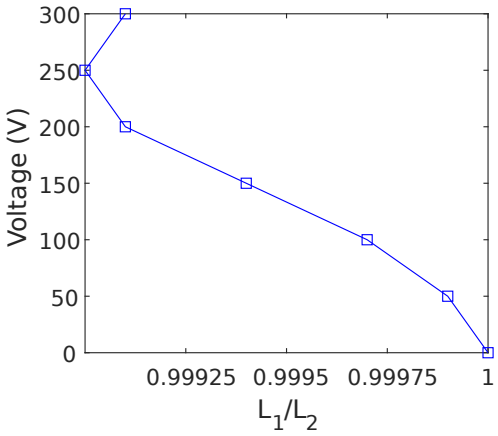

Figure 4.7: DC balancing voltage as a function of the length ratio between the two cantilevers

We notice in Figure 4.7 that Cantilever 1 is always shorter than Cantilever 2. So, we still have a softening effect with this chosen voltage range. But the length ratio L_1/L_2 increases from a DC voltage of $250\,V$. It is due to the fact that we can have a hardening effect for higher voltages. Concerning the length difference between each cantilever, we notice that it is not important even if the applied DC voltage is very high. It is due to the softening effect of this actuation which is very weak compared to the one using an attractive electrostatic force. We cannot apply too high DC voltages, so we have to choose a length ratio within the range given in Figure 4.7. But as we do not have enough precision to manufacture two cantilevers with such a length difference, we propose to use two cantilevers with the same length. Due to the manufacturing defects, these two cantilevers will never have the same dimension. Since we have actuating electrodes on both cantilevers, we will always be able to balance the system, even without knowing which cantilever is stiffer.

4.4 The fabricated device

Like for the devices using attractive electrostatic forces, those with repulsive electrostatic forces were manufactured with the MUMPS® process (Run #128). As shown in Figure 4.8, the cantilevers of the device are made with the layer Poly2, and we have a second reinforcement layer Poly1 at the fixed end. For the bottom and the side electrodes, we still use the layer Poly0.
The fabricated device is shown in Figure 4.9. We recall that the two cantilevers have the same length, and the other dimensions of the device are already given in Table 4.1.
For this device, we also have three pads. Two of them are connected to the side electrodes around each cantilever, and the last one is connected to the cantilevers and the bottom electrodes.

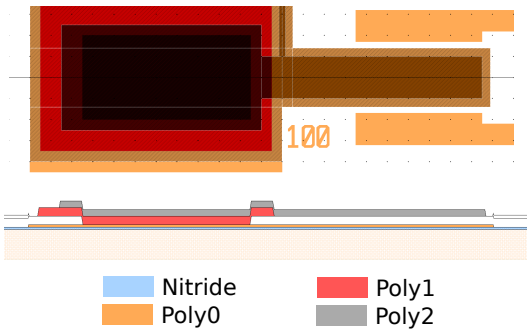

Figure 4.8: Top view and cross section of a cantilever

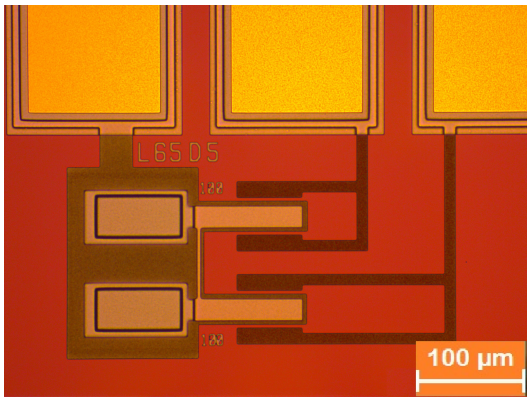

Figure 4.9: Optical microscope image of the device using repulsive electrostatic forces

4.5 Static deflection

To validate the analytical model, we perform experiments to study the static behavior of the device, and the experimental and theoretical results are then compared.

4.5.1 Experimental setup

For the experimental setup, we still use an optical interferometer to measure the deflection of the cantilevers. A DC voltage is applied on the side electrodes of one cantilever (Cantilever 1), and the rest is grounded. After measurements, the topography of the device and the profile of each cantilever are shown in Figure 4.10.

We notice in Figure 4.10b that unlike the short cantilever of the device using attractive electrostatic forces, the actuated cantilever of the device with repulsive electrostatic force is pushed up when the applied DC voltage increases. As the coupling is weak, the static deflection of the non-actuated cantilever (Cantilever 2) is low.

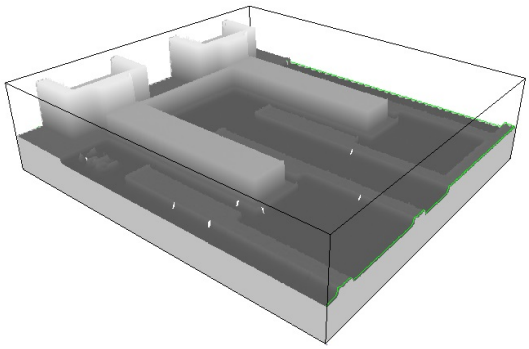

(a) Topography of the device using repulsive electrostatic forces

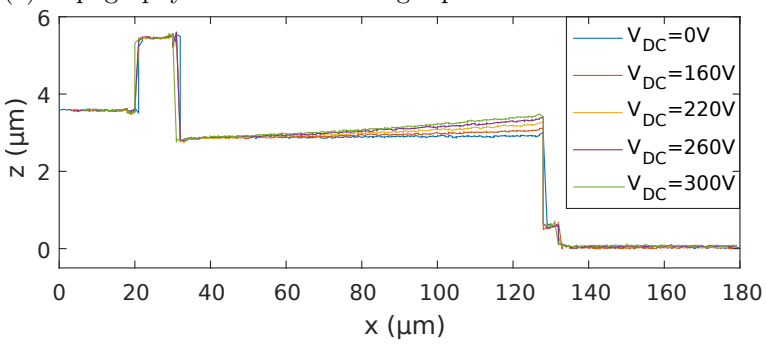

(b) Profile of the actuated cantilever (Cantilever 1)

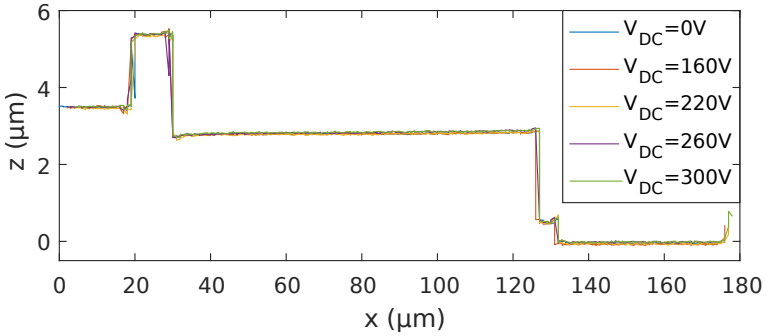

(c) Profile of the non-actuated cantilever (Cantilever 2)

Figure 4.10: Topography of the device using repulsive electrostatic forces and profile of each cantilever (the fixed end is on the left side)

4.5.2 Comparison between experimental and theoretical results

From the profile measured with the optical interferometer, we determine the deflection at the end of each cantilever, and compare it with the theoretical deflection given by the analytical model. A DC voltage in the range $0\,V$ to $300\,V$ is considered, and the results are shown in Figure 4.11.

The comparison shows that we have good agreement between experimental and theoretical results, even if the theoretical static deflections are slightly lower than those given by the experiment. For a DC voltage of $300\,V$, the static deflection of the actuated cantilever is around $450\,nm$, while with the device using attractive electrostatic forces, we get this deflection using just a DC voltage around $15\,V$.

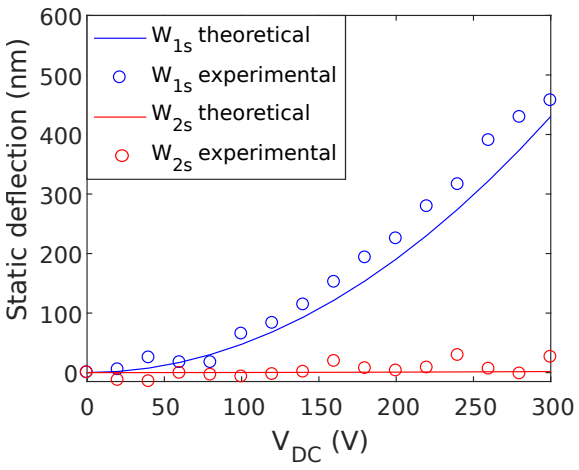

Figure 4.11: Static deflection of each cantilever as a function of the applied DC voltage

4.6 Dynamic response

After studying the static behavior of the device, we study its dynamic behavior by actuating one of the two cantilevers with a combined AC-DC voltage. To validate the analytical model, we then compare the theoretical and the experimental dynamic responses of the device.

4.6.1 Experimental setup

The experimental setup is similar to that of the device using attractive electrostatic forces. As illustrated in Figure 4.12, the device is placed in a vacuum chamber, and we use the LDV to measure the vibration amplitude at the end of each cantilever. We still have the Picoscope® which supplies the AC voltage and collects the data from the LDV, and the DC voltage is supplied by a generator. As the actuation voltage that we use is more important, it is first amplified with a signal amplifier (Tabor, model 9400). It is then applied on the side electrodes of one of the two cantilevers. The other side electrodes, the bottom electrodes and the cantilevers are always grounded.

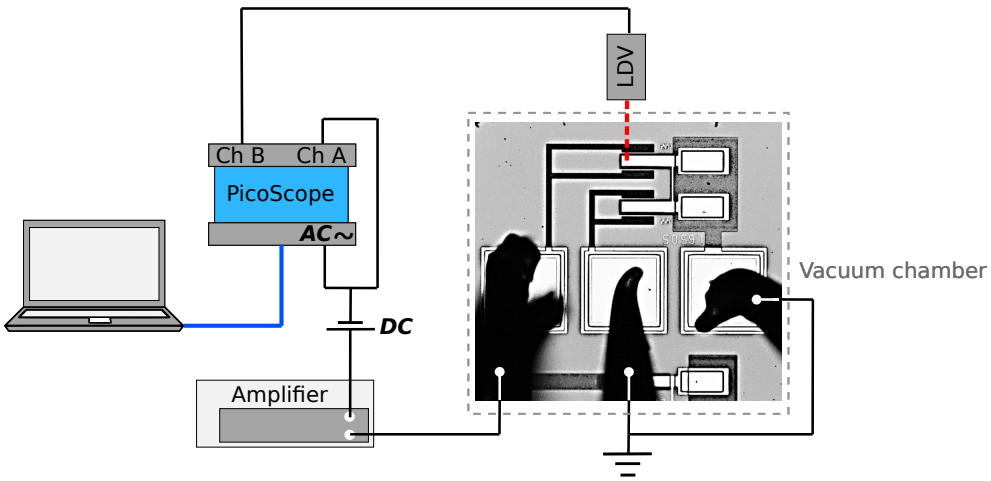

Figure 4.12: Experimental setup for the frequency responses of the device using repulsive electrostatic forces

4.6.2 Frequency response of the device

Frequency response at the veering point

In order to find the DC balancing voltage of the device, we must first find which cantilever should be actuated. As the electrostatic actuation creates a softening effect, we have to find which of the two cantilevers is the stiffest. To achieve this, we arbitrarily choose one cantilever and actuate it by using a small DC voltage. If it vibrates more in the first mode (with the lowest frequency), it means that the chosen cantilever is the softest, and we have to actuate the other one. If we now actuate the stiffest beam, it should vibrate more in the second mode (with the highest frequency). Then, we gradually increase the DC voltage until we have an amplitude response similar to the one shown in Figure 4.6, i.e. an amplitude response with an amplitude ratio equal to one on each mode.
For the theoretical amplitude response, we use the analytical model with some parameters obtained from the experimentation. The first parameter is the quality factor that is measured experimentally by using the half-power bandwidth method. The second parameter is the ratio between the lengths of each cantilever. To find this parameter, we perform simulations by using the DC balancing voltage that we experimentally obtained. The length of the non-actuated cantilever is fixed at $L_2 = 100\,\mu m$ while the length of the one that is actuated is chosen so that the theoretical amplitude response is similar to that of a balanced system. And the last parameter is the stiffness of the rotational spring modeling the fixed end of the cantilevers. We adjust it so that the theoretical and experimental frequencies of the symmetric mode are identical. Finally, the identified parameters are given in Table 4.2 for a chosen device.

Table 4.2: Parameters used for the model

Parameter	Value
Q	900 ($p \approx 0.25\,mbar$)
$\tilde{k}_e$	$3.53\,10^{-7}\,Nm/rad$
L_1	$99.96\,\mu m$

Due to a lower pressure inside the vacuum chamber (around $0.25\,mbar$), the measured quality factor in Table 4.2 is higher than that of the device using attractive electrostatic forces. Concerning the identified length of the actuated cantilever, we obtain it by using the experimental DC balancing voltage that is equal to $110\,V$. We notice that the actuated cantilever is just slightly shorter than the non-actuated one. By using these parameters for the model, the theoretical and experimental frequency responses of the chosen device are shown in Figure 4.13.
After comparison, we notice in Figures 4.13a and 4.13b that we have a good agreement between the results. For each result, the ratio between the amplitude of the actuated and the non-actuated cantilever is equal to one on each mode. But the ratio between the vibration amplitudes of the same cantilever on the two modes is not the same. For the theoretical amplitude response, the ratio between the amplitudes of the symmetric and the antisymmetric modes is equal to 1.06, because we have 3 %

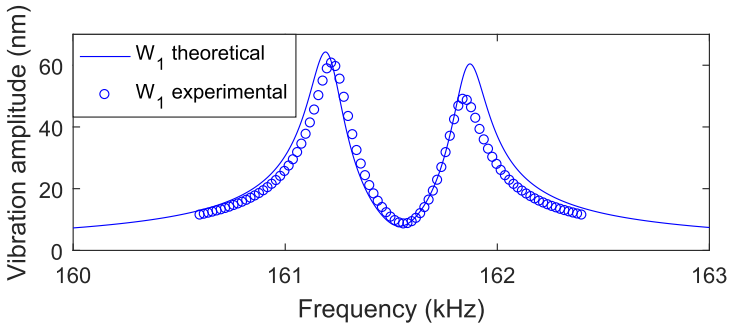

(a) Actuated cantilever (Cantilever 1)

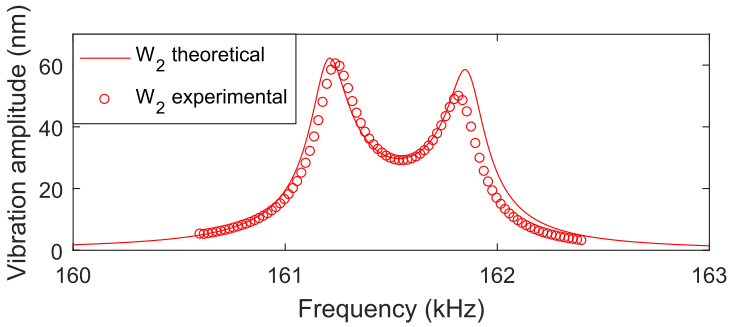

(b) Non-actuated cantilever (Cantilever 2)

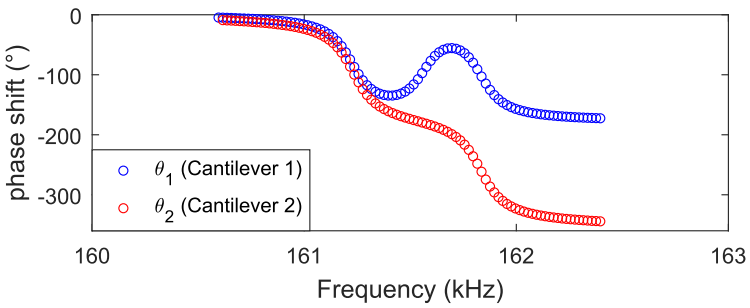

(c) Experimental phase response

Figure 4.13: Theoretical and experimental frequency responses of the device at the balanced state ($v_{AC} = 125\,mV$ and $V_{DC} = 110\,V$)

of the electrostatic force which is applied to the non-actuated cantilever. But for the experimental amplitude response, we have a ratio around 1.20. It means that the electrostatic force applied to Cantilever 2 is around 10 % of that applied to Cantilever 1. This difference may be due to the fact that our approach is based on a 2D FEM model which assumes that the lengths of the electrode and the microbeams are negligible compared to their widths. With this assumption, the electrostatic force is only applied where we have the side electrodes, but that is not exactly the case. Concerning the phase response of each cantilever in Figure 4.13c, we still have the same phase shift for the symmetric mode, reflecting the in-phase vibrations. For the antisymmetric mode, we have a difference of 180° between the phases of the two cantilevers, which reflects the out of phase vibration.

By considering other devices, we obtain different values of the DC balancing voltage, but they do not exceed $110\,V$.

Frequency response with other DC voltages

In order to show that the electrostatic actuation creates a softening effect, we plot the experimental and theoretical amplitude responses of the device by using DC voltages lower and higher than the DC balancing voltage. With DC voltages of $75\,V$ and $145\,V$, the results are shown in Figure 4.14.

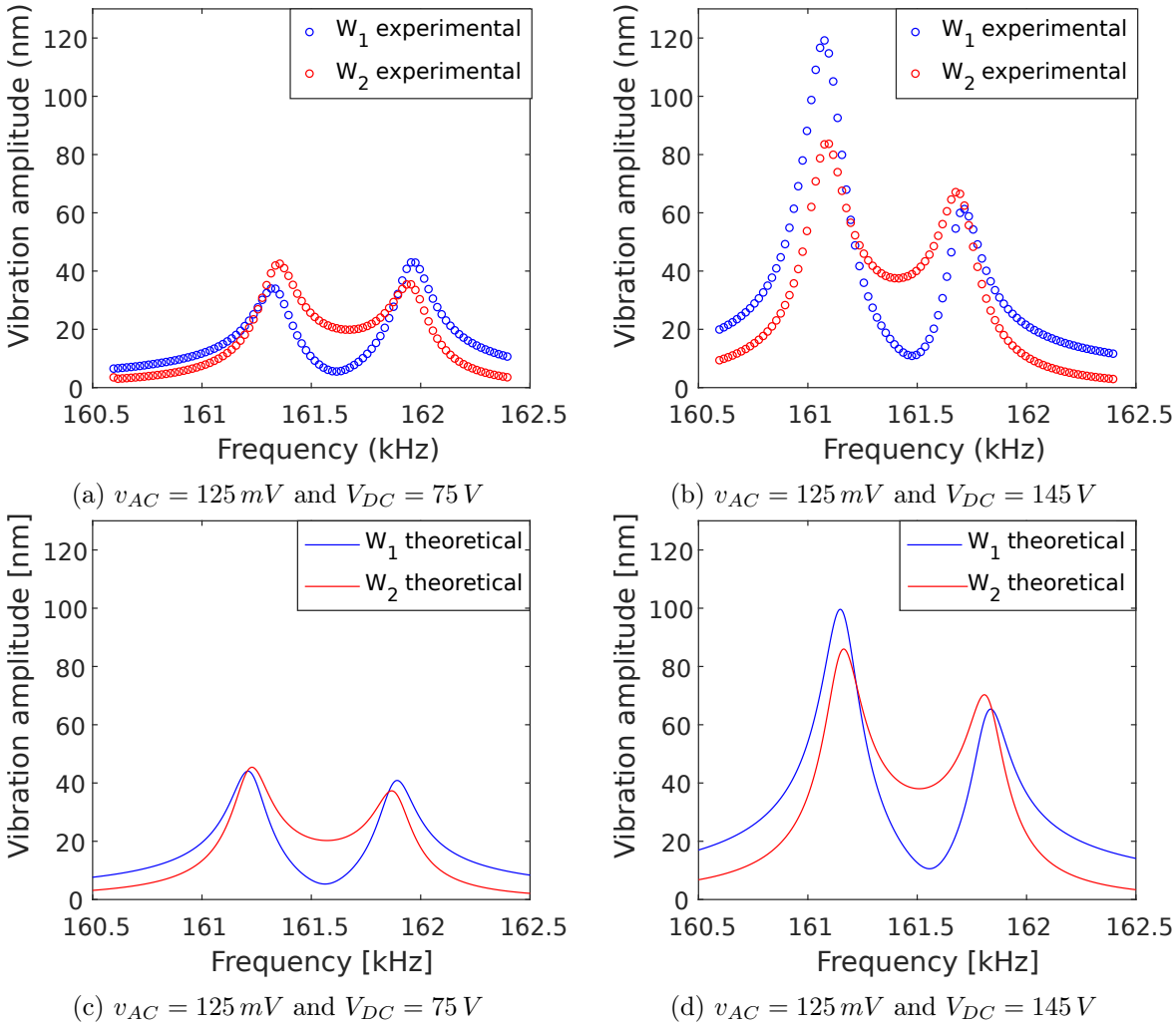

(a) $v_{AC} = 125\,mV$ and $V_{DC} = 75\,V$

(b) $v_{AC} = 125\,mV$ and $V_{DC} = 145\,V$

(c) $v_{AC} = 125\,mV$ and $V_{DC} = 75\,V$

(d) $v_{AC} = 125\,mV$ and $V_{DC} = 145\,V$

Figure 4.14: Experimental and theoretical amplitude responses of the device with other DC voltages

With a DC voltage of $75\,V$ (Figure 4.14a), the effective stiffness of the actuated cantilever is still greater than that of the non-actuated cantilever. So, it vibrates more in the second mode having a higher frequency. If we apply a DC voltage of $145\,V$ (Figure 4.14b), the effective stiffness of the actuated cantilever becomes lower and it vibrate more in the first mode. The same phenomenon has been observed with the device using attractive electrostatic forces, and this confirms that we have a softening effect. However, if we compare the theoretical and experimental amplitude responses, there is a slight difference. In the first case where $V_{DC} = 75\,V$, the experimental and theoretical curves are almost identical. But in the second case where $V_{DC} = 145\,V$, the first mode of the experimental amplitude response shows a more localized vibration. The actual softening effect of the electrostatic actuation is then more important than that predicted. Consequently, the difference between the lengths

of the two cantilevers may be more important than that identified with the model (in Table 4.2). Of course, we just assume that only the lengths of the two cantilevers are different, and the initial disorder is due to this length difference. But in reality, all the dimensions of the cantilevers can be concerned by manufacturing defects.

We also notice in Figure 4.14 that we no longer have a shift between the frequencies at peak amplitudes, even if the LDV is used. For the device using attractive force, we said previously that the laser spot may modify the electrostatic softening effects because only the actuated cantilever is affected by it. But for the device using repulsive force, the electrostatic softening effects are very weak despite the importance of the actuation voltage used. Thus, the device is less sensitive to the perturbation that the laser creates.

Linear dynamic range of the device

We said previously that as the intensity of the electrostatic force is less dependent on the out-of-plane position of the cantilever, we should no longer have electrostatic nonlinearities. In order to verify it experimentally, we plot the amplitude response of the device by using low and high AC voltages, and the result is shown in Figure 4.15.

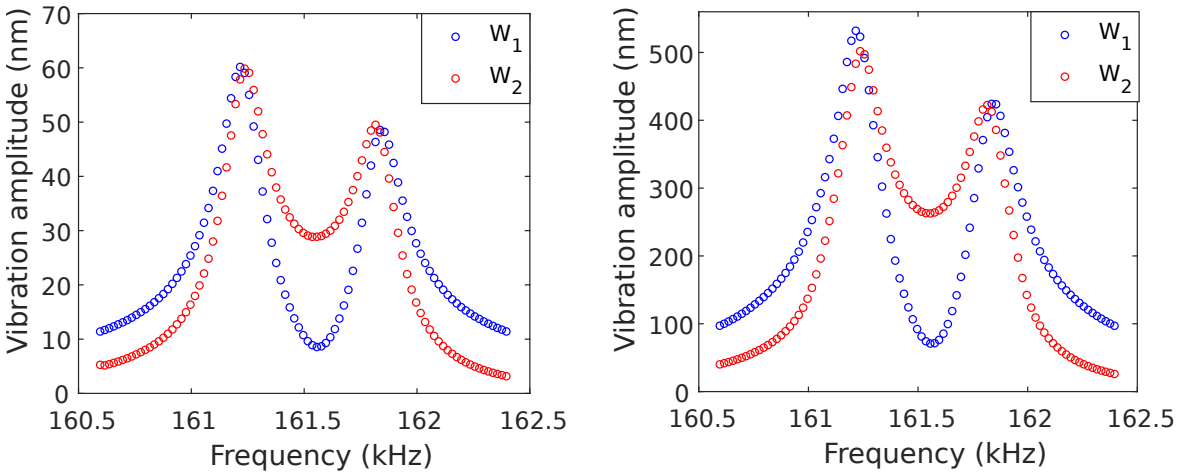

(a) $v_{AC} = 125\,mV$ and $V_{DC} = 110\,V$ (b) $v_{AC} = 1\,V$ and $V_{DC} = 110\,V$

Figure 4.15: Experimental amplitude response of the device with low and high vibration amplitudes

We notice that whether with low or high vibration amplitudes, the curves of the amplitude response are similar. With a high AC voltage involving high vibration amplitudes, the curve is still straight and no softening behavior is observed. As a reminder, the effects of electrostatic nonlinearities with the device using attractive forces appear as soon as the vibration amplitudes exceed 10 % of the gap. In Figure 4.15b, the response is still linear while we are already around 50 % of the gap. To ensure that we really have a linear behavior, we plot the vibration amplitude of the symmetric mode as a function of the AC voltage used. We then compare the result with that given by the model, and they are shown in Figure 4.16.

We notice that for the theoretical results, the amplitude is a linear function of the AC voltage. This

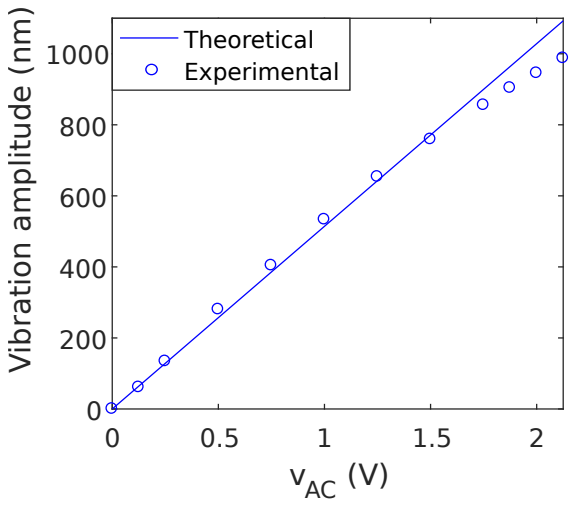

Figure 4.16: Vibration amplitude of the symmetric mode as a function of the applied AC voltage

is to be expected since we have a linear model. But for the experimental result, the linear range does not go beyond a vibration amplitude around $700\,nm$ that represents $70\,\%$ of the gap. After this limit, the amplitude is no longer linearly dependent on the AC voltage. This cannot be due to geometric nonlinearities because the experimental frequency response does not show hardening behavior. The mechanical critical amplitude [26] is equal to $21\,\mu m$, which is very large compared to what we have. The only possible cause of this result is the increase in the damping force. As the vibration amplitude increases, the cantilever moves closer to the lower electrode. This may increase the damping force, and decrease slightly the ratio between the amplitude and the AC voltage. When we add a mass perturbation on the device, one cantilever vibrates at high amplitude, and the other vibrates at low amplitude. But only the one with a large vibration amplitude will be affected by this increase in damping. Consequently, the amplitude ratio will be modified, as well as the identified mass. To ensure proper operation of the sensor, this amplitude limit must not be exceeded. When the device has a localized vibration due to a mass perturbation, the vibration amplitude of the actuated cantilever never exceeds twice its vibration amplitude at the balanced state. So, the initial device should be driven with a vibration amplitude equal to half of the maximum value of the linear range.

4.7 Influence of vibration amplitudes on the mass detection

In order to show how the dynamic range of the device affects the mass detection, we perform a theoretical study in order to investigate the effects of the vibration amplitudes on the measured amplitude ratio and the identified mass perturbation. To achieve this, we consider two cases where the device is driven at low and high vibration amplitudes. In the first case, the vibration amplitude of each mode at the balanced state is equal to $50\,nm$ while in the second case, it is equal to $350\,nm$. We then perform simulations by adding at the end of the actuated cantilever a mass in the range $0\,pg$ to $10\,pg$. For each added mass, the variation of the vibration amplitude of each cantilever on the first mode is shown in Figure 4.17.

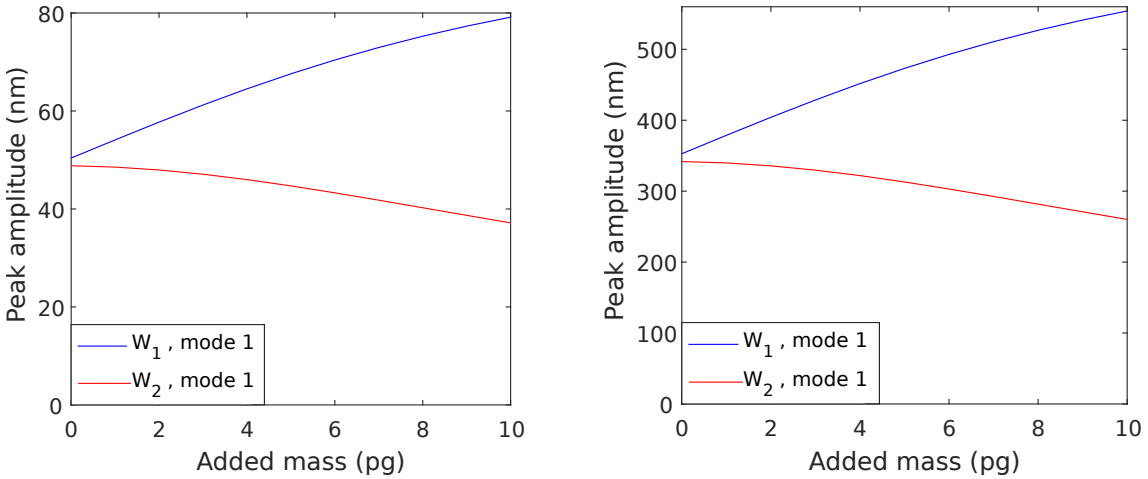

(a) Case 1: with low vibration amplitudes (b) Case 2: with high vibration amplitudes

Figure 4.17: Variation of peak amplitudes (mode 1) as a function of the added mass

Without mass perturbation, we have the same vibration amplitude on each cantilever because it corresponds to the balanced state. If we add a mass perturbation, the vibration of the actuated cantilever (W_1) increases while that of the non-actuated one (W_2) decreases. We assume now that we have a precision of $\pm 5\,nm$ for the amplitude measurement. With this consideration, we calculate for each added mass the actual, the maximum and the minimum values of the amplitude ratio, and the results are shown in Figure 4.18.

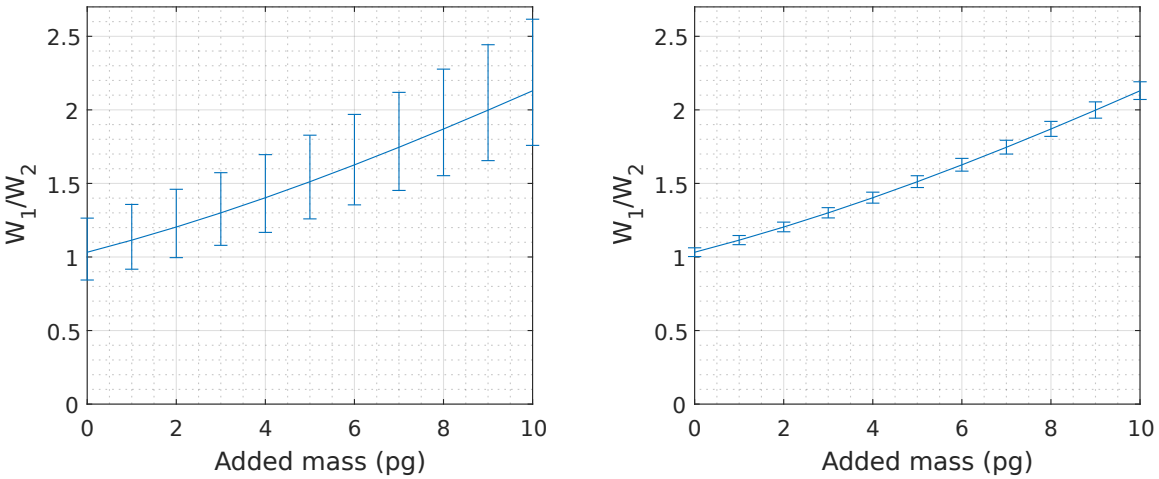

(a) Case 1: with low vibration amplitudes (b) Case 2: with high vibration amplitudes

Figure 4.18: Amplitude ratio as a function of the added mass

We notice in Figure 4.18 that in the two cases, the amplitude ratio becomes less and less accurate as the added mass increases. It is due to the fact that as the vibrations become more localized, the amplitude of the non-actuated cantilever decreases. So, the relative error on the amplitude increases. But if we compare the two cases, the amplitude ratio of the one where we have high vibration amplitudes is always more accurate. Concerning the minimal detectable mass, the maximum value of the amplitude ratio at the veering point gives us a mass resolution around $2.5\,pg$ for the first case,

while for the second case, it is around $0.5\,pg$. This shows us that using a high vibration amplitudes improves the mass resolution of the sensor. Of course, it is a theoretical study in which the precision of the amplitude measurement is fixed. In reality, we can determine it when the appropriate vibration sensing is integrated in the sensor because the LDV is just used for the characterization of the device. The measured vibration with the vibrometer is also sensitive to the position of the laser spot, which can lead to errors that are not related to this device.

4.8 Summary

In this last chapter, the second proposed device using repulsive electrostatic forces has been presented. This device is similar to the first one, but there are just additional side electrodes for the actuation. A FEM model has been used in order to determine the expression of the electrostatic force. It has been shown that the resulting force is less dependent on the out-of-plane position of the cantilever, indicating the absence of electrostatic nonlinearities. From the obtained expression of the force, an analytical model has then been presented. Like for the first device, this model is based on Euler-Bernoulli beams, and the Galerkin discretization with one mode has been used. As the electrostatic softening effect of the actuation is not important, it has been decided to use two cantilevers with the same length. The actuated cantilever which has the highest effective stiffness will then be determined experimentally. After presenting the fabricated device, an experimental investigation including a study of its static and dynamic behaviors has been carried out. In general, we have obtained a good agreement between experimental and theoretical results, but a slight difference has been noticed on the amplitude response. At the balanced state, the vibration amplitudes of each mode have shown that the electrostatic force applied on the non-actuated cantilever is more important than predicted by the model. By using other DC voltages for the actuation, the experimental frequency response has shown more localized vibrations, reflecting a more important softening effect than expected. Concerning the linear dynamic range of the device, the experimental measurements have shown that the vibrations are still linear as long as their amplitudes do not exceed 70 % of the gap. Compared to the device using attractive electrostatic forces, the linear dynamic range of this second device has been significantly improved, allowing us to drive it at higher vibration amplitudes. Finally, a theoretical demonstration of the link between the vibration amplitudes, the mass resolution of the sensor, and the precision of the mass sensing has been conducted. Using high vibration amplitudes not only increases the minimum detectable mass, but also improves the accuracy of the sensor. This clearly shows that a sensor with a high dynamic range is advantageous when the detection method is based on vibration amplitude measurement.

Conclusion

In this thesis, novel concepts allowing to improve the performances of mode localized sensors are proposed and demonstrated through two MEMS devices. This includes the cancellation of initial imbalance due to manufacturing defects, the overcoming of the sensitivity limitation imposed by the mode aliasing, and the improvement of the dynamic range of the sensors. The two considered devices used to highlight these concepts are all composed of two polysilicon microcantilevers connected by a coupling beam. Both devices are electrostatically actuated, but the first uses an attractive force while the second uses a repulsive force. Thanks to the developed analytical model of these devices and the experimentations carried out, the proposed concepts are both theoretically demonstrated and experimentally verified. This thus offers a way to enhance the performances of future mode localized sensors.

Main achievements

Initial imbalance cancellation

As a solution to the initial disorder caused by the manufacturing defects on mode localized sensors, the use of the softening effect of the electrostatic actuation is proposed for both devices.

For the device using attractive electrostatic forces, a configuration with an initial asymmetric system is proposed. It thus includes two cantilevers of different lengths: one of them has a length of $98\,\mu m$ while the other has a length of $100\,\mu m$. By tuning the DC voltage applied on the short cantilever, we can reduce its effective stiffness, cancel the effects of other defects, and balance the system. The chosen length difference allows the use of a DC balancing voltage that is not too close to the pull-in voltage, thus ensuring the proper operation of the device. In nonlinear regime, this DC balancing voltage slightly decreases due to the additional softening effect of electrostatic nonlinearities.

For the device using repulsive electrostatic forces, the same configuration cannot be used due to the weak softening effect of the chosen actuation. The two cantilevers thus have the same length of $100\,\mu m$. Nevertheless, the system can be balanced with a moderate value of the DC voltage applied on the actuated cantilever.

Design improvement

In response to the non-existence of accurate model in the literature, an analytical model based on each device dimensions is proposed, thus allowing to properly design the sensors. As the two devices use the

same mechanical structure, the two models are all based on Euler-Bernoulli beams. Only the modeling of the electrostatic actuation is different.
For the device using attractive electrostatic forces, the use of the multiple scales method shows that it is effective to solve the equation governing the bending vibration of coupled system having nonlinearities.
For the device using repulsive electrostatic forces, the use of a 2D FEM model to evaluate the intensity of the actuation has also proved its effectiveness.
For each device, the fact that there is a good agreement between experimental and theoretical results allows to validate the proposed model, especially the modeling of the mechanical coupling that is an important part of the device. As the models can predict both static and dynamic behavior of the devices, they can be used to design other sensors of the same type.

Sensitivity improvement

In order to overcome the maximum sensitivity imposed by the minimum coupling ratio that prevents mode aliasing, the functionalization of electrostatic nonlinearities is proposed for the device using attractive electrostatic forces. By using a high AC voltage involving a high vibration amplitude, a nonlinearity is introduced and easily tuned, which results in a higher amplitude ratio when a mass perturbation is added. Simulations show that the sensitivity limitation due to the mode aliasing is overcome with a significant improvement of up to 67 %. This is also supported by experiments which show the same trend when a mass of 10 pg is deposited on the device.

Dynamic range enhancement

In order to increase the mass resolution of the sensors, the dynamic range of each device has been improved.
For the device using attractive electrostatic forces, the functionalization of electrostatic nonlinearities allows us to use high vibration amplitudes even if the device is driven beyond its linear dynamic range.
For the device using repulsive electrostatic forces, it exhibits a high linear dynamic range. Compared to the actuation of the first device, this type of actuation creates an electrostatic force which is less dependent of the out-of-plane position of the actuated cantilever, reflecting the absence of nonlinearities. However, the linear dynamic range is not only limited by the initial distance between the cantilever and the bottom electrode. Indeed, experiments show an amplitude dependent damping when the vibrations exceed 70 % of the gap.

Perspectives

The two proposed devices have certainly demonstrated their performance, but there are still areas of improvement that can be investigated.

Resonance tracking

Real time sensing is one of abilities that sensors should have. This is feasible with sensors based on frequency shift by using a closed-loop control circuit. Indeed, it allows to track the resonance frequency

of the resonator without performing a frequency sweep. Some authors have also already demonstrated its use with mode localized sensors [139, 155, 156]. Thus, the system can be automatically driven at the frequency of the mode of interest, allowing a real time measurement of the amplitude ratio. However, it has only been tested on sensors driven in linear regime, while the device using attractive electrostatic forces is driven in nonlinear regime. There have been some studies on the use of closed-loop control circuit with single nonlinear resonators [157, 158]. It would therefore be interesting to study the use of such a readout technique for coupled nonlinear resonators.

Use of longer cantilevers with the repulsive force

For the device with repulsive electrostatic forces, we have seen that the two cantilevers have the same lengths, due to the fact that the softening effect of the actuation is too weak. But the consequence is that neither the microbeam to be actuated nor the DC balancing voltage can be determined in advance. Compared to the first proposed device, this may constitutes a disadvantage. As a solution, the use of longer cantilevers having a lower effective stiffness can be considered. To create the initial imbalance, we can also use two identical cantilevers with just a small part attached to one of them. This then requires an accurate model allowing to evaluate the softening effect of the electrostatic actuation.

Vibration sensing

The last perspective of this thesis is the addition of suitable vibration sensing on the proposed devices. The vibrometer is effective but its use is restricted to experimentation. We have also seen that it slightly perturbs the device. Capacitive sensing is not possible since only one of the two cantilevers is electrostatically actuated. Even if the non actuated cantilever is biased, it is not feasible without additional electrodes. The possible readout technique will be the use of piezoresistive sensing, which can be integrated on cantilevers.

Conferences and publications

Oral presentation and poster

- Eurosensors, Graz, 2018
- Séminaire Franco-Polonais de Mécanique, Besançon, 2019
- ASME conference, Anaheim, 2019

Conference paper

- Eurosensors proceeding, Multidisciplinary Digital Publishing Institute, 2018 [159]
- ASME conference proceeding, International Design Engineering Technical Conferences and Computers and Information in Engineering Conference, 2019 [160]

Journal article

- Sensors and Actuators A: Physical, 2019 [161]
- Applied physics letters, 2020 [162]

Bibliography

[1] Philip W Anderson. Absence of diffusion in certain random lattices. *Physical review*, 109(5):1492, 1958.

[2] Matthew Spletzer, Arvind Raman, Alexander Q Wu, Xianfan Xu, and Ron Reifenberger. Ultrasensitive mass sensing using mode localization in coupled microcantilevers. *Applied Physics Letters*, 88(25):254102, 2006.

[3] Chun Zhao, Mohammad H Montaseri, Graham S Wood, Suan Hui Pu, Ashwin A Seshia, and Michael Kraft. A review on coupled mems resonators for sensing applications utilizing mode localization. *Sensors and Actuators A: Physical*, 249:93–111, 2016.

[4] Chang Liu. *Foundations of MEMS*. Pearson Education India, 2012.

[5] Farrokh Ayazi and Khalil Najafi. Design and fabrication of high-performance polysilicon vibrating ring gyroscope. In *Proceedings MEMS 98. IEEE. Eleventh Annual International Workshop on Micro Electro Mechanical Systems. An Investigation of Micro Structures, Sensors, Actuators, Machines and Systems (Cat. No. 98CH36176*, pages 621–626. IEEE, 1998.

[6] Karolina Laszczyk, Sylwester Bargiel, Christophe Gorecki, Jerzy Krężel, Piotr Dziuban, Małgorzata Kujawińska, Damien Callet, and Sven Frank. A two directional electrostatic comb-drive x–y micro-stage for moems applications. *Sensors and Actuators A: Physical*, 163(1):255–265, 2010.

[7] Kamaljit Rangra, Benno Margesin, Leandro Lorenzelli, Flavio Giacomozzi, Cristian Collini, Mario Zen, Giovanni Soncini, Laura Del Tin, and Roberto Gaddi. Symmetric toggle switch—a new type of rf mems switch for telecommunication applications: Design and fabrication. *Sensors and Actuators A: Physical*, 123:505–514, 2005.

[8] Patrick Griss and Göran Stemme. Side-opened out-of-plane microneedles for microfluidic transdermal liquid transfer. *Journal of Microelectromechanical systems*, 12(3):296–301, 2003.

[9] Marc J Madou. *Fundamentals of microfabrication: the science of miniaturization*. CRC press, 2002.

[10] Patric R Salomon. European mems foundries. In *Micromachining and Microfabrication Process Technology VIII*, volume 4979, pages 327–336. International Society for Optics and Photonics, 2003.

[11] Allen Cowen, Busbee Hardy, Ramaswamy Mahadevan, and Steve Wilcenski. Polymumps design handbook. *MEMSCAP Inc*, 13, 2011.

[12] Hui Xie, Julien Vitard, Sinan Haliyo, and Stéphane Régnier. Enhanced sensitivity of mass detection using the first torsional mode of microcantilevers. In *2007 International Conference on Mechatronics and Automation*, pages 39–44. IEEE, 2007.

[13] LA Pinnaduwage, T Thundat, A Gehl, SD Wilson, DL Hedden, and RT Lareau. Desorption characteristics of uncoated silicon microcantilever surfaces for explosive and common nonexplosive vapors. *Ultramicroscopy*, 100(3-4):211–216, 2004.

[14] Mar Alvarez, Ana Calle, Javier Tamayo, Laura M Lechuga, Antonio Abad, and Angel Montoya. Development of nanomechanical biosensors for detection of the pesticide ddt. *Biosensors and Bioelectronics*, 18(5-6):649–653, 2003.

[15] A Gupta, D Akin, and Rashid Bashir. Single virus particle mass detection using microresonators with nanoscale thickness. *Applied Physics Letters*, 84(11):1976–1978, 2004.

[16] FM Battiston, J-P Ramseyer, HP Lang, MK Baller, Ch Gerber, JK Gimzewski, E Meyer, and H-J Güntherodt. A chemical sensor based on a microfabricated cantilever array with simultaneous resonance-frequency and bending readout. *Sensors and Actuators B: Chemical*, 77(1-2):122–131, 2001.

[17] KL Ekinci, XMH Huang, and ML Roukes. Ultrasensitive nanoelectromechanical mass detection. *Applied Physics Letters*, 84(22):4469–4471, 2004.

[18] In-Bok Baek, Sangwon Byun, Bong Kuk Lee, Jin-Hwa Ryu, Yarkyeon Kim, Yong Sun Yoon, Won Ik Jang, Seongjae Lee, and Han Young Yu. Attogram mass sensing based on silicon microbeam resonators. *Scientific reports*, 7:46660, 2017.

[19] Hongfei Zu, Qing-Ming Wang, and Yanqing Zheng. High temperature piezoelectric bulk acoustic wave mass sensor for thermogravimetric analysis of nano-layer polymer. In *2017 IEEE 17th International Conference on Nanotechnology (IEEE-NANO)*, pages 663–667. IEEE, 2017.

[20] Wenchang Hao, Jiuling Liu, Minghua Liu, Yong Liang, and Shitang He. Mass sensitivity optimization of a surface acoustic wave sensor incorporating a resonator configuration. *Sensors*, 16(4):562, 2016.

[21] Piotr Kunicki, Magdalena Moczała-Dusanowska, Grzegorz Jóźwiak, Paulina Szymanowska, Tomasz Piasecki, and Teodor Gotszalk. Quartz tuning fork mass change sensing for fib/sem technology. *Micron*, 129:102792, 2020.

[22] Hitoshi Nishiyama and Mitsunobu Nakamura. Form and capacitance of parallel-plate capacitors. *IEEE Transactions on Components, Packaging, and Manufacturing Technology: Part A*, 17(3):477–484, 1994.

[23] Joseph Lardies, Olivia Arbey, and Marc Berthillier. Analyse de la tension de collapse dans les transducteurs capacitifs ultrasonores. In *10ème Congrès Français d'Acoustique*, 2010.

[24] Sazzadur Chowdhury, M Ahmadi, and WC Miller. A comparison of pull-in voltage calculation methods for mems-based electrostatic actuator design. In *1st international conference on sensing technology*, pages 112–117, 2005.

[25] Gary O'Brien, David J Monk, and Liwei Lin. Mems cantilever beam electrostatic pull-in model. In *Design, Characterization, and Packaging for MEMS and Microelectronics II*, volume 4593, pages 31–41. International Society for Optics and Photonics, 2001.

[26] Najib Kacem, J Arcamone, F Perez-Murano, and Sebastien Hentz. Dynamic range enhancement of nonlinear nanomechanical resonant cantilevers for highly sensitive nems gas/mass sensor applications. *Journal of Micromechanics and Microengineering*, 20(4):045023, 2010.

[27] Weimin Wang, Qiang Wang, Hao Ren, Wenying Ma, Chuankai Qiu, Zexiang Chen, and Bin Fan. Electrostatic repulsive out-of-plane actuator using conductive substrate. *Scientific reports*, 6:35118, 2016.

[28] WC Tang, MG Lim, and RT Howe. Electrostatic comb drive levitation and control method. *Journal of Microelectromechanical Systems*, 1(4):170–178, 1992.

[29] Ki Bang Lee and Young-Ho Cho. Laterally driven electrostatic repulsive-force microactuators using asymmetric field distribution. *Journal of microelectromechanical systems*, 10(1):128–136, 2001.

[30] Siyuan He and Ridha Ben Mrad. Development of a novel translation micromirror for adaptive optics. In *Optomechatronic Systems IV*, volume 5264, pages 154–161. International Society for Optics and Photonics, 2003.

[31] Imen Rezadad, Javaneh Boroumand Azad, Evan M Smith, Ammar Alhasan, and Robert E Peale. Vertical electrostatic force in mems cantilever ir sensor. In *Infrared Technology and Applications XL*, volume 9070, page 90701U. International Society for Optics and Photonics, 2014.

[32] Hutomo Suryo Wasisto, Stephan Merzsch, Andreas Waag, and Erwin Peiner. Mems-based silicon cantilevers with integrated electrothermal heaters for airborne ultrafine particle sensing. In *Smart Sensors, Actuators, and MEMS VI*, volume 8763, page 87632L. International Society for Optics and Photonics, 2013.

[33] Priyanka Joshi, Sanjeev Kumar, VK Jain, Jamil Akhtar, and Jitendra Singh. Distributed mems mass-sensor based on piezoelectric resonant micro-cantilevers. *Journal of Microelectromechanical Systems*, 28(3):382–389, 2019.

[34] O Ergeneman, P Eberle, M Suter, G Chatzipirpiridis, KM Sivaraman, S Pané, Christofer Hierold, and Bradley J Nelson. An in-plane cobalt–nickel microresonator sensor with magnetic actuation and readout. *Sensors and Actuators A: Physical*, 188:120–126, 2012.

[35] Alibey Ozturk, H Ilker Ocakli, Natali Ozber, Hakan Urey, I Halil Kavakli, and B Erdem Alaca. A magnetically actuated resonant mass sensor with integrated optical readout. *IEEE Photonics Technology Letters*, 20(23):1905–1907, 2008.

[36] JE-Y Lee and AA Seshia. Parasitic feedthrough cancellation techniques for enhanced electrical characterization of electrostatic microresonators. *Sensors and Actuators A: Physical*, 156(1):36–42, 2009.

[37] Yuanjie Xu and Joshua E-Y Lee. Single-device and on-chip feedthrough cancellation for hybrid mems resonators. *IEEE transactions on industrial electronics*, 59(12):4930–4937, 2011.

[38] Oliver Brand and Henry Baltes. Micromachined resonant sensors—an overview. *Sensors update*, 4(1):3–51, 1998.

[39] Frédéric Lochon, Isabelle Dufour, and Dominique Rebiere. An alternative solution to improve sensitivity of resonant microcantilever chemical sensors: comparison between using high-order modes and reducing dimensions. *Sensors and Actuators B: Chemical*, 108(1-2):979–985, 2005.

[40] Anthony James Richardson. Determination of nanogram mass and measurement of polymer solution free volume using thickness-shear mode (tsm) quartz resonators. 2009.

[41] Hayato Sone, Yoshinori Fujinuma, and Sumio Hosaka. Picogram mass sensor using resonance frequency shift of cantilever. *Japanese Journal of Applied Physics*, 43(6R):3648, 2004.

[42] Blake N Johnson and Raj Mutharasan. Expression of picogram sensitive bending modes in piezoelectric cantilever sensors with nonuniform electric fields generated by asymmetric electrodes. *Review of Scientific Instruments*, 81(12):125108, 2010.

[43] Hayato Sone, Ayumi Ikeuchi, Takashi Izumi, Haruki Okano, and Sumio Hosaka. Femtogram mass biosensor using self-sensing cantilever for allergy check. *Japanese journal of applied physics*, 45(3S):2301, 2006.

[44] Dazhong Jin, Xinxin Li, Jian Liu, Guomin Zuo, Yuelin Wang, Min Liu, and Haitao Yu. High-mode resonant piezoresistive cantilever sensors for tens-femtogram resoluble mass sensing in air. *Journal of Micromechanics and Microengineering*, 16(5):1017, 2006.

[45] Jungchul Lee, Wenjiang Shen, Kris Payer, Thomas P Burg, and Scott R Manalis. Toward attogram mass measurements in solution with suspended nanochannel resonators. *Nano letters*, 10(7):2537–2542, 2010.

[46] Ya-Tang Yang, Carlo Callegari, XL Feng, Kamil L Ekinci, and Michael L Roukes. Zeptogram-scale nanomechanical mass sensing. *Nano letters*, 6(4):583–586, 2006.

[47] Manoharan Muruganathan, Hiroya Miyashita, Jothiramalingam Kulothungan, Marek E Schmidt, and Hiroshi Mizuta. Zeptogram level mass sensing of light weight gas molecules using graphene nanomechanical (gnem) resonator. In *2018 IEEE SENSORS*, pages 1–4. IEEE, 2018.

[48] Julien Chaste, A Eichler, J Moser, G Ceballos, R Rurali, and A Bachtold. A nanomechanical mass sensor with yoctogram resolution. *Nature nanotechnology*, 7(5):301–304, 2012.

[49] CH Hodges. Confinement of vibration by structural irregularity. *Journal of sound and vibration*, 82(3):411–424, 1982.

[50] Oddvar O Bendiksen. Mode localization phenomena in large space structures. *AIAA journal*, 25(9):1241–1248, 1987.

[51] Arthur W Leissa. On a curve veering aberration. *Zeitschrift für angewandte Mathematik und Physik ZAMP*, 25(1):99–111, 1974.

[52] Christophe Pierre. Mode localization and eigenvalue loci veering phenomena in disordered structures. 1988.

[53] Pradyumna Thiruvenkatanathan, Jim Woodhouse, Jize Yan, and Ashwin A Seshia. Manipulating vibration energy confinement in electrically coupled microelectromechanical resonator arrays. *Journal of microelectromechanical systems*, 20(1):157–164, 2010.

[54] Tony Chopard, Vivien Lacour, and Therese Leblois. Gaas coupled micro resonators with enhanced sensitive mass detection. *Sensors*, 14(12):22785–22797, 2014.

[55] Daichi Endo, Hiroshi Yabuno, Keiichi Higashino, Yasuyuki Yamamoto, and Sohei Matsumoto. Self-excited coupled-microcantilevers for mass sensing. *Applied Physics Letters*, 106(22):223105, 2015.

[56] Teresa J Ryan. *A Coupled Microresonator Array for Mass Detection.* PhD thesis, Catholic University of America, 2013.

[57] Pradyumna Thiruvenkatanathan, Jize Yan, Jim Woodhouse, and Ashwin A Seshia. Enhancing parametric sensitivity in electrically coupled mems resonators. *Journal of Microelectromechanical Systems*, 18(5):1077–1086, 2009.

[58] P Thiruvenkatanathan, J Yan, J Woodhouse, A Aziz, and AA Seshia. Ultrasensitive mode-localized mass sensor with electrically tunable parametric sensitivity. *Applied Physics Letters*, 96(8):081913, 2010.

[59] Graham S Wood, Chun Zhao, Suan Hui Pu, Stuart A Boden, Ibrahim Sari, and Michael Kraft. Mass sensor utilising the mode-localisation effect in an electrostatically-coupled mems resonator pair fabricated using an soi process. *Microelectronic Engineering*, 159:169–173, 2016.

[60] Guowei Tao and Bhaskar Choubey. A simple technique to readout and characterize coupled mems resonators. *Journal of Microelectromechanical Systems*, 25(4):617–625, 2016.

[61] C Humbert, G Goavec-Merou, V Walter, N Kacem, and T Leblois. Implementation of a tunable hybrid system with coupled high q-factor resonators based on mode localization for sensing purposes. *Smart Materials and Structures*, 29(2):02LT01, 2020.

[62] Claude Humbert, Vincent Walter, Najib Kacem, and Thérèse Leblois. Towards an ultra sensitive hybrid mass sensor based on mode localization without resonance tracking. *Sensors*, 20(18):5295, 2020.

[63] Y Kasai, Hiroshi Yabuno, T Ishine, Y Yamamoto, and S Matsumoto. Mass sensing using a virtual cantilever virtually coupled with a real cantilever. *Applied Physics Letters*, 115(6):063103, 2019.

[64] Dong F Wang, Xiaodong Li, Xu Yang, Tsuyoshi Ikehara, and Ryutaro Maeda. Enhancing amplitude changes by mode localization in trio cantilevers with mass perturbation. *Journal of Micromechanics and Microengineering*, 25(9):095017, 2015.

[65] Yuan Wang, Chun Zhao, Chen Wang, Delphine Cerica, Mathieu Baijot, Vinayak Pachkawade, Ali Ghorbani, Maxime Boutier, Alain Vanderplasschen, and Michael Kraft. A reversible method to characterize the mass sensitivity of a 3-dof mode localized coupled resonator under atmospheric pressure. In *Multidisciplinary Digital Publishing Institute Proceedings*, volume 1, page 493, 2017.

[66] Yuan Wang, Chun Zhao, Chen Wang, Delphine Cerica, Mathieu Baijot, Qijun Xiao, Serguei Stoukatch, and Michael Kraft. A mass sensor based on 3-dof mode localized coupled resonator under atmospheric pressure. *Sensors and Actuators A: Physical*, 279:254–262, 2018.

[67] Dong F Wang, Keisuke Chatani, Tsuyoshi Ikehara, and Ryutaro Maeda. Mode localization analysis and characterization in a 5-beam array of coupled nearly identical micromechanical resonators for ultra-sensitive mass detection and analyte identification. *Microsystem technologies*, 18(11):1923–1929, 2012.

[68] Matthew Spletzer, Arvind Raman, Hartono Sumali, and John P Sullivan. Highly sensitive mass detection and identification using vibration localization in coupled microcantilever arrays. *Applied Physics Letters*, 92(11):114102, 2008.

[69] Chun Zhao, Graham S Wood, Jianbing Xie, Honglong Chang, Suan Hui Pu, Harold MH Chong, and Michael Kraft. A sensor for stiffness change sensing based on three weakly coupled resonators with enhanced sensitivity. In *2015 28th IEEE International Conference on Micro Electro Mechanical Systems (MEMS)*, pages 881–884. IEEE, 2015.

[70] Chun Zhao, Graham S Wood, Jianbing Xie, Honglong Chang, Suan Hui Pu, and Michael Kraft. A three degree-of-freedom weakly coupled resonator sensor with enhanced stiffness sensitivity. *Journal of Microelectromechanical Systems*, 25(1):38–51, 2015.

[71] Hemin Zhang, Honglong Chang, and Weizheng Yuan. Characterization of forced localization of disordered weakly coupled micromechanical resonators. *Microsystems & nanoengineering*, 3(1):1–9, 2017.

[72] Hemin Zhang, Jing Yang, Weizheng Yuan, and Honglong Chang. Linear sensing for mode-localized sensors. *Sensors and Actuators A: Physical*, 277:35–42, 2018.

[73] Pradyumna Thiruvenkatanathan, Jize Yan, and A Ashwin Seshia. Ultrasensitive mode-localized micromechanical electrometer. In *2010 IEEE International Frequency Control Symposium*, pages 91–96. IEEE, 2010.

[74] Chun Zhao, Graham S Wood, Jianbing Xie, Honglong Chang, Suan Hui Pu, and Michael Kraft. A force sensor based on three weakly coupled resonators with ultrahigh sensitivity. *Sensors and Actuators A: Physical*, 232:151–162, 2015.

[75] Pradeep Pai, Hoorad Pourzand, and Massood Tabib-Azar. Magnetically coupled resonators for rate integrating gyroscopes. In *SENSORS, 2014 IEEE*, pages 1173–1176. IEEE, 2014.

[76] Hemin Zhang, Boyang Li, Weizheng Yuan, Michael Kraft, and Honglong Chang. An acceleration sensing method based on the mode localization of weakly coupled resonators. *Journal of microelectromechanical systems*, 25(2):286–296, 2016.

[77] Milind Pandit, Chun Zhao, Guillermo Sobreviela, Arif Mustafazade, Xudong Zou, and Ashwin A Seshia. A mode-localized mems accelerometer with 7μg bias stability. In *2018 IEEE Micro Electro Mechanical Systems (MEMS)*, pages 968–971. IEEE, 2018.

[78] Hao Kang, Jing Yang, Jiming Zhong, Heming Zhang, and Honglong Chang. A mode-localized accelerometer based on three degree-of-freedom weakly coupled resonator. In *2017 IEEE SENSORS*, pages 1–3. IEEE, 2017.

[79] Hao Kang, Jing Yang, and Honglong Chang. A mode-localized accelerometer based on four degree-of-freedom weakly coupled resonators. In *2018 IEEE Micro Electro Mechanical Systems (MEMS)*, pages 960–963. IEEE, 2018.

[80] Claude Humbert, Gwenhaël Goavec Merou, Thomas Bertin, Najib Kacem, Vincent Walter, and Thérèse Leblois. On the implementation of mode localization between physical and digital resonators. In *2018 IEEE International Ultrasonics Symposium (IUS)*, pages 1–4. IEEE, 2018.

[81] Chun Zhao, Graham S Wood, Jianbing Xie, Honglong Chang, Suan Hui Pu, and Michael Kraft. A comparative study of output metrics for an mems resonant sensor consisting of three weakly coupled resonators. *Journal of Microelectromechanical Systems*, 25(4):626–636, 2016.

[82] Shuyi Liu, Dong F Wang, Di Zhou, Jing Hong, and Maeda Ryutaro. Amplitude difference changes based metrological scheme for force detection in a mode-localized 5-beam array. *IEEE Sensors Journal*, 2019.

[83] Eduardo Gil-Santos, Daniel Ramos, Anirban Jana, Montserrat Calleja, Arvind Raman, and Javier Tamayo. Mass sensing based on deterministic and stochastic responses of elastically coupled nanocantilevers. *Nano letters*, 9(12):4122–4127, 2009.

[84] Hemin Zhang, Hao Kang, and Honglong Chang. Suppression on nonlinearity of mode-localized sensors using algebraic summation of amplitude ratios as the output metric. *IEEE Sensors Journal*, 18(19):7802–7809, 2018.

[85] Guowei Tao, Hemin Zhang, Honglong Chang, and Bhaskar Choubey. Inverse eigenvalue sensing in coupled micro/nano system. *Journal of Microelectromechanical Systems*, 27(5):886–895, 2018.

[86] Vijay Kumar, J William Boley, Yushi Yang, Hendrik Ekowaluyo, Jacob K Miller, George T-C Chiu, and Jeffrey F Rhoads. Bifurcation-based mass sensing using piezoelectrically-actuated microcantilevers. *Applied Physics Letters*, 98(15):153510, 2011.

[87] Vijay Kumar, Yushi Yang, J William Boley, George T-C Chiu, and Jeffrey F Rhoads. Modeling, analysis, and experimental validation of a bifurcation-based microsensor. *Journal of microelectromechanical systems*, 21(3):549–558, 2012.

[88] V-N Nguyen, Sébastien Baguet, C-H Lamarque, and Régis Dufour. Bifurcation-based micro-/nanoelectromechanical mass detection. *Nonlinear Dynamics*, 79(1):647–662, 2015.

[89] MS Al-Ghamdi, ME Khater, KME Stewart, Ayman Alneamy, Eihab M Abdel-Rahman, and Alexander Penlidis. Dynamic bifurcation mems gas sensors. *Journal of Micromechanics and Microengineering*, 29(1):015005, 2018.

[90] Wenhua Zhang, Rajashree Baskaran, and Kimberly L Turner. Nonlinear behavior of a parametric resonance-based mass sensor. In *ASME 2002 International Mechanical Engineering Congress and Exposition*, pages 121–125. American Society of Mechanical Engineers Digital Collection, 2002.

[91] Wenhua Zhang and Kimberly L Turner. A mass sensor based on parametric resonance. In *Proceedings of the Workshop on Solid-State Sensors and Actuators*, pages 49–52, 2004.

[92] Christiane Ziegler. Cantilever-based biosensors. *Analytical and bioanalytical chemistry*, 379(7-8):946–959, 2004.

[93] Mo Yang, Xuan Zhang, Kambiz Vafai, and Cengiz S Ozkan. High sensitivity piezoresistive cantilever design and optimization for analyte-receptor binding. *Journal of Micromechanics and Microengineering*, 13(6):864, 2003.

[94] J Fritz, MK Baller, HP Lang, H Rothuizen, P Vettiger, E Meyer, H-J Güntherodt, Ch Gerber, and JK Gimzewski. Translating biomolecular recognition into nanomechanics. *Science*, 288(5464):316–318, 2000.

[95] Jorge Amirola, Angel Rodiguez, and Luis Castaner. Design fabrication and test of micromachined-silicon capacitive gas sensors with integrated readout. In *Smart Sensors, Actuators, and MEMS*, volume 5116, pages 92–99. International Society for Optics and Photonics, 2003.

[96] M Helm, JJ Servant, F Saurenbach, and Rüdiger Berger. Read-out of micromechanical cantilever sensors by phase shifting interferometry. *Applied Physics Letters*, 87(6):064101, 2005.

[97] Pradyumna Thiruvenkatanathan, Jize Yan, and A Ashwin Seshia. Common mode rejection in electrically coupled mems resonators utilizing mode localization for sensor applications. In *2009 IEEE international frequency control symposium joint with the 22nd European frequency and time forum*, pages 358–363. IEEE, 2009.

[98] Milind Pandit, Chun Zhao, Guillermo Sobreviela, and Ashwin Seshia. Practical limits to common mode rejection in mode localized weakly coupled resonators. *IEEE Sensors Journal*, 2019.

[99] Pradyumna Thiruvenkatanathan, Jim Woodhouse, Jize Yan, and Ashwin A Seshia. Limits to mode-localized sensing using micro-and nanomechanical resonator arrays. *Journal of Applied Physics*, 109(10):104903, 2011.

[100] Vincent Walter, Gilles Bourbon, P Le Moal, Najib Kacem, and Joseph Lardies. Electrostatic actuation to counterbalance the manufacturing defects in a mems mass detection sensor using mode localization. *Procedia Engineering*, 168:1488–1491, 2016.

[101] Stephen Timoshenko. *Strength of materials Part 1.* D. Van Nostrand Co., Inc, 1940.

[102] Gino Rinaldi, Muthukumaran Packirisamy, and Ion Stiharu. Quantitative boundary support characterization for cantilever mems. *Sensors*, 7(10):2062–2079, 2007.

[103] Zuo-Yang Zhong, Wen-Ming Zhang, and Guang Meng. Dynamic characteristics of micro-beams considering the effect of flexible supports. *Sensors*, 13(12):15880–15897, 2013.

[104] S Kukla, J Przybylski, and L Tomski. Longitudinal vibration of rods coupled by translational springs. *Journal of Sound and Vibration*, 4(185):717–722, 1995.

[105] M Gürgöze, G ERDO Ğ, and S INCEO Ğ. Bending vibrations of beams coupled by a double spring–mass system. *Journal of Sound and Vibration*, 2(243):361–369, 2001.

[106] S INCEO Ğ and M Gürgöze. Bending vibrations of beams coupled by several double spring-mass systems. *Journal of Sound and Vibration*, 243(2):370–379, 2001.

[107] H-P Lin and D Yang. Dynamic responses of two beams connected by a spring-mass device. *Journal of Mechanics*, 29(1):143–155, 2013.

[108] Anita Ciekot and Stanisław Kukla. Free vibration to a system of cantilever nanobeams. *Journal of Applied Mathematics and Computational Mechanics*, 13(3):29–36, 2014.

[109] LA Bergman and D Michael McFarland. On the vibration of a point-supported linear distributed system. *Journal of vibration, acoustics, stress, and reliability in design*, 110(4):485–492, 1988.

[110] Philip D Cha and Nathanael C Yoder. Applying sherman-morrison-woodbury formulas to analyze the free and forced responses of a linear structure carrying lumped elements. *Journal of Vibration and Acoustics*, 129(3):307–316, 2007.

[111] Leszek Majkut. Eigenvalue based inverse model of beam for structural modification and diagnostics: theoretical formulation. *Latin American Journal of Solids and Structures*, 7(4):423–436, 2010.

[112] Gürkan Şcedilakar. The effect of axial force on the free vibration of an euler-bernoulli beam carrying a number of various concentrated elements. *Shock and Vibration*, 20(3):357–367, 2013.

[113] Heye Xiao, Zhihong Liu, Zhaoyu Wei, et al. The study on free vibration of elastically restrained beams carrying various types of attachments with arbitrary spatial distributions. *Shock and Vibration*, 20(3):369–383, 2013.

[114] William N Sharpe, Bin Yuan, Ranji Vaidyanathan, and Richard L Edwards. Measurements of young's modulus, poisson's ratio, and tensile strength of polysilicon. In *Proceedings IEEE the tenth annual international workshop on micro electro mechanical systems. An investigation of micro structures, sensors, actuators, machines and robots*, pages 424–429. IEEE, 1997.

[115] Jérôme Juillard, Pierre Prache, P Maris Ferreira, and Nuria Barniol. Impact of output metric on the resolution of mode-localized mems resonant sensors. In *2017 Joint Conference of the European Frequency and Time Forum and IEEE International Frequency Control Symposium (EFTF/IFCS)*, pages 506–509. IEEE, 2017.

[116] Jérôme Juillard, Pierre Prache, Pietro Maris Ferreira, and Nuria Barniol. Ultimate limits of differential resonant mems sensors based on two coupled linear resonators. *IEEE transactions on ultrasonics, ferroelectrics, and frequency control*, 65(12):2440–2448, 2018.

[117] DJ Inman. Engineering vibration. pearson, 2014.

[118] Mohammad I Younis, Eihab M Abdel-Rahman, and Ali Nayfeh. A reduced-order model for electrically actuated microbeam-based mems. *Journal of Microelectromechanical systems*, 12(5):672–680, 2003.

[119] Van-Nghi Nguyen. *Principes alternatifs pour la détection de masse ultime via la dynamique non linéaire de capteurs résonants M/NEMS*. PhD thesis, Lyon, INSA, 2013.

[120] Najib Kacem, Sébastien Baguet, Sebastien Hentz, and Régis Dufour. Computational and quasi-analytical models for non-linear vibrations of resonant mems and nems sensors. *International Journal of Non-Linear Mechanics*, 46(3):532–542, 2011.

[121] Ali H Nayfeh, Mohammad I Younis, and Eihab M Abdel-Rahman. Dynamic pull-in phenomenon in mems resonators. *Nonlinear dynamics*, 48(1-2):153–163, 2007.

[122] Adam Bouchaala, Ali H Nayfeh, and Mohammad I Younis. Frequency shifts of micro and nano cantilever beam resonators due to added masses. *Journal of Dynamic Systems, Measurement, and Control*, 138(9), 2016.

[123] Ali H Nayfeh and Dean T Mook. *Nonlinear oscillations*. John Wiley & Sons, 2008.

[124] Panagiotis Alevras, Stephanos Theodossiades, and Homer Rahnejat. Broadband energy harvesting from parametric vibrations of a class of nonlinear mathieu systems. *Applied Physics Letters*, 110(23):233901, 2017.

[125] Rumeng Liu, Lifeng Wang, and Junhua Zhao. Nonlinear vibrations of circular single-layer black phosphorus resonators. *Applied Physics Letters*, 113(21):211901, 2018.

[126] Diala Bitar, Najib Kacem, and Noureddine Bouhaddi. Investigation of modal interactions and their effects on the nonlinear dynamics of a periodic coupled pendulums chain. *International Journal of Mechanical Sciences*, 127:130–141, 2017.

[127] Marcin Marzencki, Maxime Defosseux, and Skandar Basrour. Mems vibration energy harvesting devices with passive resonance frequency adaptation capability. *Journal of Microelectromechanical Systems*, 18(6):1444–1453, 2009.

[128] Liuyang Xiong, Lihua Tang, and Brian R Mace. Internal resonance with commensurability induced by an auxiliary oscillator for broadband energy harvesting. *Applied Physics Letters*, 108(20):203901, 2016.

[129] Wei Yang and Shahrzad Towfighian. A parametric resonator with low threshold excitation for vibration energy harvesting. *Journal of Sound and Vibration*, 446:129–143, 2019.

[130] Najib Kacem, Sébastien Baguet, Laurent Duraffourg, Georges Jourdan, Régis Dufour, and Sébastien Hentz. Overcoming limitations of nanomechanical resonators with simultaneous resonances. *Applied Physics Letters*, 107(7):073105, 2015.

[131] I Kozinsky, HW Ch Postma, I Bargatin, and ML Roukes. Tuning nonlinearity, dynamic range, and frequency of nanomechanical resonators. *Applied Physics Letters*, 88(25):253101, 2006.

[132] Najib Kacem, Sebastien Hentz, David Pinto, Bruno Reig, and V Nguyen. Nonlinear dynamics of nanomechanical beam resonators: improving the performance of nems-based sensors. *Nanotechnology*, 20(27):275501, 2009.

[133] Kianoush Naeli and Oliver Brand. Dimensional considerations in achieving large quality factors for resonant silicon cantilevers in air. *Journal of applied Physics*, 105(1):014908, 2009.

[134] Weibin Zhang and Kimberly L Turner. Pressure-dependent damping characteristics of microsilicon beam resonators for different resonant modes. In *SENSORS, 2005 IEEE*, pages 4–pp. IEEE, 2005.

[135] Zhili Hao, Ahmet Erbil, and Farrokh Ayazi. An analytical model for support loss in micromachined beam resonators with in-plane flexural vibrations. *Sensors and Actuators A: Physical*, 109(1-2):156–164, 2003.

[136] Feng Xu, Yuliang Wei, Shiyuan Bian, Huanqin Wang, Da-Ren Chen, and Deyi Kong. Simulation-based design and optimization of rectangular micro-cantilever-based aerosols mass sensor. *Sensors*, 20(3):626, 2020.

[137] Jérôme Juillard, Ali Mostafa, and Pietro Maris Ferreira. Nonlinear operation of resonant sensors based on weakly coupled resonators: Theory and modeling. *IEEE Transactions on Ultrasonics, Ferroelectrics, and Frequency Control*, 66(12):1950–1961, 2019.

[138] Jerome Juillard. A comparative study of reduced-order modeling techniques for nonlinear mems beams. In *2014 Symposium on Design, Test, Integration and Packaging of MEMS/MOEMS (DTIP)*, pages 1–5. IEEE, 2014.

[139] Chun Zhao, Milind Pandit, Boqian Sun, Guillermo Sobreviela, Xudong Zou, and Ashwin Seshia. A closed-loop readout configuration for mode-localized resonant mems sensors. *Journal of Microelectromechanical Systems*, 26(3):501–503, 2017.

[140] W Wu, O Gottlieb, and A Shavit. Transient thermoelastic dynamics of a microcantilever subject to laser irradiation. In *Seventh International Conference on Vibration Measurements by Laser Techniques: Advances and Applications*, volume 6345, page 63451B. International Society for Optics and Photonics, 2006.

[141] G Rousset, F Lepoutre, and L Bertrand. Influence of thermoelastic bending on photoacoustic experiments related to measurements of thermal diffusivity of metals. *Journal of applied physics*, 54(5):2383–2391, 1983.

[142] Maria Allegrini, C Ascoli, P Baschieri, F Dinelli, C Frediani, A Lio, and T Mariani. Laser thermal effects on atomic force microscope cantilevers. *Ultramicroscopy*, 42:371–378, 1992.

[143] Ferdinando Cannella and Barbara Marchetti. Evaluation of thermal loading effects of laser doppler vibrometer applied to micro-electro-mechanical systems (mems). In *Sixth International Conference on Vibration Measurements by Laser Techniques: Advances and Applications*, volume 5503, pages 468–477. International Society for Optics and Photonics, 2004.

[144] Joydeep Basu and Tarun Kanti Bhattacharyya. Microelectromechanical resonators for radio frequency communication applications. *Microsystem technologies*, 17(10-11):1557, 2011.

[145] Chao-Yu Chen, Ming-Huang Li, Chi-Hang Chin, and Sheng-Shian Li. Implementation of a cmos-mems filter through a mixed electrical and mechanical coupling scheme. *Journal of Microelectromechanical Systems*, 25(2):262–274, 2016.

[146] S He, R Ben Mrad, and J Chong. Repulsive-force out-of-plane large stroke translation micro electrostatic actuator. *Journal of Micromechanics and Microengineering*, 21(7):075002, 2011.

[147] Hao Ren, Weimin Wang, Fenggang Tao, and Jun Yao. A bi-directional out-of-plane actuator by electrostatic force. *Micromachines*, 4(4):431–443, 2013.

[148] Meysam Daeichin, Ronald Miles, and Shahrzad Towfighian. Lateral pull-in instability of electrostatic mems transducers employing repulsive force. *NONLINEAR DYNAMICS*, 2020.

[149] Gang Li, Xingjun Guo, Qinghua Zhao, Jie Hu, Pengwei Li, Wendong Zhang, and Chaoqun Cheng. An electrostatic repulsive-force based micro actuator for capacitive rf mems switch. In *2015 IEEE 15th International Conference on Nanotechnology (IEEE-NANO)*, pages 1095–1098. IEEE, 2015.

[150] Mehmet Ozdogan, Meysam Daeichin, Abdallah Ramini, and Shahrzad Towfighian. Parametric resonance of a repulsive force mems electrostatic mirror. *Sensors and Actuators A: Physical*, 265:20–31, 2017.

[151] Mark Pallay, Meysam Daeichin, and Shahrzad Towfighian. Dynamic behavior of an electrostatic mems resonator with repulsive actuation. *Nonlinear Dynamics*, 89(2):1525–1538, 2017.

[152] Mark Pallay and Shahrzad Towfighian. A reliable mems switch using electrostatic levitation. *Applied Physics Letters*, 113(21):213102, 2018.

[153] Mark Pallay, Alwathiqbellah I Ibrahim, Ronald N Miles, and Shahrzad Towfighian. Pairing electrostatic levitation with triboelectric transduction for high-performance self-powered mems sensors and actuators. *Applied Physics Letters*, 115(13):133503, 2019.

[154] Siyuan He and Ridha Ben Mrad. Design, modeling, and demonstration of a mems repulsive-force out-of-plane electrostatic micro actuator. *Journal of Microelectromechanical Systems*, 17(3):532–547, 2008.

[155] Jing Yang, Jiming Zhong, and Honglong Chang. A closed-loop mode-localized accelerometer. *Journal of Microelectromechanical Systems*, 27(2):210–217, 2018.

[156] Xueyong Wei, Hongcai Zhang, Yanyu Ding, and Juan Ren. Closed-loop capacitive readout based on mode localization effect in weakly-coupled rlc circuits. *Sensors and Actuators A: Physical*, 304:111904, 2020.

[157] Hossein Sohanian-Haghighi and Amir Hossein Davaie-Markazi. Resonance tracking of nonlinear mems resonators. *IEEE/ASME transactions on Mechatronics*, 17(4):617–621, 2011.

[158] Yan Su, Pengfei Xu, Guowei Han, Chaowei Si, Jin Ning, and Fuhua Yang. The characteristics and locking process of nonlinear mems gyroscopes. *Micromachines*, 11(2):233, 2020.

[159] Toky Rabenimanana, Vincent Walter, Najib Kacem, Patrice Le Moal, and Joseph Lardiès. Nonlinear analytical model of two weakly coupled mems cantilevers for mass sensing using electrostatic actuation. In *Multidisciplinary Digital Publishing Institute Proceedings*, volume 2, page 1084, 2018.

[160] Toky Rabenimanana, Vincent Walter, Najib Kacem, Patrice Le Moal, Gilles Bourbon, and Joseph Lardiès. Mode localization in two coupled nearly identical mems cantilevers for mass sensing. In *International Design Engineering Technical Conferences and Computers and Information in Engineering Conference*, volume 59223, page V004T08A008. American Society of Mechanical Engineers, 2019.

[161] Toky Rabenimanana, Vincent Walter, Najib Kacem, Patrice Le Moal, Gilles Bourbon, and Joseph Lardies. Mass sensor using mode localization in two weakly coupled mems cantilevers with different lengths: Design and experimental model validation. *Sensors and Actuators A: Physical*, 295:643–652, 2019.

[162] Toky Rabenimanana, Vincent Walter, Najib Kacem, Patrice Le Moal, Gilles Bourbon, and Joseph Lardiès. Functionalization of electrostatic nonlinearities to overcome mode aliasing limitations in the sensitivity of mass microsensors based on energy localization. *Applied Physics Letters*, 117(3):033502, 2020.

Appendices

A.1 Steps of the MUMPS®

(a) Deposition of the nitride and the Poly0

(b) Patterning of the Poly0

(c) Deposition of the 1st oxide

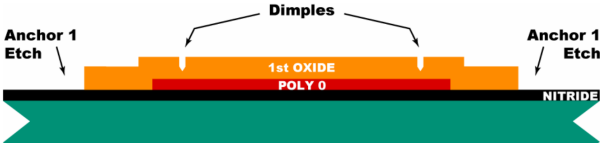

(d) Patterning of the 1st oxide

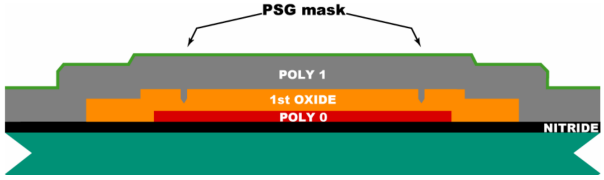

(e) Deposition of the Poly1

(f) Patterning of the Poly1

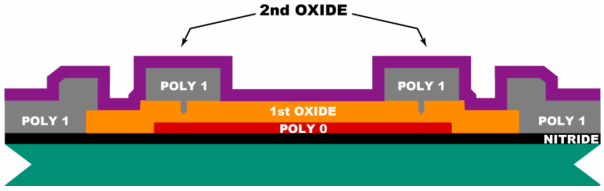

(g) Deposition of the 2nd oxide

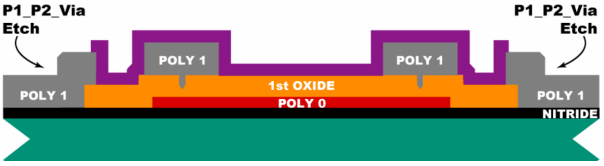

(h) Patterning of the 2nd oxide

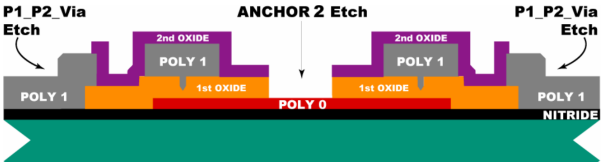

(i) Patterning of the anchors

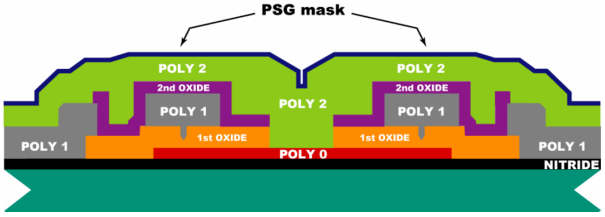

(j) Deposition of the Poly2

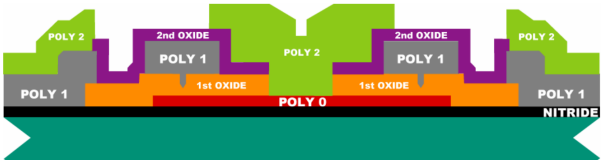

(k) Patterning of the Poly2

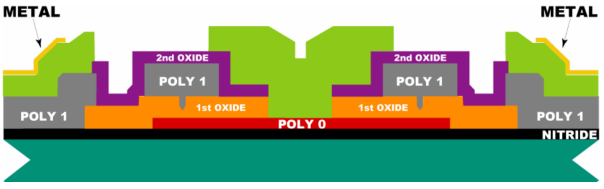

(l) Patterning of the metal layer

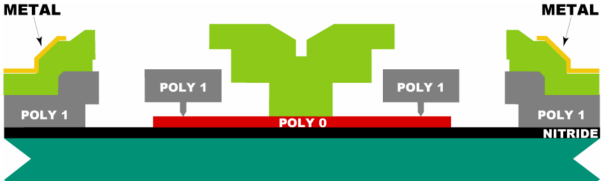

(m) The final structure after removing the sacrificial layers

Figure A.1: Steps of the MUMPS® [11]

A.2 Coefficient β for the torsional stiffness of the coupling beam

Table A.1: Data for the twist of a shaft with rectangular cross section [101]

b_c/h	1.00	1.50	1.75	2.00	2.50	3.00	4.00	6	8	10	∞
β	0.141	0.196	0.214	0.229	0.249	0.263	0.281	0.299	0.307	0.313	0.333

A.3 *Cast3M* script for the finite element model of two coupled cantilevers

```
************************************************************************
*              EIGENFREQUENCIES OF TWO COUPLED CANTILEVERS             *
************************************************************************
* CANTILEVERS
L1 = 100E-6 ; L2 = 100E-6 ;
B = 20E-6 ; H = 1.3E-6 ;
IY = B*(H**3)/12 ; IZ = H*(B**3)/12 ;
IT = IY + IZ ; SB = B * H ;
* COUPLING BEAM
LC = 65E-6 ; BC = 3.E-6 ; H = 1.3E-6 ;
IYC = BC*(H**3)/12 ; IZC = H*(BC**3)/12 ;
ITC = 0.242*BC*(H**3) ; SC = BC * H ; XC = 5.5E-6 ;
* MATERIAL PROPERTIES
E = 163E9 ; NUP = 0.22 ; RHOP = 2320 ;
* TORSIONAL SPRING AT THE FIXED END
KE = 3.0E-7 ;
* MESH
*     P3                P6
*      !                 !
*      !                 !
*      !                 !
*     P2 ------------- P5
*      !                 !
* --- P1 ------------- P4 ---
OPTI DIME 3 ELEM SEG2 EPSI LINEAIRE DENS 0.1E-6 ;
P1 = 0.  0.  0.  ; P2 = XC. 0.  0.  ; P3 = L1 0.  0.  ;
P4 = 0.  LC 0.  ; P5 = XC LC 0.  ; P6 = L2 LC 0.  ;
B1 = (DROI P1 P2) ET (DROI P2 P3) ;
B2 = (DROI P4 P5) ET (DROI P5 P6) ;
```

```
C = DROI P2 P5 ;
RES = B1 ET B2 ET C ;
* MODE
MOB1 = MODE B1 MECANIQUE ELASTIQUE ISOTROPE POUT ;
MOB2 = MODE B2 MECANIQUE ELASTIQUE ISOTROPE POUT ;
MOC = MODE C MECANIQUE ELASTIQUE ISOTROPE POUT ;
* MATERIAL
MATEB1 = MATE MOB1 YOUNG E NU NUP RHO RHOP ;
CARB1 = CARA MOB1 SECT SB INRY IY INRZ IZ TORS IT VECT (0.  1.  0.)  ;
MATEB1 = MATEB1 ET CARB1 ;
MATEB2 = MATE MOB2 YOUNG E NU NUP RHO RHOP ;
CARB2 = CARA MOB2 SECT SB INRY IY INRZ IZ TORS IT VECT (0.  1.  0.)  ;
MATEB2 = MATEB2 ET CARB2 ;
MATEC = MATE MOC YOUNG E NU NUP RHO RHOP ;
CARC = CARA MOC SECT SC INRY IYC INRZ IZC TORS ITC VECT (1.  0.  0.)  ;
MATEC = MATEC ET CARC ;
* BOUNDARY CONDITIONS ;
CL1 = BLOQ UX UY UZ RX RZ (P1 ET P4) ;
CL2 = APPUI RY KE P1 ;
CL3 = APPUI RY KE P4 ;
CL = CL1 ET CL2 ET CL3 ;
* STIFFNESS
RIGB1 = RIGI MATEB1 MOB1 ;
RIGB2 = RIGI MATEB2 MOB2 ;
RIGC = RIGI MATEC MOC ;
RIGT = RIGB1 ET RIGB2 ET RIGC ; RIGT = RIGT ET CL ;
* MASS
MASSB1 = MASS MOB1 MATEB1 ;
MASSB2 = MASS MOB2 MATEB2 ;
MASSC = MASS MOC MATEC ;
MASST = MASSB1 ET MASSB2 ET MASSC ;
* EIGENFREQUENCIES
TAB1 = VIBR INTER 0.  200.E4 MASST RIGT TBAS ;
TAB2 = TAB1.modes ;
F1 = (TAB2.1).frequence ;
F2 = (TAB2.2).frequence ;
MESS ' FREQUENCY 1 (Hz) :  '  F1 ;
MESS ' FREQUENCY 2 (Hz) :  '  F2 ;
```

A.4 Free vibration of a single cantilever with a flexible support

We study in this section the free vibration of a single cantilever with a length L and with a rotational spring $\tilde{k}_e$ at its end (Figure A.2).

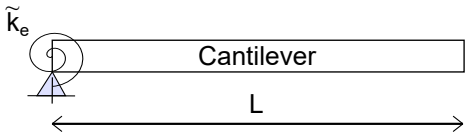

Figure A.2: Model of single cantilever with a flexible support

A.4.1 eigenfrequency

The equation governing the free undamped bending vibration of the beam in Figure A.2 is given by

$$EI\tilde{w}'''' + \rho bh\ddot{\tilde{w}} = 0 \tag{A.1}$$

After a variable separation, the deflection $\tilde{w}$ can be expressed as

$$\tilde{w}\left(\tilde{x},\tilde{t}\right) = \phi\left(\tilde{x}\right) * \cos\left(\omega\tilde{t}\right) \tag{A.2}$$

where $\phi\left(\tilde{x},\tilde{t}\right)$ is the mode shape of the cantilever and ω is its the angular frequency. The mode shape can be expressed as

$$\phi\left(\tilde{x}\right) = A\cos\left(\tilde{\lambda}\tilde{x}\right) + B\sin\left(\tilde{\lambda}\tilde{x}\right) + C\cosh\left(\tilde{\lambda}\tilde{x}\right) + D\sinh\left(\tilde{\lambda}\tilde{x}\right) \tag{A.3}$$

The boundary conditions at $\tilde{x} = 0$ and $\tilde{x} = L$ give us

$$\begin{aligned} \phi\left(0\right) &= 0 \\ \mathrm{EI}\phi''\left(0\right) &= \tilde{k}_e\phi'\left(0\right) \\ \phi''\left(L\right) &= 0 \\ \phi'''\left(L\right) &= 0 \end{aligned} \tag{A.4}$$

By considering these equations, we obtain

$$\begin{aligned} A &= -C \\ A &= -\frac{\tilde{k}_e}{2EI\tilde{\lambda}}\left(B+D\right) \\ \frac{\tilde{k}_e}{2EI\tilde{\lambda}}\left(B+D\right)\cos\left(\tilde{\lambda}L\right) - B\sin\left(\tilde{\lambda}L\right) + \frac{\tilde{k}_e}{2EI\tilde{\lambda}}\left(B+D\right)\cosh\left(\tilde{\lambda}L\right) + D\sinh\left(\tilde{\lambda}L\right) &= 0 \\ -\frac{\tilde{k}_e}{2EI\tilde{\lambda}}\left(B+D\right)\sin\left(\tilde{\lambda}L\right) - B\cos\left(\tilde{\lambda}L\right) + \frac{\tilde{k}_e}{2EI\tilde{\lambda}}\left(B+D\right)\sinh\left(\tilde{\lambda}L\right) + D\cosh\left(\tilde{\lambda}L\right) &= 0 \end{aligned} \tag{A.5}$$

By transforming the two last equations of Equation (A.5) into matrix form, we have

$$\left[\ M\ \right] * \begin{bmatrix} B \\ D \end{bmatrix} = \begin{bmatrix} 0 \\ 0 \end{bmatrix} \tag{A.6}$$

where

$$\left[\ M\ \right] = \begin{bmatrix} \frac{\tilde{k}_e}{2EI\tilde{\lambda}}\cos\left(\tilde{\lambda}L\right) + \frac{\tilde{k}_e}{2EI\tilde{\lambda}}\cosh\left(\tilde{\lambda}L\right) - \sin\left(\tilde{\lambda}L\right) & \frac{\tilde{k}_e}{2EI\tilde{\lambda}}\cos\left(\tilde{\lambda}L\right) + \frac{\tilde{k}_e}{2EI\tilde{\lambda}}\cosh\left(\tilde{\lambda}L\right) + \sinh\left(\tilde{\lambda}L\right) \\ -\frac{\tilde{k}_e}{2EI\tilde{\lambda}}\sin\left(\tilde{\lambda}L\right) + \frac{\tilde{k}_e}{2EI\tilde{\lambda}}\sinh\left(\tilde{\lambda}L\right) - \cos\left(\tilde{\lambda}L\right) & -\frac{\tilde{k}_e}{2EI\tilde{\lambda}}\sin\left(\tilde{\lambda}L\right) + \frac{\tilde{k}_e}{2EI\tilde{\lambda}}\sinh\left(\tilde{\lambda}L\right) + \cosh\left(\tilde{\lambda}L\right) \end{bmatrix} \tag{A.7}$$

and the existence of non-trivial solutions involves :

$$det\left[\ M\ \right] = 0 \tag{A.8}$$

By calculating the determinant of this matrix, we obtain

$$\frac{\tilde{k}_e}{EI\tilde{\lambda}}\left[\cos\left(\tilde{\lambda}L\right)\cosh\left(\tilde{\lambda}L\right) + 1\right] + \cos\left(\tilde{\lambda}L\right)\sinh\left(\tilde{\lambda}L\right) - \sin\left(\tilde{\lambda}L\right)\cosh\left(\tilde{\lambda}L\right) = 0 \tag{A.9}$$

By solving Equation (A.9), we can calculate the frequency of the nth vibration mode of the cantilever by

$$f_n = \frac{\left(\tilde{\lambda}_n\right)^2}{2\pi}\sqrt{\frac{EI}{\rho bh}} \tag{A.10}$$

A.4.2 Mode shape of the cantilever

By using the third equation of Equation (A.5), we can express B and D by

$$\begin{aligned} B &= \frac{\tilde{k}_e}{2EI\tilde{\lambda}_n}\left(\cos\left(\tilde{\lambda}_n L\right) + \cosh\left(\tilde{\lambda}_n L\right)\right) + \sinh\left(\tilde{\lambda}_n L\right) \\ D &= -\frac{\tilde{k}_e}{2EI\tilde{\lambda}_n}\left(\cos\left(\tilde{\lambda}_n L\right) + \cosh\left(\tilde{\lambda}_n L\right)\right) + \sin\left(\tilde{\lambda}_n L\right) \end{aligned} \tag{A.11}$$

so

$$A = -C = -\frac{\tilde{k}_e}{2EI\tilde{\lambda}_n}\left(\sinh\left(\tilde{\lambda}_n L\right) + \sin\left(\tilde{\lambda}_n L\right)\right) \tag{A.12}$$

By dividing these expressions by $\tilde{k}_e\left(\cos\left(\tilde{\lambda}_n L\right) + cosh\left(\tilde{\lambda}_n L\right)\right)/2EI\tilde{\lambda}_n$, the expression of the mode shape becomes

$$\phi_n\left(\tilde{x}\right) = K_1\sin\left(\tilde{\lambda}_n\tilde{x}\right) - K_2\sinh\left(\tilde{\lambda}_n\tilde{x}\right) + \frac{\sin\left(\tilde{\lambda}_n L\right) + \sinh\left(\tilde{\lambda}_n L\right)}{\cos\left(\tilde{\lambda}_n L\right) + \cosh\left(\tilde{\lambda}_n L\right)}\left(\cosh\left(\tilde{\lambda}_n\tilde{x}\right) - \cos\left(\tilde{\lambda}_n\tilde{x}\right)\right) \tag{A.13}$$

where

$$K_1 = \frac{\cos\left(\tilde{\lambda}_n L\right) + \cosh\left(\tilde{\lambda}_n L\right) + \frac{2EI\tilde{\lambda}_n}{\tilde{k}_e}\sinh\left(\tilde{\lambda}_n L\right)}{\cos\left(\tilde{\lambda}_n L\right) + \cosh\left(\tilde{\lambda}_n L\right)} \tag{A.14}$$

and

$$K_2 = \frac{\cos\left(\tilde{\lambda}_n L\right) + \cosh\left(\tilde{\lambda}_n L\right) - \frac{2EI\tilde{\lambda}_n}{\tilde{k}_e}\sin\left(\tilde{\lambda}_n L\right)}{\cos\left(\tilde{\lambda}_n L\right) + \cosh\left(\tilde{\lambda}_n L\right)} \tag{A.15}$$

We can notice that $K_1 \to 1$ and $K_2 \to 1$ when $\tilde{k}_e \to \infty$, and it gives us the mode shape of fully clamped cantilever.

A.5 Electrical measurement of the vibration of the short cantilever

A.5.1 Expression of the vibration from the motional current

In this section we determine the expression of the vibration of the short cantilever from the motional current measured with the impedance analyzer. To do so, we first determine the expression of the variable capacitance $C(t)$ due to the vibration of the short cantilever. We have

$$C\left(t\right) = \int_0^{L_1} \frac{\varepsilon_0 b C_n}{g - \tilde{w}_1\left(\tilde{x},t\right)} d\tilde{x} = \int_0^1 \frac{\varepsilon_0 b C_n L_1}{g - \left(a_{1S}\phi_1\left(x\right) * g + a_1\phi_1\left(x\right) * g\right)} dx \tag{A.16}$$

The derivative with respect to the time $\tilde{t}$ gives

$$\begin{aligned} \frac{\partial}{\partial\tilde{t}} C\left(t\right) &= \frac{\partial}{\partial t}\frac{C\left(t\right)}{\tau} = \int_0^1 \frac{\varepsilon_0 b C_n L_1 * \dot{a}_1\phi_1\left(x\right) * g}{\tau * \left(g - \left(a_{1s}\phi_1\left(x\right) * g + a_1\phi_1\left(x\right) * g\right)\right)^2} dx \\ &= \frac{\varepsilon_0 b C_n L_1}{\tau g} * \int_0^1 \frac{\dot{a}_1\phi_1\left(x\right)}{\left(1 - \left(a_{1s}\phi_1\left(x\right) + a_1\phi_1\left(x\right)\right)\right)^2} dx \end{aligned} \tag{A.17}$$

With a third order Taylor series expansion, we obtain

$$\begin{aligned} \frac{\partial}{\partial\tilde{t}} C\left(t\right) &= \frac{\varepsilon_0 b C_n L_1}{\tau g} * \int_0^1 \dot{a}_1\phi_1\left(x\right)\left[1 + 2\left(a_{1s}\phi_1\left(x\right) + a_1\phi_1\left(x\right)\right)\right. \\ &\quad \left. + 3\left(a_{1s}\phi_1\left(x\right) + a_1\phi_1\left(x\right)\right)^2 + 4\left(a_{1s}\phi_1\left(x\right) + a_1\phi_1\left(x\right)\right)^3\right] dx \\ &= \frac{\varepsilon_0 b C_n L_1}{\tau g}\dot{a}_1 * \left[\int_0^1 \phi_1\left(x\right) \mathrm{dx} + 2\left(a_{1s} + a_1\right)\int_0^1 {\phi_1}^2\left(x\right) dx\right. \\ &\quad \left. + 3\left(a_{1s} + a_1\right)^2\int_0^1 {\phi_1}^3\left(x\right) dx + 4\left(a_{1s} + a_1\right)^3\int_0^1 {\phi_1}^4\left(x\right) dx\right] \end{aligned} \tag{A.18}$$

By keeping only terms with $\dot{a}_1$, we obtain

$$\frac{\partial}{\partial\tilde{t}} C(t) = \frac{\varepsilon_0 b C_n L_1}{\tau g}\dot{a}_1 * \left(0.784 + 2a_{1s} + 4.43{a_{1s}}^2 + 9.39{a_{1s}}^3\right) \tag{A.19}$$

The relation between the motional current $I_1(\tilde{t})$ and $C(t)$ is

$$I_1(\tilde{t}) = V_{DC}\frac{\partial}{\partial \tilde{t}}C(t) \tag{A.20}$$

From Equation (A.19) and Equation (A.20), we obtain

$$\dot{a}_1(t) = \frac{I_1(\tilde{t})}{V_{DC}} * \frac{\tau g}{\varepsilon_0 b C_n L_1 (0.784 + 2a_{1s} + 4.43{a_{1s}}^2 + 9.39{a_{1s}}^3)} \tag{A.21}$$

From Equation (A.21), the relation between the vibration amplitude at the end of the short cantilever (W_1) and the amplitude of the motional current (i_1) is

$$\frac{W_1}{g * \phi_1(1)} * 2\pi f\tau = \frac{i_1 \tau g}{\varepsilon_0 b C_n L_1 V_{\mathrm{DC}} (0.784 + 2a_{1s} + 4.43{a_{1s}}^2 + 9.39{a_{1s}}^3)} \tag{A.22}$$

where f is the excitation frequency. Finally

$$W_1 = \frac{i_1 g^2 \phi_1(1)}{2\Pi f \varepsilon_0 b C_n L_1 V_{\mathrm{DC}} (0.784 + 2a_{1s} + 4.43{a_{1s}}^2 + 9.39{a_{1s}}^3)} \tag{A.23}$$

We notice that this expression contains the normalized static deflection a_{1s} which has to be calculated with the model.

A.5.2 Comparison between the vibration calculated from the motional current and the vibration measured with the LDV

Once we can calculate the vibration amplitude from the motional current, we compare it with the vibration amplitude measured with the LDV, and the results are shown in Figure A.3.

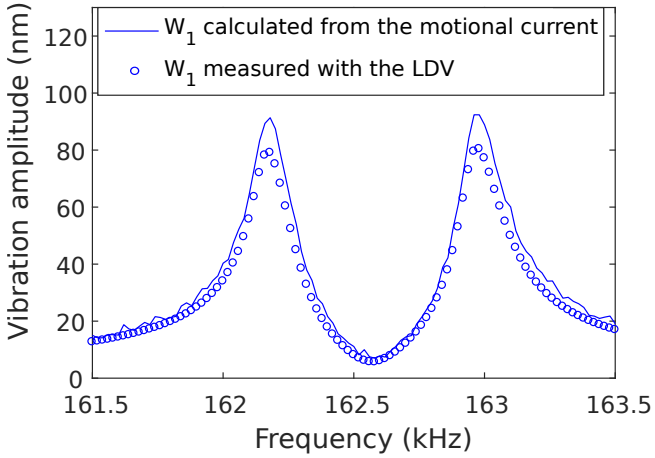

Figure A.3: Comparison between the vibration calculated from the motional current and the vibration measured with the LDV

We notice in Figure A.3 that there is a difference between the two vibration amplitudes. The quotient between the two results shows that the vibration amplitudes calculated from the motional current is

15% higher than those measured with the LDV. It can be explained by the vibration measured with the LDV, which does not correspond exactly to the vibration at the end of the short cantilever. As the size of the laser spot is not negligible, we cannot put it exactly at the end of the short cantilever. But it can also be explained by the accuracy of the electrical measurement.

List of Figures

List of Tables

Titre: Modélisation, fabrication et caractérisation expérimentale de réseaux MEMS faiblement couplés pour la détection de masse
Mots-clés: Localisation de mode, MEMS, détecteur de masse, défauts de fabrication, couplage mécanique, non-linéarités électrostatique, gamme dynamique

Une étude sur les détecteurs de masse utilisant la localisation d'Anderson est menée dans le cadre de cette thèse. Différents moyens permettant d'améliorer leurs performances sont proposés et démontrés à travers deux dispositifs MEMS. Les deux dispositifs utilisent le même système composé de deux cantilevers couplés mécaniquement, mais les vibrations sont générées de deux manières différentes: le premier dispositif est actionné par une force électrostatique attractive tandis que le second est actionné par une force électrostatique répulsive. Afin de se débarrasser du déséquilibre créé par les défauts de fabrication, on utilise l'assouplissement électrostatique en réglant la tension continue de l'actionnement. Pour le premier dispositif, une approche utilisant un système asymétrique avec deux cantilevers de longueurs différentes est proposée. On réduit alors la rigidité effective de la poutre courte pour équilibrer le système. Avec le second type d'actionnement, le faible assouplissement électrostatique nous oblige à utiliser deux micropoutres de même longueur. Mais le système est toujours équilibré de la même manière. Grâce à la fonctionnalisation des non-linéarités électrostatiques, le premier dispositif montre une meilleure sensibilité, qui est de 67 % supérieure à la sensibilité maximale atteignable en régime linéaire. Quant au second dispositif, il montre l'absence de non-linéarités électrostatiques, ce qui permet d'augmenter sa gamme dynamique linéaire jusqu'à 70 % de la distance qui sépare les poutres des électrodes inférieures. Cela devrait améliorer non seulement la résolution en masse du détecteur, mais aussi la précision des mesures. Tous ces concepts sont d'abord étudiés théoriquement avec le modèle analytique basé sur la théorie d'Euler-Bernoulli. Ils sont ensuite démontrés expérimentalement après que les détecteurs aient été fabriqués suivant le processus MUMPS®.

Title: Modeling, fabrication and experimental characterization of weakly coupled MEMS arrays for mass detection
Keywords: Mode localization, MEMS, mass sensor, manufacturing defects, mechanical coupling, electrostatic nonlinearities, dynamic range.

A study on mass microsensors using Anderson localization is conducted in this thesis. Different ways allowing to enhance their performance are proposed and demonstrated through two MEMS devices. Both devices use the same system composed of two mechanically coupled cantilevers, but the vibrations are generated in two different ways: the first device is actuated with an attractive electrostatic force while the second device is actuated with a repulsive electrostatic force. In order to get rid of initial imbalance due to manufacturing defects, the electrostatic softening effect is used by tuning the DC voltage of the actuation. For the first device, a concept with an asymmetric system including two cantilevers of different lengths is proposed. We thus reduce the effective stiffness of the short cantilever to balance the system. With the second type of actuation, the weak electrostatic softening effect forces us to use two microbeams of the same length. But the system is still balanced with the same approach. Thanks to the functionalization of electrostatic nonlinearities, the first device shows an enhanced sensitivity, which is 67 % higher than the maximum sensitivity reachable in the linear regime. Concerning the second device, it shows the absence of electrostatic nonlinearities, which allows to increase the linear dynamic range by up to 70 % of the gap. It should improve not only the mass resolution of the sensor, but also the accuracy of the mass sensing. All of these concepts are first theoretically investigated with the developed analytical model based on the Euler-Bernoulli beam theory. They are then experimentally demonstrated after the sensors are manufactured with the MUMPS®.